Diffractive Micro-Electromechanical Structures in Si and SiGe

Diffractieve micro-elektromechanische structuren
in silicium en silicium-germanium

Sukumar Rudra

Promotor: prof. dr. ir. D. Van Thourhout
Proefschrift ingediend tot het behalen van de graad van
Doctor in de Ingenieurswetenschappen: Fotonica

Vakgroep Informatietechnologie
Voorzitter: prof. dr. ir. D. De Zutter
Faculteit Ingenieurswetenschappen en Architectuur
Academiejaar 2012 - 2013

UNIVERSITEIT
GENT

ISBN 978-90-8578-614-6
NUR 959
Wettelijk depot: D/2013/10.500/47

Universiteit Gent
Faculteit Ingenieurswetenschappen en Architectuur
Vakgroep Informatietechnologie

Diffractive Micro-Electromechanical Structures in Si and SiGe

Diffractieve micro-elektromechanische structuren in silicium en silicium-germanium

Sukumar Rudra

Proefschrift tot het bekomen van de graad van
Doctor in de Ingenieurswetenschappen:
Fotonica
Academiejaar 2012-2013

Universiteit Gent
Faculteit Ingenieurswetenschappen en Architectuur
Vakgroep Informatietechnologie

Promotor:

Prof. Dr. Ir. Dries Van Thourhout

Examencommissie:

Prof. Dr. Ir. Hendrik Van Landeghem (voorzitter)	Universiteit Gent, LERC
Prof. Dr. Ir. Dries Van Thourhout (promotor)	Universiteit Gent, INTEC
Prof. Dr. Ir. Herbert De Smet (secretaris)	Universiteit Gent, CMST
Prof. Dr. Ir. Roel Baets	Universiteit Gent, INTEC
Dr. Ir. Ann Witvrouw	KU Leuven, MTM
Dr. Ir. Marcel Tichem	TU Delft, PME
Dr. Ir. Pieter Dumon	Universiteit Gent, INTEC

Universiteit Gent
Faculteit Ingenieurswetenschappen en Architectuur

Vakgroep Informatietechnologie
Sint-Pietersnieuwstraat 41, B-9000 Gent, België

Tel.: +32-9-264.99.59
Fax.: +32-9-331.35.93

Acknowledgments

It is not an easy task to cover all the people who have directly or indirectly helped me in accomplishing this thesis in the final form. However, I would first start with giving thanks to Dries who trusted in my capabilities in completing the designated task. Being one of the very few people to interact with regarding my research work, I learned a lot of minute scientific and technical details from him. His approach to supervision gave me full independence in doing things my own way and own pace.

A significant chunk of the work in this thesis was carried out as a part of the bigger project of GEMINI which was chaired by Dr. Ann Witvrouw. Even after having numbered interactions, I appreciate her dedication in conducting the whole project work with utmost importance. I appreciate the patience with which the devices were fabricated even after repeated initial failures. Within the same scope of the project, I would also like to thank Jeroen De Coster who helped me with all the LDV measurements which formed a significant backbone of this thesis work.

The last part of the work in this thesis was carried out at Ghent University clean-room facilities at Zwijnaarde. I express my regards to Steven who taught me all the processing details and provided continuous support and technical assistance throughout my work. I would also like to thank Liesbet for her patience in capturing all the SEM images which enabled my thesis a more handsome look. Thanks to Jeroen Allaert as well, without his handmade circuits, my publication list would have looked even slimmer.

Special thanks to my mentor Joris who was a key person in helping me in getting started with this PhD. I am thankful for all his valuable suggestions and ideas.

I would also like to thank Honguiy, Thijs, Eva, Peter, Diedrik and Thomas to provide a charming environment inside an office space with hammering construction noise for months. I am also thankful to all my colleagues for all the opportunities of socializing during evening drinks, chit-chats, hangouts, Photonics/Group days, Ghent fest, badminton rounds and many more.

Throughout my stay in PRG, I enjoyed every bit of the humor spread through the group email. Particularly those ideas of giving goodbye gifts always amazed me.

My regards to Aditya, Pijush, Sarvagya, Stevan, Shibnath and Punitha for all the discussions during lunch or coffee break. Thanks to Ananth in providing continuous enthusiasm and teaching me table tennis. Special thanks to Samir, I could not have survived my PhD period without devouring the delicious bhat, dal and chicken curry/ chingri machher kalia prepared by him over and over again. Thanks to Rajesh for all those prolonged discussions every now and then.

I would also like to thank Kedar, Anil and Ark with whom I discovered every nook and corners of Ghent. In their absence, I would not have been able to appreciate the numerous Belgian beers which fill a significant part of my stay in Ghent. Special thanks to Adil for all the numerous discussions, hangouts and for being just a good philosophical friend. Thanks to my gang of other Indian friends: Unmesh, Sandeep, Chetan, Karthik and many others who filled a significant part of my social life.

My deepest gratitude goes to my parents. Without their endless affection and continuous support, I could not have achieved anything. Also, thanks to Srestha for all the emotional support during the troubled days.

I shall finally sign-off with regards to this beautiful city of Ghent which became my home for more than four years. It will forever hold a special place in my heart.

Thank you all, for everything.

Eindhoven, August 2013
Sukumar Rudra

Table of Contents

List of Figures

List of Acronyms

A

ASAP	Advanced Systems Analysis Program

C

CCD	Charge-coupled Device
CMOS	Complementary Metal Oxide Semiconductor
CMP	Chemical Mechanical Polishing
CPU	Central Processing Unit

D

DFB-LD	Distributed Feedback Laser Diodes
DMD	Digital Micromirror Device
DUV	Deep Ultra Violet
DWDM	Dense Wavelength Division Multiplexing

F

FGC	Focusing Grating Coupler
FWHM	Full Width at Half Maximum

G

GLV	Grating Light Valve

H

HDP	High Density Plasma

I

IC	Integrated Circuit

L

LCD	Liquid Crystal Display
LDV	Laser Doppler Vibrometry

M

MFD	Mode Field Diameter
MEMS	Micro-electro-mechanical Systems
MOEMS	Micro-opto-electro-mechanical Systems

N

NIR	Near Infrared

O

OPD	Optical Path Difference

P

PDL	Polarization Dependent Loss
PSI	Phase Shifting Interferometery

R

RCWA	Rigorous Coupled Wave Analysis

S

SEM	Scanning Electron Microscope
SFD	Squeezed Film Damping
SMF	Single Mode Fiber
SOI	Silicon-On-Insulator
SRAM	Static Random Access Memory

T

TE	Transverse Electric
TM	Transverse Magnetic

V

VOA	Variable Optical Attenuator
VCSEL	Vertical Cavity Surface Emitting Laser
VLC	Visible Light Communications
VSI	Vertical Scanning Interferometry

W

WDM	Wavelength Division Multiplexing

Nederlandse samenvatting –Summary in Dutch–

Optische systemen vinden vandaag vooral toepassingen in beeldacquisitie, communicatie en beeldschermen. De motivatie om optische systemen te miniaturiseren is daarom gelijklopend als die voor elektronische systemen: het creëren van goedkopere en meer functionele systemen en het toegang krijgen tot applicaties waar bulk optische componenten eenvoudig weg niet passen. Tegelijkertijd vereisen de meeste systemen zowel elektronica (bv. voor de aansturing) en optische componenten, en moeten deze intiem geïntegreerd worden. Deze directe integratie met elektronische systemen zorgt ervoor dat goedkope en overvloedige rekenkracht uitgebreid beschikbaar is. Anderzijds is miniaturisatie ook voordelig omdat het toelaat om vele parallelle kleinere systemen het werk te laten doen van een enkel groter systeem. Al deze voordelen maken dat er een grote interesse is in de studie van de integratie van klassieke geïntegreerde schakelingen (IC) met micro-elektro-mechanische systemen (MEMS) als een platform voor geminiaturiseerde optische systemen.

Deze nieuwe klasse van microsystemen, genaamd micro-optische elektromechanische systemen (MOEMS), die heeft geleid tot nieuwe optische functionaliteit met voordien nooit vertoonde kwaliteit en nauwkeurigheid. Het samenbrengen van deze verschillende technologieplatformen heeft geleid tot industrieel belangrijke verwezenlijkingen zoals de DMD (digital micromirror displays), laser scanners, optische schakelaars en dynamische microspiegels gebaseerde beeldschermen. De trend om klassieke optische systemen te miniaturiseren en verder te integreren zal ook de adoptie en commercialisatie van MOEMS technologie versnellen.

Het onderzoek in deze thesis naar Silicium Germanium gebaseerde MOEMS kadert in deze toenemende trend naar integratie van elektronica en microsystemen. Poly-SiGe is een ideaal materiaal voor het postprocessen van MEMS structuren boven op elektronische chips. De films hebben heel goede elektrische en mechanische eigenschappen en worden gedeponeerd op een relatief lage temperatuur die compatibel is met bestaande elektronische chips. Het SiGe-MEMS platform laat dan ook toe om complexe MEMS structuren bovenop be-

staande elektronische chips te fabriceren en direct te interconnecteren met de aanstuurcircuits. Dit maakt het platform heel interessant voor toepassingen die heel grote rijen of matrices van MEMS schakelaars vereisen, die elk individueel moeten worden verbonden met de besturingslogica.

Dit werk focusseert in het bijzonder op de volgende MOEMS applicaties:

Beeldvormende systemen: MOEMS, die MEMS en micro-optische componenten combineren, zijn vanzelfsprekend in de eerste plaats bedoeld voor het manipuleren van licht. Verschillende aanpakken voor het sturen, richten en moduleren van licht bundels gebruik makend van minuscule micromechanische structuren kunnen worden beschouwd. Verschillende types MOEMS gebaseerde systemen werden ontwikkeld voor toepassingen in defensie, luchtvaart, industrie, medische wereld en consumer markt, onder de vorm van draagbare beeldschermen, barcode lezers, projectie gebaseerde beeldschermen en infrarood camera's. Een goed voorbeeld van een zeer succesvol MOEMS product is Texas Instrument's DMD array, die waarschijnlijk het grootst aantal bewegende mechanische componenten (meer dan 1 miljoen) bevat ooit samengebracht in 1 product.

In dit werk hebben we een poly-Silicium Germanium gebaseerde GLV (grating light valve) MOEMS in detail bestudeerd. GLV beeldscherm pixels zijn opgebouwd uit aanpasbare diffractie-roosters die in reflectie werken. Elk van de pixels bestaat uit een aantal parallelle, vrijstaande microbalkjes die verticaal kunnen bewegen in respons op een elektrisch veld en op die manier een diffractie rooster kunnen vormen met variabele amplitude. Het onderzoek focusseerde zich op de optische en mechanische performantie van deze roosters en met name het bereikbare optische contrast en de schakeltijd. De voor- en nadelen van verschillende ontwerpscriteria werden in detail onderzocht en geoptimaliseerd om de performantie van de systemen te maximalizeren. De meetopstelling wordt uitvoering besproken en methodes om de contrastmeting te verbeteren worden aangebracht. Methodes om de verschillende dimensionele parameters zodanig te kiezen dat kritische demping - met de beste schakeltijd - wordt bekomen zijn onderzocht en experimenteel geverifieerd. De mogelijkheid om GLV's te gebruiken in combinatie met een grijswaardeschaal werd geverifieerd. Deze optie is een van de belangrijkste voordelen die deze GLV's bieden t.o.v. concurrenten in het zelfde veld zoals DMD's.

Variabele optische attenuator (VOA): VOA's spelen een sleutel rol in het controleren van vele optische systemen en in het bijzonder in optische netwerken. In optische vezelsystemen kunnen een hele reeks van vermogenniveaus gebruikt worden, van heel sterke signalen (~100mW), direct na de transmitter tot heel zwakke signalen (~ microwatt) na transmissie over langere

afstanden. VOA's kunnen dan gebruikt worden om het vermogen van deze signalen aan te passen en op een gelijk niveau te brengen. Oorspronkelijk werden ze gebruikt om optische ontvangers te beschermen van al te hoge invallende vermogens en het simuleren van verschillende reikwijdtes in systemen met beperkte lengte. De ontwikkeling van golflengte gemultiplexeerde communicatiesystemen (DWDM of Dense Wavelength Division Mulitiplexion) heeft nieuwe toepassingsgebieden voor VOA's geopend, en met name het in vermogen egaliseren van rijen van laserbronnen wordt alsmaar belangrijker.

Verschillende types VOA's werden al ontwikkeld voor deze toepassingen. In dit werk is een diffractierooster gebaseerde VOA ontwikkeld. De component werd gevormd door de elektrodes van een poly-SiGe component te structureren en op die manier een twee-dimensionaal rooster te vormen, dat ongevoelig is aan de polarizatie van de invallende licht bundel, in tegenstelling tot de eendimensionele roosters die eerder werden onderzocht. Het verlies van de component, de polarisatieafhankelijkheid, dynamisch bereik en schakeltijd zijn onderzocht. Mogelijke verbeteringen van de optische en mechanische performantie worden besproken.

Microsystemen voor siliciumfotonica: Silicium fotonica vormt een ideaal platform voor de miniaturisatie van geïntegreerde optische circuits, vanwege het hoge index contrast tussen silicium en lucht of oxide, wat toelaat het licht heel sterk op te sluiten in de kern van de golfgeleiders. Bovendien vertoont silicium heel lage verliezen bij golflengtes van 1.3-1.6 micrometer, wat belangrijk is voor toepassingen in telecommunicatie. Het belangrijkste voordeel wellicht is echter het feit dat voor hun fabricage de zelfde toestellen gebruikt kunnen worden als die voor de fabricage van de meest geavanceerde elektronische systemen gebruikt worden. Ondanks al deze voordelen blijft een belangrijk struikelblok het in- en uitkoppelen van licht in deze silicium gebaseerde optische circuits. Het belangrijkste probleem is het verschil in modediameter voor het licht in de golfgeleiders - een paar honderd nanometer - en dat in de optische vezel - een tiental micrometer. Een oplossing voor dit probleem is de gefocusserde roosterkoppelaar, die eerst een laterale transformatie ondergaat in het vlak en dan het licht uitkoppeld over een afstand van een 10-tal micrometer en op die manier de bundeldiameter aanpast aan die van de optische vezel. Maar zelfs met deze koppelaar is nog altijd een alignatienauwkeurigheid vereist van minder dan 1 micrometer, wat moeilijk haalbaar is met standaard verpakkingstechnologieën en vaak ook van een vergelijkbare grootteorde is als de excentriciteit van de kern in vezelarrays.

Daarom hebben we in dit werk een nieuw idee om dit alignatieprobleem op te lossen onderzocht. Door de roosterkoppelaar vrij op te hangen en kamtype actuatoren te bevestigen langs beide zijden kunnen ze in principe zowel lateraal

als transversaal worden bewogen. Door het actueren van de kamactuatoren in een specifieke combinatie kan de positie van de roosters dan in principe geoptimaliseerd worden t.o.v. de optische vezel en kan de koppel efficiëntie worden verbeterd. Binnen dit werk zijn we er in geslaagd de laterale beweging te demonstreren. De transversale beweging - langs de as van de binnenkomende golfgeleider - kon nnog niet eenduidig worden vastgesteld. Naast deze structuur is een alternatief voorgesteld waarbij de capacitieve kracht tussen roosterkoppelaar en substraat werd benut om de koppelaar uit het vlak te laten roteren. Op deze manier kan het signaal komende uit de roosterkoppelaar in verschillende richtingen worden gestuurd en kan het worden gebruikt voor bundelsturing in vrije ruimte interconnecties.

English summary

Modern optics is primarily used for information capture, communication and imaging applications. The motivation for miniaturization of optics is therefore the same as for electronics; to create cheaper and more functional information-technology (IT) systems, and to gain access to regions where bulk equipments will not fit. At the same time, highly-functional IT systems require both electronics (for computations) and optics (for communication), so these two should be closely integrated. A direct consequence of the integration with electronics is the availability of cheap and abundant signal processing. On the other hand, reduction of the overall size is also advantageous to use many parallel systems to perform the job of a single large device. It leads us to consider Integrated Circuits (IC) and micro-electro-mechanical systems (MEMS) as platform for miniaturized optical systems.

The integration of micro-optics and MEMS has created a new class of microsystems, termed as micro-opto-electro-mechanical systems (MOEMS) that are capable of performing a range of optical functions with unprecedented levels of quality and accuracy. Merging all these multi technologies, made MOEMS an ideal knowhow for many industrial demonstrations of commercial devices, such as optical switches, digital micromirror devices (DMD), laser scanners, optical shutters and dynamic micromirror displays. All technologies of MOEMS have the potential of batch processing and embossed replication which, again, makes them highly attractive and necessary for commercial applications. The trend towards miniaturization and integration of conventional optical systems will further accelerate the adoption of MOEMS technology in commercialization of many industrial components.

Keeping in mind the benefits of integration of electronics and microsystems, we describe poly-SiGe based MOEMS devices in this thesis. Poly-SiGe has been demonstrated to be an ideal material for post-processing MEMS above CMOS, since films with very good electrical and mechanical properties can be obtained at CMOS-compatible temperatures.

The SiGe MEMS technology allows to postprocess MEMS structures on top of CMOS with a large number of fine-pitch interconnections between the MEMS devices and the underlying circuits. This makes the SiGe MEMS platform very

well suited for applications that need large arrays of MEMS devices, which need to be individually connected to the interfacing circuits.

In this thesis we particularly focus on the following applications of MOEMS:

Display and imaging systems: MOEMS technology combining MEMS and micro-optics is well suited for manipulating light. Different ways can be envisioned to scan, steer or modulate light beams using tiny electromechanical structures. A number of MOEMS displays, imaging products and technology demonstrators have been developed for defence, aerospace, industrial, medical and consumer markets in the form of wearable displays, projection displays, imaging devices, barcode readers and infrared imaging cameras.

An array of micromechanical devices can be used to produce a line or a 2D array of pixels, each pixel is a microelectromechanical element that displays different pixel intensities or gray levels. A good example of a successful MOEMS display product is the Texas Instrument's digital micrrmirror device (DMD) display, which probably has the largest number of moving mechanical components (over 1 million) of any product.

In this work, we investigated the poly-SiGe based Grating Light Valve (GLV) devices in detail. GLV display pixels are reflection type diffraction gratings consisting of parallel freestanding microbeams which move vertically in response to an electric field and hence form a square well grating with changing phase. We particularly focused on the optical and mechanical performance of the devices in terms of the obtained contrast and switching rate. The pros and cons of the different design criteria are mentioned in detail to get the maximum performance out of the devices. A detail discussion is also presented on how the experimental setup can also influence the contrast measurement and to what extent it can be improved. We also discuss the influence of different dimensional parameters of the devices to obtain critical damping of the microbeams which provides the best switching rate. We also show the analog gray scale nature of the GLVs which is one of the strongest points of these devices compared to the other competitors within the same field (e.g. DMDs).

Variable optical attenuator (VOA): VOAs play a key role in the optical power management of many optical systems, especially in optical networks. Fiber-optic systems operate over a large span of optical power level, from very strong signals (>1 W) emitted from high-power laser sources to very weak signals (several microwatts) after transmitting over long distances. VOAs are key components for adjusting optical powers to different levels. They were initially used to protect optical receivers from overhigh incident powers and simulate different span losses in short-span systems. However, the development of dense wavelength division multiplexed (DWDM) systems technology has opened up

new application areas for VOAs. Empowered by advanced fabrication technologies and integration capabilities, different types of VOAs have been demonstrated based on the fiber direct coupling, laser interference, diffraction, refraction, and reflection; each having several different designs.

In this thesis we concentrated on diffractive grating based VOAs. We patterned the bottom electrode of the poly-SiGe devices to form 2D movable gratings which are more insensitive to polarization of the incident light beam compared to their 1D counterpart. We focused on investigating the insertion loss, polarization dependent loss, dynamic range and response time of the devices which are the prime factors in determining the overall performance of the VOAs. A detail discussion is also presented regarding the design of the device to show how the optical and mechanical performances can be improved further.

Silicon photonic microsystems: Silicon photonics is one of the ideal candidates for miniaturization of integrated photonic circuits due to the high index contrast between silicon and air which confines light effectively within the silicon core. Silicon exhibits low loss at wavelengths near 1.5 microns, which makes it simple to leverage existing telecommunications components. In addition, the fabrication and manufacturing of silicon photonics is typically compatible with CMOS-based silicon processing. Despite such positive prospects, a major stumbling block on the way to silicon photonics applications remains the issue of coupling light in and out of the photonic circuits by means of optical fibers. The major problem stems from the large mismatch in modesize of nanowires (a few hundred nanometers) and standard single mode fibers. One solution to this problem is to use a focused grating coupler (FGC) to perform a lateral spotsize conversion in an adiabatic taper plus out-of-plane coupling to a single mode fiber by diffraction via a waveguide grating. But, the most important feature of the FGC is their drop in coupling efficiency due to the slight lateral and angular misalignment of the single mode fiber above the grating structure.

In this thesis, we propose an idea to resolve the misalignment problem between a grating coupler and a single mode fiber (SMF) by attaching combinations of comb-drives on either sides of the FGC. By actuating the specific combination of comb-drives, the FGC can be moved in-plane and hence, any misalignment issue can be addressed within the maximum permissible displacement range of the FGC. At the same time, we propose another mechanism based on the capacitive action of MEMS devices which can tilt the FGC in out-of-plane direction. This way the outgoing signal from the FGC can be steered along multiple directions to mitigate the alignment issue and can also be used as a beam steering method in free space interconnects.

1 Introduction

Similar to what happened in the industrial age where the power to process and apply materials defined the productivity of a society, the ability to acquire, process and apply information defines the growth of the current era. The modern information processing power is provided mostly by highly advanced electronic integrated circuits (ICs). As these are continuously being miniaturized following Moore's law (Fig. 1.1), the total information processing power of humankind is growing exponentially. To take advantage of this, it is of extreme importance to design and build systems that can extract information from the physical world, which is inherently analog and can convert this information into formats recognizable to IC processors in efficient and economical ways. At the same time, action needs to be taken to react to the environment based on the processed information. In this process, it is very beneficial to integrate the information collector, processor and the corresponding actuators in a single system.

Micro-electro-mechanical systems (MEMS) can serve these needs. MEMS are a new frontier for miniaturization in the 21st century. The terms micro and electro refer to the compatibility with ICs, whereas mechanical refers to the interactive connection of the systems to the physical world. In MEMS, the information contained in an outside physical variable can be mechanically converted into electronic formats and processed by ICs or vice versa.

MEMS technology can be viewed as a technology for fabrication of micro-scale and nano-scale mechanical devices, based on semiconductor fabrica-

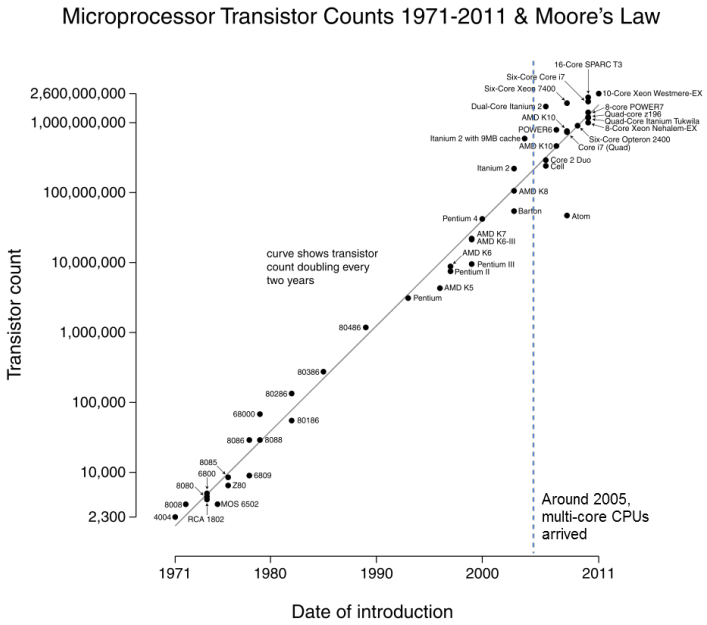

Figure 1.1: Plot of CPU transistor count against date of introduction. Note the logarithmic vertical scale; the line corresponds to an exponential growth with the transistor count doubling every two years.

tion technology. It mostly uses the same tools as those used for IC fabrication technology, complemented by some specific processing steps unique to MEMS technology. The majority of the MEMS fabrication techniques can be categorized either into surface micromachining or bulk micromachining [1] techniques. Surface micromachining consists of the addition or deletion of thin films of different materials by photolithography, thin film deposition techniques and dry and wet etching methods. Bulk micromachining is based on making different shapes using crystal orientation based etching of the silicon substrate underlying the thin film structures. The most common method for performing bulk micromachining is via selective masking and wet chemical solvents. The newer alternative to this method is dry etching using a plasma or laser system to remove unwanted material. This is generally more accurate than wet etching, but it is also more expensive.

In MEMS technology, the standard constructs of classical mechanics are not always useful, since weight is almost insignificant. However, other forces, especially electrostatic forces become more important. Therefore, MEMS de-

vices can move very rapidly without the movement creating mechanical wear or cracks over a very long period of time and hence resulting in very high switching rates (e.g. operations at several kilohertz over a number of years have been reported).

Depending on the transducing mechanisms MEMS can be categorized into mechanical transducers, electromagnetic transducers, microfluidic transducers, thermal transducers or optical transducers. In the remaining part of the thesis, we will focus only on the optical transducing methods using micro-opto-electro-mechanical systems (MOEMS) or optical MEMS (1.2), where optical information is obtained, modulated or created by MEMS devices.

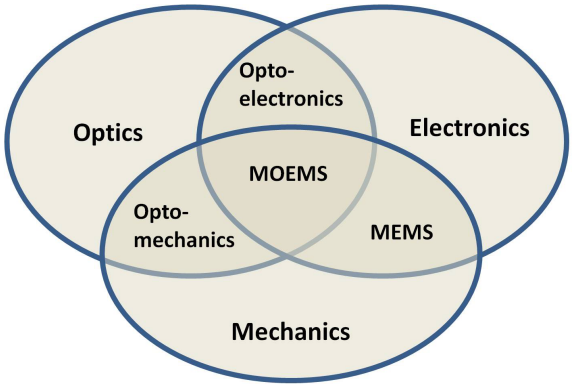

Figure 1.2: Multidisciplinary nature of optical MEMS.

1.1 Optical MEMS

During the past decade, the field of optical MEMS experienced a fast growth [1, 2]. The optical functionality facilitated by these microsystems goes from light emission, detection and amplification to switching, spatial modulation and routing of optical signals [3]. Performance of these devices increased with the advances in the field of materials and processing techniques and the development of a system approach for their conception. Miniaturization is one of the key aspects in the development of MOEMS. From the point of view of cost reduction, it is a significant factor in many cases. However, in most cases, miniaturization alone cannot ensure the commercial success of optical microsystems. Some of the key requirements for success are:

- the possibility to set-up large scale matrices of micro-device;
- the ability to reset optical properties, spatially and temporally, using microactuation and micro-deformation;

- nanopositioning, i.e. the nanoscale control of positioning precision and alignment for these devices;

1.2 Applications of Optical MEMS

Based on their operating mechanism, MOEMS can be classified into three different categories: geometrical, interferometric/ diffractive and electromagnetic devices. Geometric MOEMS modulate the intensity of the light by changing the optical path of the incident light; interferometric/ diffractive optical MEMS use two or multi beam interference or diffraction to change the spatial and spectral distribution of the incoming light; electromagnetic MOEMS modulate the light by mechanically changing the electromagnetic boundary conditions of the waveguide structures or resonant cavities.

1.2.1 Geometric MOEMS

The majority of optical MEMS devices are based on the principles of geometric or Gaussian wave optics. These devices use mirrors or lenses with one or two degrees of rotational freedom to redirect the optical path of the light. Their diverse applications include two dimensional displays, optical communications, adaptive optics and medical imaging.

The Digital Micromirror Device (DMD) from Texas Instruments is one of the most commercially successful optical MEMS devices to date. The DMD chip is a MEMS array of aluminum alloy based micromirrors, monolithically integrated onto and controlled by an underlying CMOS SRAM array [2–4]. The micromirror superstructure is fabricated through a series of aluminum metal depositions, oxide masks, metal etches and organic spacer deposition steps. The organic spacers are then subsequently removed using oxygen and fluorine plasma etching to release the mirrors. The DMD has a layered structure, consisting of a micromirror layer, a yoke and hinge layer, and a metal layer on a CMOS memory array. An exploded view of the DMD layer and the corresponding AFM surface height images are shown in Fig. 1.3 [5].

One DMD chip contains half a million to more than two million of these independently controllable reflective micromirrors each with a size of the order of 14x14 μm^2 and 15 μm pitch. Each of these mirrors switch back and forth at a frequency on the order of 5-7 kHz. To produce grey scales, the mirror is toggled on and off very quickly, and the ratio of on time to off time determines the shade produced (binary pulse-width modulation). Contemporary DMD chips can produce up to 1024 shades of gray (10 bits). The micromirrors are rotated because of the electrostatic attraction of the mirrror structure and the underlying electrode. Fig. 1.4 shows a schematic of two pixels of a DMD [2]. The

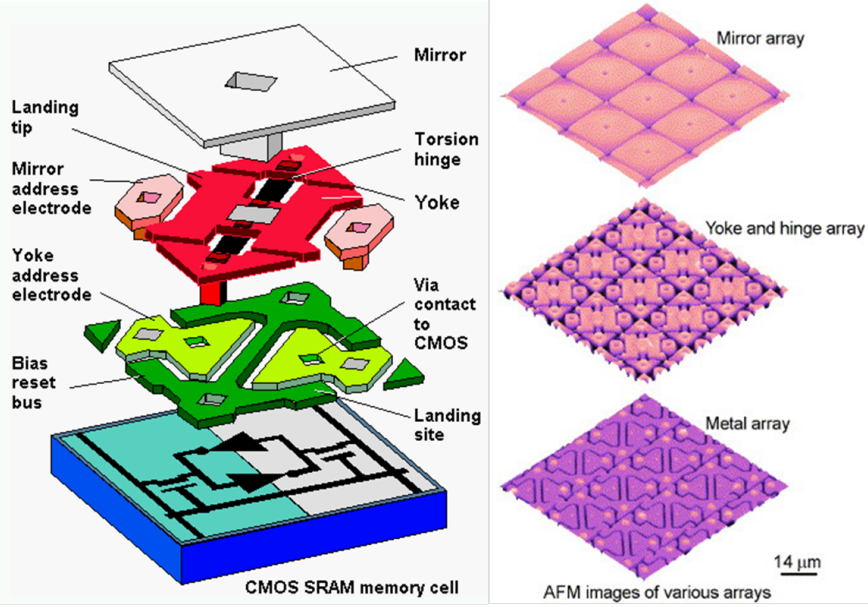

Figure 1.3: An exploded view of the DMD layered structure with AFM images showing the micromirror, yoke, hinge and metal layer arrays.

micromirror and the yoke are connected to a bias/ reset voltage. The address electrodes are connected to the underlying CMOS memory through contacts. Movement of the mirrors is accomplished by storing a 1 or 0 in the memory cell applying a bias voltage to the micromirror or yoke structure. When this occurs, the micromirror is attracted to the side with largest electrostatic field differential, as shown in Fig. 1.4. To release the micromirrors a short reset pulse is applied that excites the resonant mode of the structure and the bias voltage is removed. This combination allows the mirrors to leave the landing site. Each SRAM cell is connected to a micromirror and allows each mirror to be individually addressed so as to rotate ±12deg with respect to the horizontal plane, limited by a mechanical stop [2, 6]. Contact between cantilever spring tips at the end of the yoke (four are present on each yoke) with the underlying stationary landing sites is required for the binary operations.

DMD's major applications are digital projectors and projection TVs [6]. A variety of new applications including spectroscopy, volume display, lithography and microscopy are actively being exploited by researchers.

MEMS based optical switches are another set of examples which has taken a major role in the optical telecommunication market. With the recent popularity of fiber-to-the-home, gigabit ethernet and more and more upcoming band-

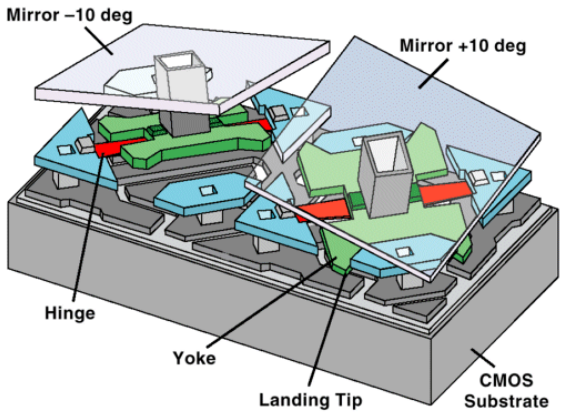

Figure 1.4: Two pixels of a DMD with the micromirror attached to the side of the largest field differential.

width hungry applications, large scale optical switches are becoming more of a necessity than a luxury. With its core 3D MEMS technology, CALIENT has developed its flagship S320 Photonic Switch [7]. This offers industry's one of the highest density photonic switches with 320 x 320 ports. As shown in Fig. 1.5, inside CALIENT's 3D MEMS photonic switching technology [8], the optical beams are steered in three dimensions by two stages of dual-axis micromirrors, directing it toward the desired output port where the input and output fibers are arranged in 2-D arrays.

The MOEMS micromirror [9] developed by Sandia National Laboratory is another example of a commercially successful optical switch which was designed for switching laser or IR signals. In addition to the examples discussed here, other companies, including Xerox, Optical MEMS and Agilent technologies have also been developing MOEMS based optical switches which are surely going to have a strong impact on the future of optical network communications.

1.2.2 Interferometric MOEMS

Interferometric optical MEMS change the spectral and spatial output of the incident light based on the principle of optical interference of two or multiple temporally and spatially coherent beams. In the interferometric MEMS devices, the amplitude of the light wave is split and the resulting wavefronts are added constructively or destructively.

Qualcomm's Mirasol displays uses the Interferometric Modulator (iMoD) technique which is a MOEMS device [11, 12] that is composed of two conductive plates. One is a thin film stack on a glass substrate over which the second,

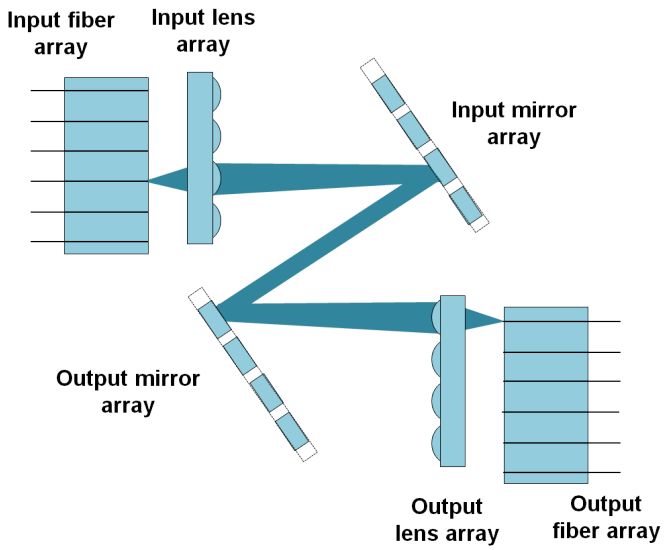

Figure 1.5: Schematic of a 3-D MEMS switch.

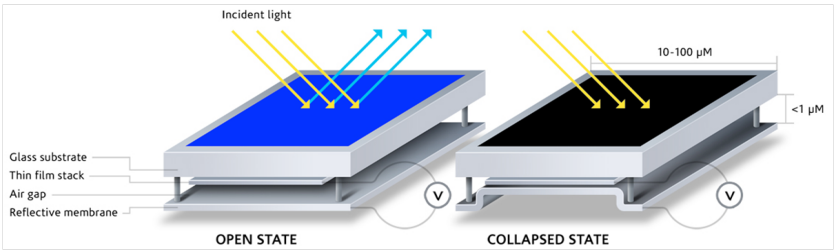

Figure 1.6: Basic structure of an iMoD pixel [10].

a metallic membrane, is suspended. There is an airgap between the two in the non-actuated state and when the light is hitting the substrate it is simply reflected back as shown in left figure of Fig 1.6. In the actuated state, when a small voltage is applied, the plates are pulled together by electrostatic attraction and the light is absorbed, turning the element black. This is the fundamental building block of the Mirasol display. iMoD elements are typically 25- 60 μm on a side (400- 1000 dots per inch). Therefore, many iMoD elements are stacked and driven together as a single pixel when used in a color display. The color of the iMoD element is determined by the size of the gap between the plates. Compared to classical displays, the iMoD display technique increases brightness and contrast and enables saturated colors to be displayed, high-resolution formats, smooth video playback and low power consumption.

1.2.3 Diffractive grating MOEMS

Unlike the interferometric MOEMS, diffractive MEMS change their spectral and spatial output based on the principle of diffraction. Here the wavefronts are split spatially to change the direction of propagation of the outgoing light and hence creating an ON or OFF state to modulate the light intensity.

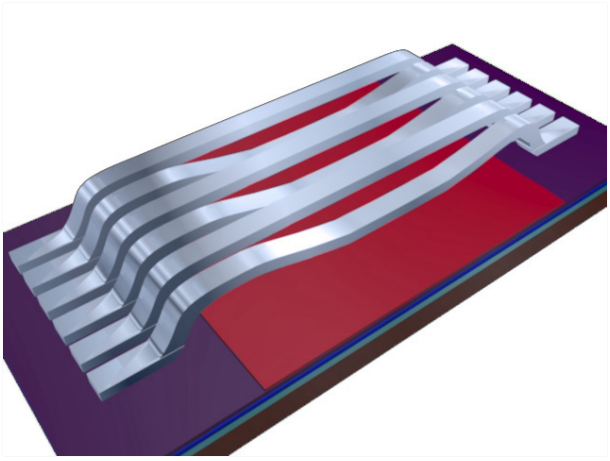

Figure 1.7: Single pixel of a GLV matrix where the alternate ribbons are actuated (ON state) to create the grating shape.

An example of a diffractive MOEMS device which has gained quite a lot of attention due to its high performance and simple fabrication process is the Grating Light Valve [13–15] technology developed by Silicon Light Machines. It is a unique MOEMS that acts as a dynamic tunable grating to precisely vary the amount of laser light that is diffracted or reflected. The GLV is made of many microscale ribbons on the surface of a silicon plate (Fig. 1.7). These ribbons can move upwards or downwards by very small distances by adjusting the electrostatic forces between the ribbons and the substrate. Due to the positioning of the ribbons, each element can modulate light, so that a well positioned matrix can vary the level of reflected light. The light control can be analog or digital (on/off switching). As the GLV device uses the grating diffraction principle to switch, dim and modulate light, it is very precise, easy to produce and can possibly manipulate relatively high power beams.

Each GLV component is made of 6 parallel ribbons that are suspended at both ends and made of a thin layer (~ 300-400 nm) of silicon nitride (with high tensile stress ~ 800 MPa) covered with a reflective metal layer. This upper layer also acts as an electrode, allowing to attract the ribbons towards the bottom electrode shared by every tape. Through applying an electric field between the

two, the switching from the undeflected state to maximum deflection of the ribbon is fast. It can switch in ~ 100 nanoseconds which is a million times faster than conventional LCD display devices, and about 1000 times faster than TI's DMD technology (see section 1.2.1). This high speed can be achieved because of the small size and mass of the ribbons and the small excursion needed (only a few hundreds of nanometers). Besides, there is no physical contact between moving elements which results in a lifetime for GLVs of as long as 15 years without stopping (over 210 billion switching cycles).

The GLV technology was originally developed for use in extremely high resolution digital display products. The GLV device creates bright and flawless images with high contrast and supreme color reproduction. Sony corporation is developing a product based on Silicon Light Machines' GLV technology to accelerate the development of its next generation display products that utilize lasers as a light source. Except for the display application, GLV technology can also be used in high-end printers and optical communications [15].

1.2.4 Microsystems for integrated optics

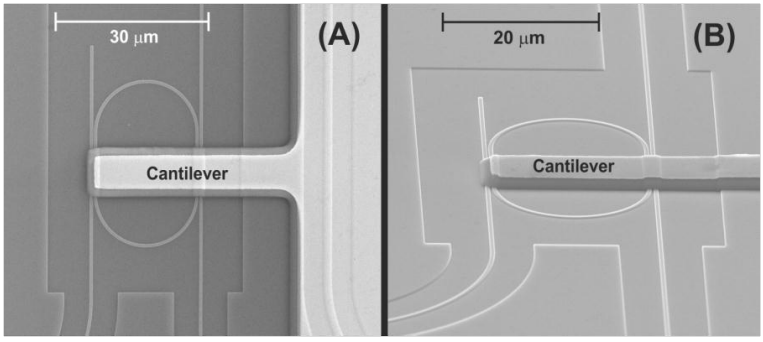

Figure 1.8: SEM image of a 40 μm long cantilever successfully integrated with the racetrack ring resonator showing (A) top view and (B) oblique view.

The optical microsystems described in the previous sections can be considered as free-space optical systems since the mobile structures (mirrors, gratings, etc.) interact with light during its travel through air. On the contrary, in integrated optics, light is contained in waveguides fabricated in the appropriate optical materials. In that case, it is hard to control the propagation of light with mirrors or diffraction gratings in direct contact with the light beam. However, there are other means to control light with mechanical structures in integrated optics. They are based on the evanescent coupling between guided light and dielectric structures such as bridges or cantilevers, suspended on waveguides.

Basically these devices are phase modulators and work by modifying the guided refractive index.

Tuning of a microring resonator makes it possible to use it as an active element, which can have ample applications in future optical communication networks. Changing the effective index of the guided mode of the ring resonator results in a shift of the ring's resonance wavelength. Among other methods (e.g. thermal tuning), opto-mechanical tuning by electrostatic actuation could potentially provide a broad wavelength tuning range and require only very little energy for operation. Fig. 1.8 shows an example of a silicon based ring resonator device whereby a cantilever is formed above the device using a surface micromachining technique. On application of a voltage between the top electrode and the substrate, the cantilever is pulled towards the resonator and the air is partially replaced by the dielectric material having a higher refractive index. This changes the modal propagation and hence tunes the resonator. These electrostatically actuated integrated devices have been fabricated on wafer scale with CMOS compatible technologies. Reversible resonance wavelength tuning over 122 pm with a modulation depth of 18 dB was demonstrated for this device [16].

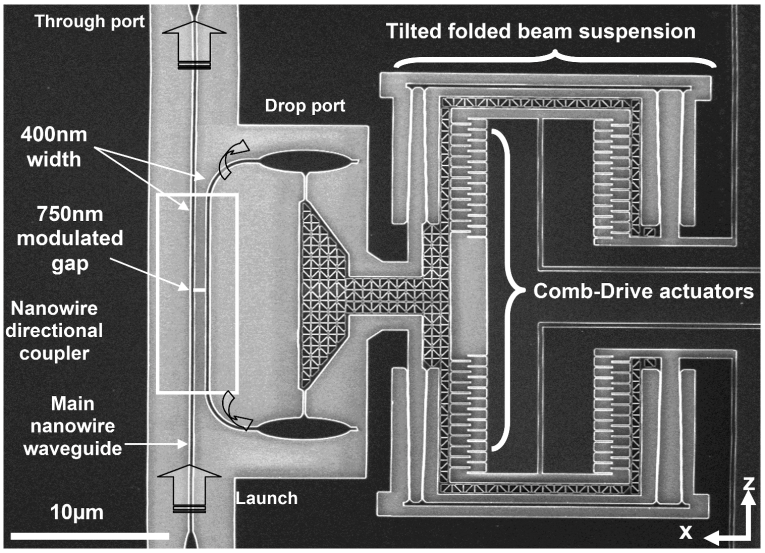

Figure 1.9: SEM diagram illustrating the fabricated device of the nanomechanically suspended low-loss silicon nanowire waveguide directional coupler displacement sensor [17].

Fig. 1.9 shows a novel integrated nanophotonic sensor based on a silicon nanowire based directional coupler [17]. From coupled mode theory we know

that the coupling efficiency changes as function of the gap distance between two silicon waveguides. Here, the in-plane displacement is achieved using an ultrasmall electrostatic comb actuator. The proposed device is capable of producing sub-100 nm displacement with a relatively low noise level resolution at a magnitude of 0.172 nm/$\sqrt{Hz}$. As the design can be easily fabricated with conventional SOI micromachining techniques, it may potentially be used in compact, low power high sensitivity, fast displacement sensing applications.

1.3 CMOS-MEMS integration

Over the last decades, CMOS (complementary metal oxide semiconductor) technology has become by far the predominant fabrication technology for integrated circuits (IC). Tremendous efforts have been made to continuously improve process yield and reliability, while minimal feature sizes and fabrication cost continue to decrease. Semiconductor roadmaps show the current state and, more important, outlines the future performance of CMOS technology with ever increasing integration density and decreasing feature sizes.

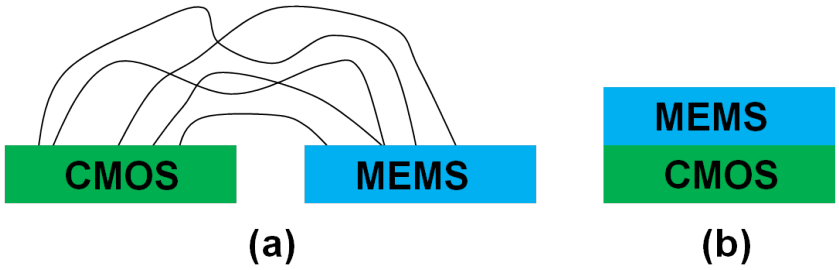

Figure 1.10: Hybrid (a) and Monolithic approach (b) of integration of MEMS and CMOS [18].

Nowadays, the power of CMOS technology is not only exploited for ICs but also for a variety of microsensors and microelectromechanical systems (MEMS) benefiting from well established fabrication technologies. Particularly, integration of the MEMS devices with the integrated circuit becomes increasingly important for compactness and performance reasons [19, 20]. The majority of current MEMS products on the market, is still using a hybrid approcah (Fig. 1.10a) where MEMS and CMOS are fabricated separately and connected through wirebonds. The advantage of the hybrid approach is its modular nature which has a much shorter development time as compared to the monolithic approach. Also it allows for an independent optimization of the CMOS and the MEMS technology. On the other hand, the assembly and packaging cost also rises with increasing degree of integration. Furthermore, with MEMS and electronic circuits on

separate chips, the parasitic capacitance and resistance of interconnects, bond pads, and bond wires can attenuate the signal and add significant noise [19].

Therefore, using a monolithic approach (Fig. 1.10b) to fabricate the MEMS devices directly on top of the CMOS metal interconnects will result in a reduction of the parasitics which will improve the system performance and will also help to further miniaturize the devices. At the same time, once volumes become high enough, the longer development time needed for the monolithic approach is more likely to be paid back by the reduced assembly and packaging cost.

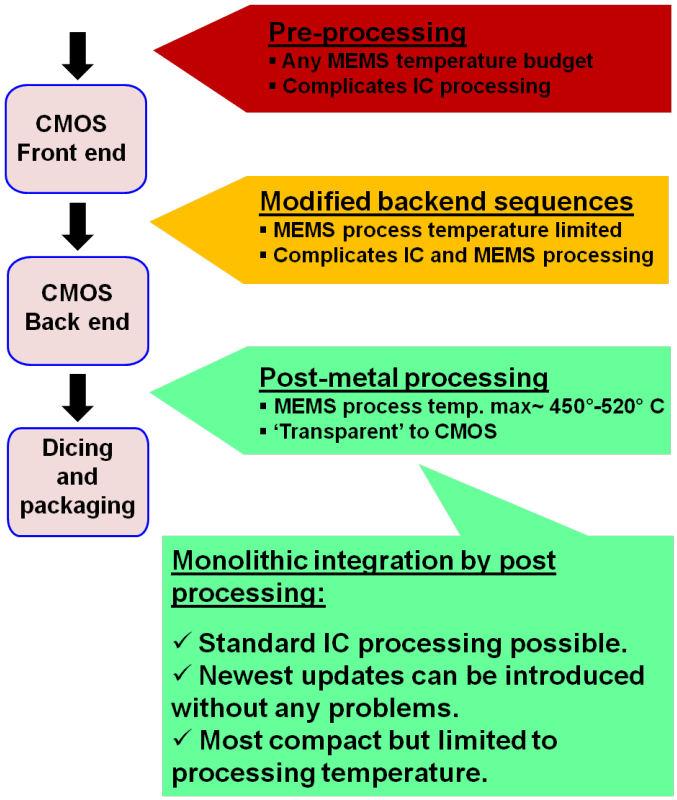

Figure 1.11: Three different approaches that can be used in monolithic integration of MEMS with CMOS [18].

The requirement of CMOS compatibility as discussed in [21], in practice results in CMOS being the dominant technology. This means that the MEMS devices have to adapt to the CMOS process and not the other way around. Still, this leaves three different options for producing CMOS-MEMS systems:

- Pre-CMOS Micromachining, where the microsystems are processed before the CMOS [22].

- Intra-CMOS Micromachining, where the CMOS and MEMS fabrication processes are inter-mixed [23, 24].

- Post-CMOS Micromachining, where the CMOS is processed before the MEMS and the MEMS is typically on top of the CMOS [25–28].

The pre-CMOS fabrication module neither interrupts the CMOS process, nor does it place any constraints on the thermal budget of the MEMS process. There are many choices of CMOS technologies, but this approach requires much development and preparation of the micromachined wafers. The major hurdles of the pre-CMOS approach include the MEMS topography which can compromise subsequent state-of-the art CMOS lithography steps. Also, it results into larger die areas due to the fact that the MEMS and CMOS devices cannot be easily stacked and the fact that integrated circuits foundries are usually not inclined to accept pre-processed wafers because of material compatibility and contamination issues. In addition to this, there will most probably be a requirement of post-CMOS processing in order to release the MEMS devices. Considering all these constraints, this is not a favorable technology.

The intra-CMOS fabrication module brings many constraints to the CMOS processing, thus making it harder to proceed to more advanced technologies. In addition, in this case it almost always required to have fabrication of CMOS and MEMS at the same foundry. The critical factor is the high temperature steps required for fabrication of microstructures, which may violate the allowable thermal budget of the CMOS process. Hence, this fabrication module is also not favorable.

Post-CMOS microfabrication is the most flexible fabrication module, especially because the CMOS and the MEMS circuits can be processed separately. The advantages of post-CMOS processing are:

- The MEMS structure may be placed on top or besides the CMOS circuitry.

- The CMOS process can easily adapt to new generations of electronics, which e.g. allows to reduce the area of the required electronics drive circuits, without requiring expensive re-qualification of the CMOS process. [29].

- It is possible to use two different foundries for the CMOS and MEMS circuits.

The primary constraint for the post-CMOS integration is that the CMOS process introduces a maximum temperature which the MEMS fabrication module must stay below. This thermal budget is determined by the metallization layers

of the transistors which is mostly Copper and Aluminum. Because Al can withstand temperatures only till approximately 450° C, poly-Si (deposition temperature of 800° C) cannot be used any further as a MEMS material for post-CMOS processing.

1.3.1 Poly-SiGe technology

As an alternative, Poly-SiGe has been proven to provide the necessary mechanical properties and reliability required for MEMS applications while requiring a significantly lower processing temperature compared to poly-Si (i.e. deposition temperature of ≤ 450°C instead of ≥ 800 °C). This makes poly-SiGe technology to be highly suitable for post CMOS integration of MEMS [30]. Hence, in IMEC's 200 mm fab, a dedicated poly-SiGe above-IC MEMS platform has been set up to integrate MEMS devices and their readout and driving electronics on the same chip. The SiGe MEMS platform consists of a number of standard modules: a CMOS protection layer, vias between the MEMS and CMOS layer, a poly-SiGe electrode, anchors, a poly-SiGe structural layer and an optional thin-film poly-SiGe packaging module (Fig. 1.12). These modules can be processed at a maximum temperature of 450° C, above standard CMOS, avoiding any degradation of the circuit functionality. Extra modules (optical coating, piezoresistive probes) can be added depending on the functionality that is needed. Both the electrode and the structural layer are in-situ B-doped and can have two different thicknesses within the same design.

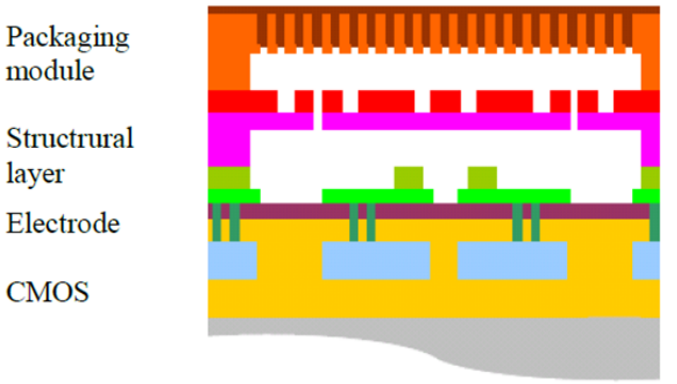

Figure 1.12: Different modules provided by IMEC as a part of the SiGe platform [31].

With this platform, several successful demonstrators have been built already. Examples are an integrated gyroscope for automotive applications [32],

a reliable 11 megapixel micro-mirror array for high-end industrial applications [31, 33] and a cantilever array for probe-based data storage [34].

In the Flemish IWT SBO project GEMINI (Generic Electronics and Microsystems INtegration Initiative) [35], the possibilities of this platform have been explored further. In Gemini, three different demonstrators were realized: mirrors for display applications (CMST, Ghent University), grating light valves (Photonics Research Group, Ghent University) and accelerometers (ESAT, K.U.Leuven). Whereas the mirrors and GLVs are realized with a ~300 nm thick SiGe structural layer (+ optional 5 nm SiC/30 nm Al coating for improved reflectivity), the SiGe structural layer thickness for the accelerometers is 4 μm to improve the capacitive readout of in-plane devices.

1.4 Grating couplers for coupling light to nanophotonic waveguides

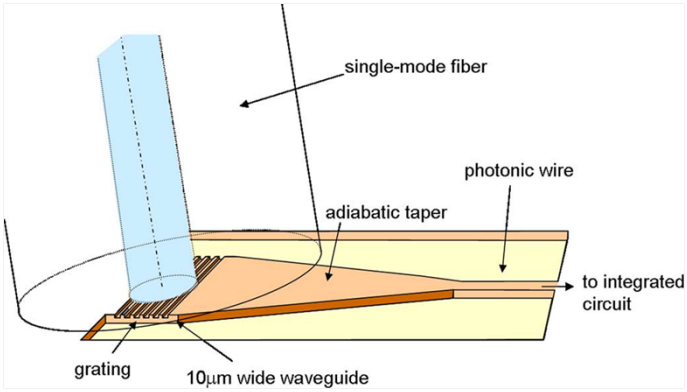

Figure 1.13: Schematic representation of a grating coupler which can be used to couple incoming/outgoing light from/ to an optical fiber [36].

Coupling of light between a single mode fiber and nanophotonic circuits remains a serious issue in integrated optics. The large difference in dimensions between the fiber and the waveguides on a chip causes high insertion losses and high packaging costs. The ongoing trend to make components smaller, in order to integrate them on a single chip, makes the problem even more difficult. The key features of an effective solution are compactness, low insertion loss, large alignment tolerance and broadband operation. However, use of grating couplers for out-of-plane coupling between a standard single-mode fiber and waveguide have become more and more popular with time. The approach has major advantages over edge-coupling methods. There is no need for a cleaved

facet and light can be coupled in and out everywhere on the chip, opening the way for wafer-scale testing.

A coupling efficiency (for 1.55 μm wavelength) to single-mode fiber of 33% for a 10 x 10 μm^2 grating coupler in silicon-on-insulator (SOI) was demonstrated [37] by Taillaert *et al*, where the angle (θ) between the fiber and the normal to the grating was optimized at 10°. But, a misalignment of only ±2 μm from the optimal position already results in an additional coupling loss of 1.0 dB at the same wavelength [38]. At the same time, the central wavelength exhibiting maximum coupling shifts approximately 9 nm per degree of change in θ. This clearly shows how sensitive the coupling efficiency is with regard to slight misalignment between the two components (grating and fiber). This makes it very difficult to achieve efficient coupling using a purely passive alignment technique. Hence, there is a need for new concepts which allow the fiber or the grating coupler to be actively adjusted with sub μm precision either in-plane or out-of-plane and thereby find the best coupling efficiency.

In the second part of this thesis, we will propose a concept which has the potential to successfully mitigate the alignment problem using MEMS to actively control the position or the angle of the grating coupler with respect to the optical fiber.

1.5 Objectives of this work and thesis outline

The core of this thesis is related to the investigation of different kinds of optical MEMS systems. Being a part of the GEMINI project, we used poly-SiGe as a structural material to form different types of diffractive MOEMS systems and characterized the quality of the devices which in turn gives feedback on the usability of poly-SiGe in fabricating high quality MEMS devices. In addition, we investigated integrated optical micro systems integrated on a silicon photonics integrated waveguide platform which can be employed in solving misalignment issues between an optical fiber and a grating coupler.

In chapter 2, we introduce the theory of the bending of a microbeam which we use later to determine the electromechanical properties of our MEMS devices. The importance of the squeezed film damping phenomenon is described in detail which has a significant effect on the dynamic properties of our MEMS devices. Standard device characterization techniques of optical interferometry and laser doppler vibrometry are described thoroughly. In this chapter, we also provide an in detail description of the GEMINI process flow which was developed solely in imec (without any contribution from the PhD candidate's side) to fabricate the poly-SiGe devices.

In chapter 3, we mainly deal with Grating Light Valves (GLV). Our devices are significantly different in specs from their earlier counterparts because of the

different properties of poly-SiGe compared to the Silicon Nitride used by Silicon Light Machines as a structural material. We also investigated other geometries which give better and more reliable performance for the fabricated GLV devices. Other than concentrating only on the nature of the optical output, we gave equal importance to investigating the dynamic properties of the GLVs which are extremely important in overall qualification of the fabricated devices.

In chapter 4, we demonstrated another kind of MEMS gratings which are based on a similar working principle as the GLVs, but instead, have a 2D structure. Due to their planar symmetry, these gratings are more insensitive to the incident polarization.

In chapter 5, we investigated integrated waveguide based microsystems with the goal of reaching dynamic beam steering and thereby solving fiber to photonic circuit or VCSEL to photonic circuit alignment problems. Our approach involved the grating coupler which is used to couple incoming/ outgoing light in between an optical fiber and a silicon photonic waveguide. We investigated two different approaches: (i) the grating coupler is tilted out-of-plane to direct the outgoing light in several directions, (ii) we attached the grating coupler with nanoscale combs to laterally translate the outgoing light in orthogonal directions in the same plane.

Finally, we draw our conclusion on the overall work described in this thesis and propose some improvements that can be implemented in the future to make the devices better.

1.6 Publications

The results obtained in the framework of this work is published in three peer reviewed journals and were presented at other international conferences.

Publications in international journals

1. S. Rudra, R. Van Hoof, J. De Coster, G. Bryce, S. Severi, A. Witvrouw, and D. Van Thourhout, "A 2D MEMS grating based CMOS compatible poly-SiGe variable optical attenuator", Microelectronic Engineering, vol. 105, pp. 8-12, 2013.

2. S. Rudra, J. De Coster, R. Van Hoof, G. Bryce, S. Severi, A. Witvrouw, and D. Van Thourhout, "Static and dynamic characterization of pull-in protected CMOS compatible poly-sige grating light valves", Sensors and Actuators A: Physical, vol. 179, pp. 283-290, 2012.

3. S. Rudra, J. Roels, G. Bryce, L. Haspeslagh, A. Witvrouw, and D. Van Thourhout, "SiGe based grating light valves: A leap towards monolithic

integration of MOEMS", Microelectronic Engineering, vol. 87, no. 5-8, pp. 1195-1197, 2010.

Publications at international conferences

1. S. Rudra, J. De Coster, R. Van Hoof, A. Witvrouw, D. Van Thourhout, Static and dynamic characterization of poly-SiGe Grating Light Valves,IEEE Optical MEMS and Nanophotonics 2011, Turkey, p.203-204 (2011)

2. A. Witvrouw, R. Van Hoof, G. Bryce, B. Du Bois, A. Verbist, S. Severi, L. Haspeslagh, H. Osman, J. De Coster, L. Wen, R. Puers, R. Beernaert, H. De Smet, S. Rudra, D. Van Thourhout, SiGe MEMS technology: a Platform Technology Enabling Different Demonstrators,218th ECS Meeting, Las Vegas, NV (invited), 33(6), United States, p.799-812 (2010).

3. S. Rudra, J. Roels, G. Bryce, S. Severi, A. Witvrouw, R. Baets, D. Van Thourhout, Grating light valves: a SiGe based approach towards monolithic integration of MOEMS,Proceedings of the 2009 Annual Symposium of the IEEE Photononics Benelux Chapter, Belgium, p.109-112 (2009).

References

[1] S. Beeby, G. Ensell, M. Kraft, and N. White, "Mems mechanical sensors. artech house," *Inc. Boston, London*, pp. 104–105, 2004.

[2] M. Douglass, "Lifetime estimates and unique failure mechanisms of the digital micromirror device (dmd)," in *Reliability Physics Symposium Proceedings, 1998. 36th Annual. 1998 IEEE International*. IEEE, 1998, pp. 9–16.

[3] W. Bailey and J. Baker, "Fabrication method for digital micro-mirror devices using low temperature cvd," Jun. 18 1996, uS Patent 5,526,951.

[4] J. Choi, "Method for manufacturing digital micro-mirror device (dmd) packages," Apr. 13 2004, uS Patent 6,720,206.

[5] H. Liu and B. Bhushan, "Nanotribological characterization of digital micromirror devices using an atomic force microscope," *Ultramicroscopy*, vol. 100, no. 3, pp. 391–412, 2004.

[6] L. Hornbeck, "The dmdŹ projection display chip: a mems-based technology," *Mrs Bulletin*, vol. 26, no. 4, pp. 325–327, 2001.

[7] "Optical circuit switching relieves inter-cluster congestion in datacenter networks." [Online]. Available: http://www.calient.net/wp-content/uploads/downloads/2012/12/The-Hybrid-Packet-OCS-Datacenter-Network-Final-12_29_12.pdf

[8] X. Zheng, V. Kaman, S. Yuan, Y. Xu, O. Jerphagnon, A. Keating, R. C. Anderson, H. N. Poulsen, B. Liu, J. R. Sechrist *et al.*, "Three-dimensional mems photonic cross-connect switch design and performance," *Selected Topics in Quantum Electronics, IEEE Journal of*, vol. 9, no. 2, pp. 571–578, 2003.

[9] "http://mems.sandia.gov/tech-info/doc/isa98.pdf."

[10] C. Chui, P. D. Floyd, D. Heald, B. Arbuckle, A. Lewis, M. Kothari, B. Cummings, L. Palmateer, J. Bos, D. Chang *et al.*, "The imod display: considerations and challenges in fabricating moems on large area glass substrates," in *MOEMS-MEMS 2007 Micro and Nanofabrication*. International Society for Optics and Photonics, 2007, pp. 646 609–646 609.

[11] M. Miles, "Large area manufacture of mems based displays," in *Symposium on Design, Test, Integration and Packaging of MWMS/MOEMS*, 2004, pp. 313–316.

[12] B. Gally, "P-103: Wide-gamut color reflective displays using imodŹ interference technology," in *SID Symposium Digest of Technical Papers*, vol. 35, no. 1. Wiley Online Library, 2012, pp. 654–657.

[13] D. Bloom *et al.*, "The grating light valve: revolutionizing display technology," in *Proc. SPIE*, vol. 3013, 1997, pp. 165–171.

[14] D. Amm and R. Corrigan, "Grating Light Valve Technology: Update and Novel Applications," in *SID Symposium Digest of Technical Papers*, vol. 29, no. 1, 1998, p. 29.

[15] J. Trisnadi, C. Carlisle, and R. Monteverde, "Overview and applications of Grating Light ValveTM based optical write engines for high-speed digital imaging," in *Proc. SPIE*, vol. 5348, 2004, pp. 1–13.

[16] S. Abdulla, L. Kauppinen, M. Dijkstra, M. de Boer, E. Berenschot, H. Jansen, R. De Ridder, and G. Krijnen, "Tuning a racetrack ring resonator by an integrated dielectric mems cantilever," *Optics express*, vol. 19, no. 17, pp. 15 864–15 878, 2011.

[17] X. Chew, G. Zhou, and F. Chau, "Nanomechanically suspended low-loss silicon nanowire waveguide as in-plane displacement sensor," *Journal of Nanophotonics*, vol. 6, no. 1, pp. 063 505–1, 2012.

[18] A. Witvrouw, "CMOS-MEMS integration today and tomorrow," *scripta materialia*, vol. 59, no. 9, pp. 945–949, 2008.

[19] C. Van Hoof, K. Baert, and A. Witvrouw, "The best materials for tiny, clever sensors," *Science*, vol. 306, no. 5698, pp. 986–987, 2004.

[20] R. Howe and T. King, "Low-temperature lpcvd mems technologies," in *MATERIALS RESEARCH SOCIETY SYMPOSIUM PROCEEDINGS*, vol. 729. Cambridge Univ Press, 2002, pp. 205–214.

[21] H. Baltes, O. Brand, G. Fedder, C. Hierold, J. Korvink, and O. Tabata, *CMOS-MEMS: Advanced Micro and Nanosystems*. Wiley-VCH, 2008.

[22] L. Parameswaran, C. Hsu, and M. Schmidt, "A merged mems-cmos process using silicon wafer bonding," in *Electron Devices Meeting, 1995., International*. IEEE, 1995, pp. 613–616.

[23] C. Hierold, "Intelligent cmos sensors," in *Micro Electro Mechanical Systems, 2000. MEMS 2000. The Thirteenth Annual International Conference on*. IEEE, 2000, pp. 1–6.

[24] K. Chau, S. Lewis, Y. Zhao, R. Howe, S. Bart, and R. Marcheselli, "An integrated force-balanced capacitive accelerometer for low-g applications," in *Proc. 8th Int. Conf. Solid-State Sensors and Actuators (TransducersŠ 95)*, 1995, pp. 25–29.

[25] P. Van Kessel, L. Hornbeck, R. Meier, and M. Douglass, "A mems-based projection display," *Proceedings of the IEEE*, vol. 86, no. 8, pp. 1687–1704, 1998.

[26] S. Michaelis, H. Timme, M. Wycisk, and J. Binder, "Acceleration threshold switches from an additive electroplating mems process," *Sensors and Actuators A: Physical*, vol. 85, no. 1, pp. 418–423, 2000.

[27] A. Haberli, O. Paul, P. Malcovati, M. Faccio, F. Maloberti, and H. Baltes, "Cmos integration of a thermal pressure sensor system," in *Circuits and Systems, 1996. ISCAS'96., Connecting the World., 1996 IEEE International Symposium on*, vol. 1. IEEE, 1996, pp. 377–380.

[28] A. Schaufelbuhl, N. Schneeberger, U. Munch, M. Waelti, O. Paul, O. Brand, H. Baltes, C. Menolfi, Q. Huang, E. Doering *et al.*, "Uncooled low-cost thermal imager based on micromachined cmos integrated sensor array," *Microelectromechanical Systems, Journal of*, vol. 10, no. 4, pp. 503–510, 2001.

[29] X. Zhu, S. Santhanam, H. Lakdawala, H. Luo, and G. Fedder, "Copper interconnect low-k dielectric post-cmos micromachining," in *11th Int. Conf. Solid State Sensors and Actuators*, 2001, pp. 1549–1551.

[30] P. Gonzalez, B. Guo, M. Rakowski, K. De Meyer, and A. Witvrouw, "Cmos compatible polycrystalline silicon-germanium based pressure sensors," *Sensors and Actuators A: Physical*, vol. 188, pp. 9–18, 2011.

[31] A. Witvrouw, L. Haspeslagh, O. Pedreira, J. De Coster, I. De Wolf, H. Tilmans, T. Bearda, B. Schlatmann, M. van Bommel, M. de Nooijer *et al.*, "11-megapixel cmos-integrated sige micromirror arrays for high-end applications," *Microelectromechanical Systems, Journal of*, vol. 19, no. 1, pp. 202–214, 2010.

[32] A. Scheurle, T. Fuchs, K. Kehr, C. Leinenbach, S. Kronmuller, A. Arias, J. Ceballos, M. Lagos, J. Mora, J. Muñoz *et al.*, "A 10 μm thick poly-sige gyroscope processed above 0.35 μm cmos," in *Micro Electro Mechanical Systems, 2007. MEMS. IEEE 20th International Conference on*. IEEE, 2007, pp. 39–42.

[33] L. Haspeslagh, J. De Coster, O. Pedreira, I. De Wolf, B. Du Bois, A. Verbist, R. Van Hoof, M. Willegems, S. Locorotondo, G. Bryce *et al.*, "Highly reliable cmos-integrated 11mpixel sige-based micro-mirror arrays for high-end industrial applications," in *Electron Devices Meeting, 2008. IEDM 2008. IEEE International*. IEEE, 2008, pp. 1–4.

[34] J. Heck, D. Adams, N. Belov, T. Chou, B. Kim, K. Kornelsen, Q. Ma, V. Rao, S. Severi, D. Spicer *et al.*, "Ultra-high density mems probe memory device," *Microelectronic Engineering*, vol. 87, no. 5, pp. 1198–1203, 2010.

[35] "Iwt-sbo project gemini (generic electronics and microsystems integration initiative) iwt-nr 60046„" Tech. Rep., 2007-2011.

[36] D. Taillaert, "Grating couplers as interface between optical fibres and nanophotonic waveguides," Ph.D. dissertation, Ghent University, 11/2004.

[37] D. Taillaert, R. Baets, P. Dumon, W. Wim Bogaerts, D. Van Thourhout, B. Luyssaert, V. Wiaux, S. Beckx, and J. Wouters, "Silicon-on-insulator platform for integrated wavelength-selective components," in *Fibres and Optical Passive Components, 2005. Proceedings of 2005 IEEE/LEOS Workshop on*. IEEE, 2005, pp. 115–120.

[38] D. Taillaert, F. Van Laere, M. Ayre, W. Bogaerts, D. Van Thourhout, P. Bienstman, and R. Baets, "Grating couplers for coupling between optical fibers and nanophotonic waveguides," *Jpn. J. Appl. Phys*, vol. 45, no. 8A, pp. 6071–6077, 2006.

2

Electro-Mechanics of the MEMS structures and GEMINI Process Flow

2.1 Introduction

In this chapter we will focus on the electromechanical properties of microbeams. First, a short introduction will be given regarding beam theory and interaction with an electric field. Later, we will introduce the basics of microfluidics and how it influences MEMS structures. Though most of the content of this chapter is readily available in literature, further introductory explanations will help the reader to understand the experimental results described later in the thesis. We first discuss the static behavior of a beam under an electrostatic force and will check how the residual stress in the structure influences the deformed shape and its vibrational properties. Afterwards, we will introduce the squeezed film damping phenomenon which influences the MEMS operation and how it can be optimized to our advantage. Later, we talk about the processing steps that were used in imec to fabricate our poly-SiGe based MEMS devices and using the previously described beam theory, we will deduce the elastic properties of the fabricated structures. Lastly, we will give a very short description of the optical profilometry and Laser Doppler Vibrometry (LDV), which we used intensively to characterize the static and dynamic properties of the MEMS devices.

2.2 Bending of a beam

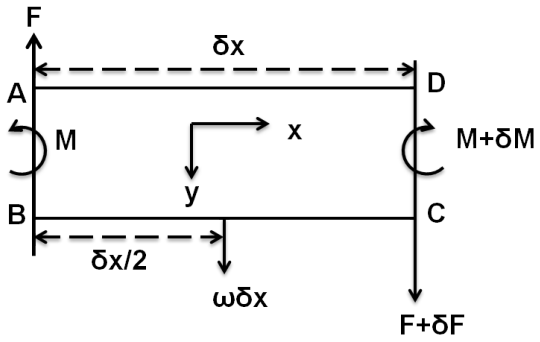

Figure 2.1: Distribution of the force and bending moment over the section of a beam of length δx.

Let us consider an element of a beam as shown in Fig. 2.1, the left edge of which is at a distance x from the origin and the right edge at a distance x+δx as shown in Fig. 2.1. The shearing stress at the left edge is F and at the right edge is F+ δF during upward displacement of the element. The corresponding internal resisting moment at the left face due to the left hand portion of the beam is M in the counter clockwise direction and at the right face of the beam is M+ δM in the clockwise direction.To attain, vertical equilibrium of the element δx, the force equation becomes:

$$F - \omega\delta x - (F + \delta F) = 0 \tag{2.1}$$

where ω is the distributed load or the force per unit length of the beam. Hence, in the limit δx–> 0, we get:

$$\frac{dF}{dx} = -\omega \tag{2.2}$$

Considering the moment equation (taking moments about A since there is no rotation) we may write:

$$M - \omega\delta x\frac{\delta x}{2} - (M + \delta M) - (F + \delta F)\delta x = 0 \tag{2.3}$$

in the limit δx–> 0, we get:

$$\frac{dM}{dx} = -F \tag{2.4}$$

and hence, finally by coupling eq. 2.3 and eq. 2.4 we can write:

$$\frac{d^2M}{dx^2} = \omega \tag{2.5}$$

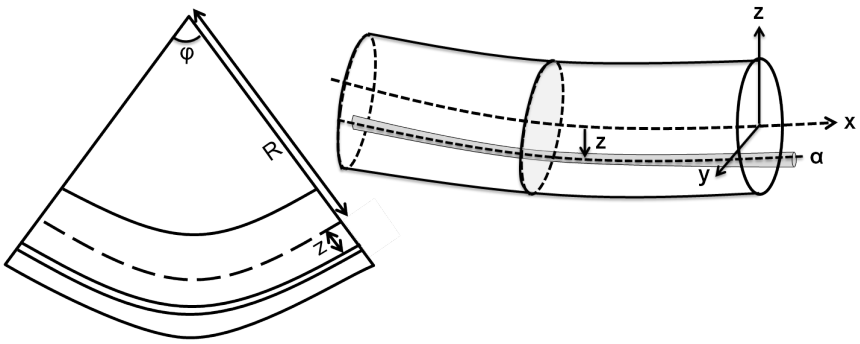

Figure 2.2: Distribution of different filaments over the length of a bent beam.

Now, if we consider a portion of a bent beam and imagine the beam to be divided in straight parallel longitudinal filaments, then the strain at a small height z from the neutral axis [1] is given by $s = \frac{z\phi}{R\phi} = \frac{z}{R}$, where R is the radius of curvature of the neutral axis.

Let, α be the sectional area of the filament in Fig. 2.2 and f be the longitudinal force that comes to play across the section of the filament to resist elongation. Then we have, f= $\frac{Y\alpha z}{R}$, where Y is the Young's modulus of the material of the beam. Hence, the internal bending moment of the whole beam is given by:

$$M = \Sigma f.z = \frac{Y}{R}\Sigma\alpha z^2 \tag{2.6}$$

But $\Sigma\alpha z^2$ signifies the geometric moment of inertia (I) of the section of the beam about the axis passing through the center of the section and for small bending we can write: $\frac{1}{R} = \frac{d^2h}{dx^2}$ [2], where h(x) is the deflection of the beam in the z direction at some point x.

Hence, combining the equations we obtain:

$$YI\frac{d^4h}{dx^4} = \omega \tag{2.7}$$

Now, if we consider a uniformly loaded low-stress fixed-fixed beam of length l, width b and thickness t with ω as the force per unit length of the beam, then the deflection h, at a point x of the beam can be given as (by solving eq. 2.7):

$$h = \frac{\omega}{24YI}x^2(l-x)^2 \tag{2.8}$$

For a rectangular beam, it can be shown that the moment of inertia is given by, $I = \frac{bt^3}{12}$ [3], and hence, the deflection curve takes the form [4, 5]:

$$h = \frac{q}{2Yt^3}x^2(l-x)^2 \tag{2.9}$$

where q is the spatially uniform and temporally harmonically varying force per unit area (the applied pressure).

If, due to a particular deposition condition of the material, the rectangular beam has a large built-in tensile stress, then the stored potential energy in the ribbon is mostly due to elongation, and hence its deflection curve can be expressed as [6, 7]:

$$h = \frac{q}{t\sigma} x(l-x) \tag{2.10}$$

where, σ is the tensile stress in the beam.

The deflection shapes given by the two different equations are shown in Fig. 2.3. It can be seen that the stress dominated beam has a much flatter central part than the bending dominated beam.

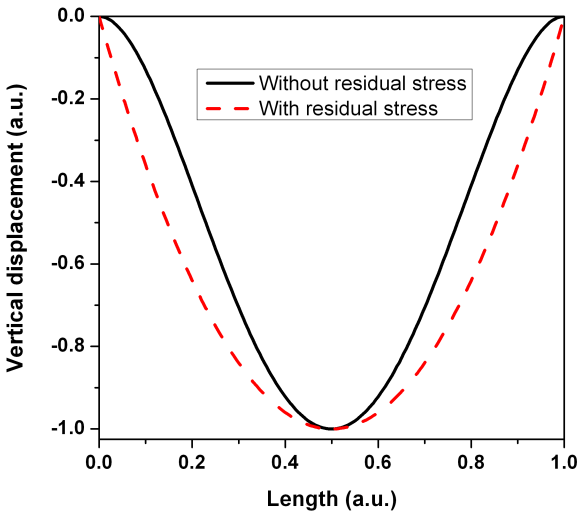

Figure 2.3: Deflection curves for beams without any residual stress and with residual stress.

2.3 Electro-mechanics of the MEMS structures

The electromechanical behavior of the fixed-fixed microbeams (as used in our MEMS structures) can be described by the spring-capacitor model as shown in Fig. 2.4. For a fixed-fixed beam with tensile stress the spring constant (k) is given by [7]:

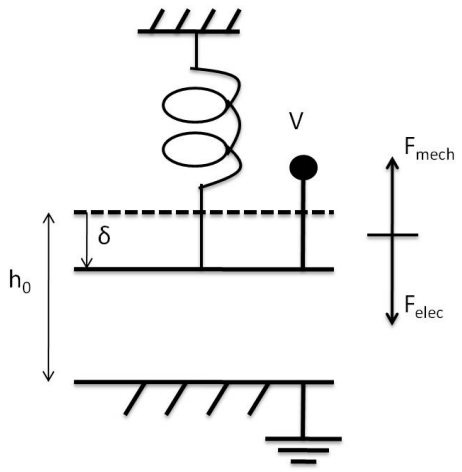

Figure 2.4: Spring-capacitor model resembling the operation of a GLV microbeam.

$$k = 32Ew\left(\frac{t}{l}\right)^3 + 8\sigma(1-\nu)w\left(\frac{t}{l}\right) \tag{2.11}$$

where, E is the Young's modulus, ρ is the specific mass, ν is the Poisson's ratio, σ is the tensile stress, w is the width, t is the thickness and l is the length and m is the mass of the microbeams.

If the residual stress within the beam is compressive then the above formula is not valid anymore. The primary concern with compressive stress is the tendency of the beam to buckle. Due to the inherent stiffness of the beam, a certain amount of the compressive stress can be tolerated before the buckling occurs. This compressive stress is known as the critical stress and for a fixed-fixed beam it is be given as [8]:

$$\sigma_{cr} = \frac{\pi^2 E t^2}{3l^2(1-\nu)} \tag{2.12}$$

Hence, a shorter beam can tolerate higher compressive stress but the shortcoming is that the actuation voltage becomes even higher. When a voltage is applied, the plate on top is pulled towards the bottom electrode by the Coulomb force. If we consider a plate of width w and length l is displaced by a distance δ due to an applied voltage of V w.r.t. the bottom electrode, then by equating the applied electrostatic force [9] with the mechanical restoring force due to the stiffness of the beam (F = kx), we can write:

$$\frac{1}{2}\frac{\epsilon_0 wl}{(h_0-\delta)^2}V^2 = k\delta \tag{2.13}$$

$$V = \sqrt{\frac{2k}{\epsilon_0 w l}\delta\,(h_0-\delta)^2} \tag{2.14}$$

Now, if we plot the gap spacing between the plate and the bottom electrode as shown in Fig. 2.5, then it shows two possible solutions for a single applied voltage. This is due to the fact that after $\delta > \frac{h_0}{3}$, the electrostatic force is greater than the restoring force, resulting in (i) the beam position becoming unstable and (ii) collapse of the beam on top of the bottom electrode. This phenomenon is known as pull-in [4, 7].

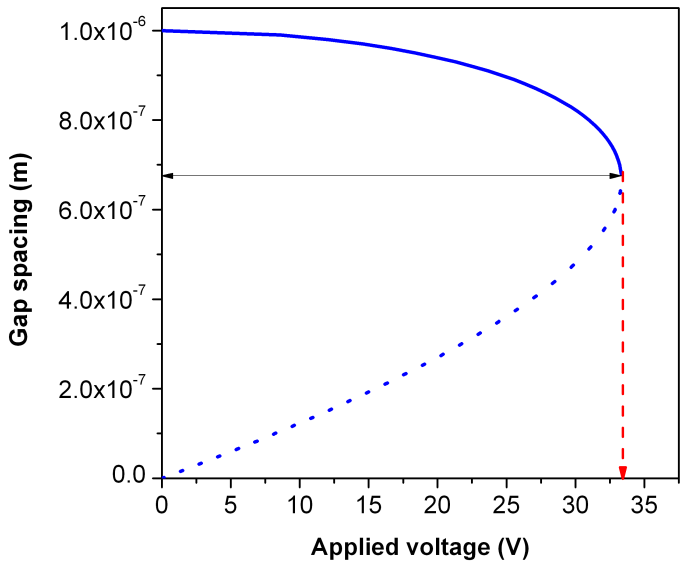

Figure 2.5: Gap spacing vs applied voltage for a fixed-fixed microbeam with w= 5 μm, l= 50 μm, t = 300 nm, E= 120 GPa, σ= 20 MPa and h_0 = 1 μm. The dashed line represents the unstable region of the beam.

Another important parameter for a fixed-fixed beam is the resonance frequency which determines its fastest achievable modulation rate. And for a beam with the above mentioned details, the resonance frequency (ω_r) is given by [10]:

$$\omega_r = \frac{\alpha^2}{\sqrt{12}}\frac{t}{l^2}\left(\frac{E}{\rho\left(1-\nu^2\right)}\right)^{0.5}\left(1+\gamma\left(\frac{\sigma\left(1+\nu^2\right)}{E}\right)\frac{l^2}{t^2}\right)^{0.5} \tag{2.15}$$

where, α = 4.73 and γ= 0.295. It is clear from the above equation that though the resonance frequency is independent of the width, it is strongly dependent on the length and thickness of the microbeams. At the same time, the higher the tensile stress within the structures, the faster will be the modulation rate of the devices.

2.4 Effects of air damping on microstructures

It can be shown that the drag force applied to a sphere moving in a viscous fluid at a speed of v is F= $6\pi\mu r v$ [11], where μ is the coefficient of viscosity of the fluid and r is the radius of the sphere. The ratio between the drag force F and the mass of the body, M, is given by:

$$\frac{F}{M} = \frac{6\pi\mu r v}{4\pi r^3 \rho/3} = \frac{4.5\mu v}{\rho r^2} \tag{2.16}$$

It is obvious from the above equation that the smaller the dimension, the more important is the drag force on the body. If we consider two spheres of radius of 1 cm and 1 μm respectively, made of the same material, then the drag force by mass ratio on the smaller sphere is a million times larger than that exerted on the bigger one. Hence, while the drag force caused by viscosity of the surrounding air is usually negligible for conventional macro-structures, it plays a crucial role in the motion of microstructures. Therefore, in the next section we will discuss in detail on how the viscous forces influence the motion of our microbeams and how we can tailor it to our advantage.

2.5 Viscous forces in MEMS

In general, in any flow, different layers move with different velocities and the fluid's viscosity [12] arises from the shear stress between the layers that ultimately oppose any applied force. The internal shear force in a steady flow of a viscous fluid is proportional to the velocity gradient. If the flow velocity u, in the X direction is a function of Y, then the shear force is given by

$$\tau_{yx} = \mu \frac{\partial u(y)}{\partial y} \tag{2.17}$$

where, μ is the coefficient of viscosity of the fluid.

If we consider a cubic element in a moving fluid as shown in Fig. 2.6, then it suffers shear forces on each of its six surfaces because of the velocity gradient in the flow, which are given by: $\tau_{xy}(x)dydz$, $\tau_{xy}(x+dx)dydz$, $\tau_{yz}(y)dzdx$, $\tau_{yz}(y+dy)dzdx$, $\tau_{zx}(z)dxdy$, $\tau_{zx}(z+dz)dxdy$, $\tau_{xz}(x)dydz$, $\tau_{xz}(x+dx)dydz$, $\tau_{yx}(y)dzdx$, $\tau_{yx}(y+dy)dzdx$, $\tau_{zy}(z)dxdy$, $\tau_{zy}(z+dz)dxdy$. Additionally,

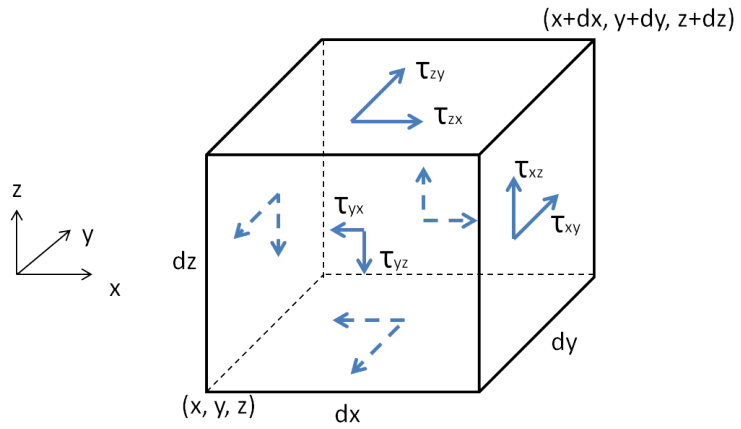

Figure 2.6: Shearing forces on the different sides of a cube in a viscous flow.

there are also six normal force components on its surfaces caused by pressure: $P(x)dydz$, $P(x+dx)dydz$, $P(y)dzdx$, $P(y+dy)dzdx$, $P(z)dxdy$,$P(z+dz)dxdy$.

Then for a steady flow, assuming the weight of the fluid is negligible, the force balance for the cube in the z-direction is:

$$[P(z+dz)-P(z)]dxdy = [\tau_{xz}(x+dx)-\tau_{xz}(x)]dydz+[\tau_{yz}(y+dy)-\tau_{yz}(y)]dxdz \tag{2.18}$$

Then, we obtain:

$$\frac{\partial P}{\partial z} = \frac{\partial \tau_{xz}}{\partial x} + \frac{\partial \tau_{yz}}{\partial y} \tag{2.19}$$

But, if we consider u, v and w to be the velocity component in the x, y and z directions respsectively, then we get: $\tau_{xz} = \mu\frac{\partial w}{\partial x}$ and $\tau_{yz} = \mu\frac{\partial w}{\partial y}$. And hence:

$$\frac{\partial P}{\partial z} = \mu\left(\frac{\partial^2 w}{\partial x^2} + \frac{\partial^2 w}{\partial y^2}\right) \tag{2.20}$$

Similarly,

$$\frac{\partial P}{\partial x} = \mu\left(\frac{\partial^2 u}{\partial y^2} + \frac{\partial^2 u}{\partial z^2}\right) \tag{2.21}$$

$$\frac{\partial P}{\partial y} = \mu\left(\frac{\partial^2 v}{\partial z^2} + \frac{\partial^2 v}{\partial x^2}\right) \tag{2.22}$$

For conventional bulk machines, the damping caused by surrounding air can be ignored because the energy dissipated by air damping is much less than the energy dissipated by other mechanisms. But in case of micro dimensional structures (MEMS), the surface to volume ratio is very high and hence a larger

part of the device is damped by the air which is a key factor behind their dynamic behavior.

2.5.1 Squeeze film damping

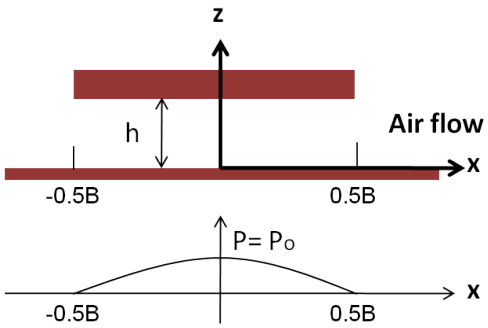

Figure 2.7: Pressure gradient created due to relative motion of two parallel plates separated by a small gap.

If we consider two parallel plates separated by a tiny gap which are moving towards each other, then, part of the air closer to the center of the gap is squeezed and a part of it flows away at the boundary. As a result, an additional pressure ΔP is created within the gap (Fig. 2.7) which restricts the motion of the plates. On the contrary, if the plates are moving away from each other then the pressure inside the gap is reduced to keep the air flowing into the gap. Hence, in both moving directions, the forces on the plates caused by the built-up pressure are always working against the movement of the plates. In short, the fluid medium in between the plates acts like a damper and this damping is known as squeeze-film damping [13, 14]. Depending on the application, the damping force should either be reduced or optimized to a desired level.

2.5.2 Reynold's equation

Suppose, that we have a pair of plates parallel with the x-y plane of the Cartesian coordinates as shown in Fig. 2.8 and the dimensions of the plates are much larger than the distance between them so that the gas flow between the plates caused by the relative motion of the plates is lateral (in the x- and y-direction but not in the z-direction).

Let us consider an elemental column, hdxdy (where $h = h_2 - h_1$), as shown in Fig. 2.8, where q_x is the flow rate in the x-direction per unit width in the

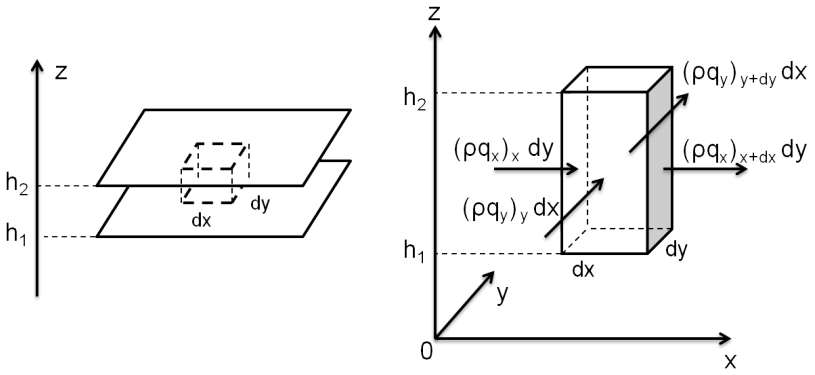

Figure 2.8: Pressure gradient created due to relative motion of two parallel plates separated by a small gap.

y-direction and q_y is the flow rate in the y-direction per unit width in the x-direction.

The balance of mass flow for the elemental column requires:

$$(\rho q_x)_x\,dy-(\rho q_x)_{x+dx}\,dy+(\rho q_y)_y\,dx-(\rho q_y)_{y+dy}\,dx=\left(\frac{\partial \rho h_2}{\partial t}-\frac{\partial \rho h_1}{\partial t}\right)dxdy \tag{2.23}$$

Again we can write:

$$(\rho q_x)_{x+dx}=(\rho q_x)+\left[\frac{\partial \rho q_x}{\partial x}\right]dx \tag{2.24}$$

$$(\rho q_y)_{y+dy}=(\rho q_y)+\left[\frac{\partial \rho q_y}{\partial y}\right]dy \tag{2.25}$$

By using the above equations, we can obtain:

$$\frac{\partial(\rho q_x)}{\partial x}+\frac{\partial(\rho q_y)}{\partial y}+\frac{\partial(\rho h)}{\partial t}=0 \tag{2.26}$$

To find q_x and q_y, we have to find the speed distribution in the z-direction first. As the dimensions of the plate are much larger than the gap and the flow is lateral, the velocity components u and v are functions of z only. From Eq. 2.21, we have:

$$\frac{\partial P}{\partial x}=\mu\left(\frac{\partial^2 u}{\partial z^2}\right) \tag{2.27}$$

For a small gap, P(x,y) is not a function of z. By integrating the equation twice, we have:

$$u(z) = \frac{1}{2\mu}\frac{\partial P}{\partial x}z^2 + C_1\frac{1}{\mu}z + C_2 \tag{2.28}$$

If the plates do not move laterally and we put the origin of the coordinates on the bottom plate, the boundary conditions for Eq. 2.28 are, u(0)=0, u(h)=0. Therefore:

$$u(z) = \frac{1}{2\mu}\frac{\partial P}{\partial x}z(z-h) \tag{2.29}$$

The flow rate in the x-direction for a unit width in the y-direction is:

$$q_x = \int_0^h u dz = -\frac{h^3}{12\mu}\frac{\partial P}{\partial x} \tag{2.30}$$

The negative sign in the equation indicates that the flow is in the direction with decreasing pressure. Similarly, we have:

$$q_y = -\frac{h^3}{12\mu}\frac{\partial P}{\partial y} \tag{2.31}$$

By substituting Eq. 2.30 and Eq. 2.31 into Eq. 2.26, we find

$$\frac{\partial}{\partial x}\left(\rho\frac{h^3}{\mu}\frac{\partial P}{\partial x}\right) + \frac{\partial}{\partial y}\left(\rho\frac{h^3}{\mu}\frac{\partial P}{\partial y}\right) = 12\frac{\partial(h\rho)}{\partial t} \tag{2.32}$$

Eq. 2.32 is referred to as Reynolds' equation. Eq. 2.32 can also be derived from the much more complicated Navier-Stokes equation under the condition that the Modified Reynolds' Number for a squeeze film, R_s, is much smaller than unity, i.e., the condition of $R_s = \frac{\omega h^2 \rho}{\mu} << 1$, where ω is the radial frequency of the oscillating plate. This condition is satisfied for typical silicon microstructures.

As h is assumed to be uniform both in the x- and y-directions, we have:

$$\frac{\partial}{\partial x}\left(\rho\frac{\partial P}{\partial x}\right) + \frac{\partial}{\partial y}\left(\rho\frac{\partial P}{\partial y}\right) = 12\frac{\mu}{h^3}\frac{\partial(h\rho)}{\partial t} \tag{2.33}$$

For an isothermal film, the air density, ρ, is proportional to pressure P, i.e., $\rho = \frac{P}{P_0}\rho_0$. The above equation can then be written as

$$\left(\frac{\partial P}{\partial x}\right)^2 + \left(\frac{\partial P}{\partial y}\right)^2 + P\left(\frac{\partial^2 P}{\partial x^2} + \frac{\partial^2 P}{\partial y^2}\right) = 12\frac{\mu}{h^3}\left(P\frac{dh}{dt} + h\frac{\partial P}{\partial t}\right) \tag{2.34}$$

Assuming that $h = h_o + \Delta h$ and $P = P_o + \Delta P$, for small motion distance of the plate, we have $\Delta h << h_o$ and $\Delta P << P_o$. Under these conditions, the equation can be approximated as:

$$P_0\left(\frac{\partial^2 \Delta P}{\partial x^2} + \frac{\partial^2 \Delta P}{\partial y^2}\right) = 12\frac{\mu}{h^3}P_0 h_0\left(\frac{1}{h_0}\frac{d\Delta h}{dt} + \frac{1}{P_0}\frac{\partial \Delta P}{\partial t}\right) \tag{2.35}$$

If $\Delta P/P_o << \Delta h/h_o$, Eq. 2.34 can be developed into:

$$\frac{\partial^2 \Delta P}{\partial x^2} + \frac{\partial^2 \Delta P}{\partial y^2} = 12\frac{\mu}{h^3}\frac{d\Delta h}{dt} \tag{2.36}$$

or

$$\frac{\partial^2 P}{\partial x^2} + \frac{\partial^2 P}{\partial y^2} = 12\frac{\mu}{h^3}\frac{d\Delta h}{dt} \tag{2.37}$$

In Eq. 2.37, P is equivalent to ΔP. Thus, letter P in Eq. 2.37 is sometimes read as ΔP. However, attention must be given to the difference in the boundary conditions for P and ΔP : $P = P_o$ but $\Delta P = 0$ at the periphery of the plate.

Now, as in the case of the GLVs, let us consider a pair of rectangular plates (Fig. 2.7) with length L and width B on top of each other separated by a gap of h. For the plates, the length of the microbeam is much bigger than the width of it, i.e.$L \gg B$. Considering the vertical motion of the top plate, the modified Reynolds equation 2.37 reduces to a one-dimensional problem:

$$\frac{d^2 P}{dx^2} = \frac{12\mu}{h^3}\frac{dh}{dt} \tag{2.38}$$

In this case, the boundary conditions are: $P(\pm\frac{B}{2}) = 0$ and by solving the above equation we obtain:

$$P(x,t) = \frac{-6\mu}{h^3}\left(\frac{B^2}{4} - x^2\right)\frac{dh}{dt} \tag{2.39}$$

The damping pressure is positive when the air film is squeezed, i.e. dh/dt<0 and vice versa. The maximum damping pressure occurs at the center of the plate, where $P(0,t) = \frac{-3\mu B^2}{2h^3}\frac{dh}{dt}$. The damping force F on the plate is then given by:

$$F = \int_{-B/2}^{+B/2} P(x)dx = \frac{-\mu B^3 L}{h^3}\frac{dh}{dt} \equiv \frac{-\mu B^3 L}{h^3}\dot{h} \tag{2.40}$$

According to the definition of $F = -c\dot{z}$, the coefficient of damping force for a long rectangular plate is given by:

$$c_d = \frac{\mu B^3 L}{h^3} \tag{2.41}$$

It can be shown that the amplitude-frequency relation is governed by the damping factor [14]:

$$\varsigma = \frac{c_d}{2m\omega_0} \tag{2.42}$$

where, m is the mass of the microbeam and ω_0 is the natural angular vibration frequency of the plate.

Further, it can be explained [4, 7, 13] that the damping ratio ς determines the dynamic behavior of the system where a damped harmonic oscillator can be:

Overdamped ($\varsigma > 1$): The system returns (exponentially decays) to equilibrium without oscillating. The larger the value of the damping ratio ς, the slower the system returns to equilibrium.

Critically damped ($\varsigma = 1$): The system returns to equilibrium as quickly as possible without oscillating.

Underdamped ($0 < \varsigma < 1$): The system oscillates with the amplitude gradually decreasing to zero.

Hence, careful choice of the dimension of the micro-devices can produce the desired damping effect which can be used for dedicated application of the MEMS.

2.6 GEMINI process flow

The general process flow for the poly-SiGe GLVs is schematically shown in Fig. 2.9. This process flow was developed solely in imec (without any contribution from the PhD candidate's side).

(a) A standard Si wafer is used as the starting substrate. A 1 μm thick High Density Plasma (HDP) Si-oxide layer is deposited over the Si-wafer followed by the deposition of a trilayer of Ti (20 nm)/ AlCu (880 nm)/ TiN (60 nm) after a short degas. The metal stack was subsequently patterned to define the underlying metal connections to the bondpads.

(b) A 1650 nm of HDP Si-oxide was added further on top of the existing structures and planarized by CMP. Next, a 200 nm additional HDP Si-oxide was added and the wafers were then annealed at 455° C for 30 mins. Later, a 400 nm of SiC layer was deposited on top of the planar oxide to protect the bottom dielectric layers during the aggressive vapor HF-based release process. This protection layer was subsequently patterned and plasma-etched, stopping on the underlying metal layer to define the opening for the MEMS via.

(c) A trilayer of Ti (5 nm) / TiN (10 nm) / poly-SiGe (380 nm) was deposited at a maximum wafer temperature of 450°. This layer fills the via holes and at the same time creates the electrode layer on top of which a 250 nm Si-oxide hardmask is deposited and patterned.

(d) Further, an extra SiGe layer is deposited to form a thicker electrode. A single etch process was used to pattern both the thin and thick electrode layers by using the oxide hardmask as an etch stop layer. The thick electrode structures are therefore defined by lithography while the Si-oxide hardmask defines the thin electrode structures.

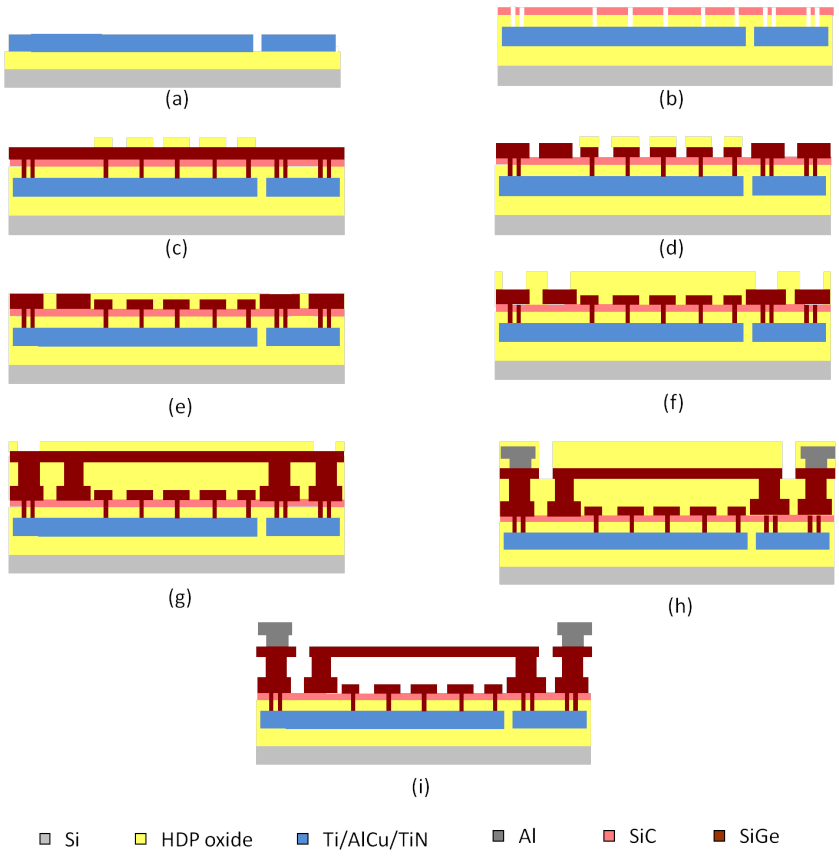

Figure 2.9: Process flow for fabrication of the devices.

(e) Next, the electrode structures were planarized by the deposition of a HDP Si-oxide layer followed by CMP which makes the thick electrode to be ~ 50 nm thicker than the thinner one.

(f) After this planarization with stop on the SiGe layer, the sacrificial HDP oxide layer was added on top of the electrodes to define the actuation airgap for the MEMS structures. Two different thicknesses were used, 350 nm and 800 nm as measured from cross section SEM pictures. In this sacrificial oxide, the anchors for anchoring the structural layer to the electrode are etched.

(g) These anchors are filled during the deposition of the SiGe structural layer. To create the bondpads, a low temperature protecting oxide was deposited on top of the structural layer stack followed by a subsequent patterning to create bondpad openings.

(h) These openings were filled with metals and later patterned to form the

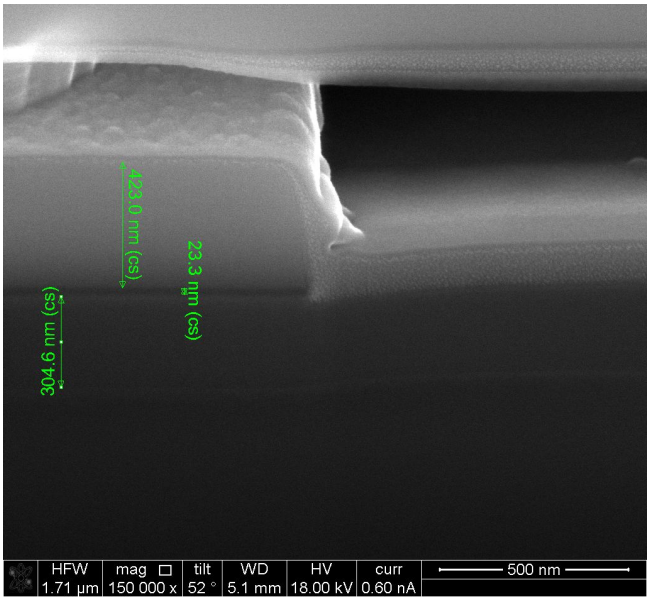

(a)

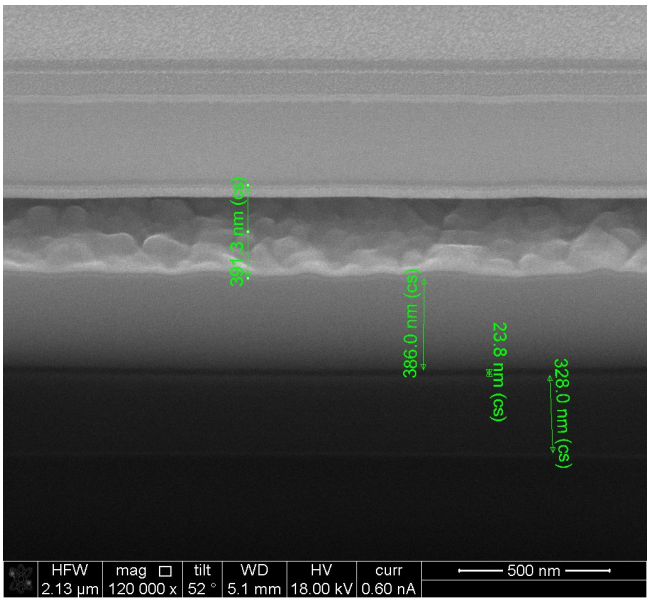

(b)

Figure 2.10: (a) SEM cross section of the device showing the anchor and the thick electrode, (b) SEM cross section of the device showing the thin electrode and the thickness of the airgap.

bondpads. Next, another protecting oxide layer was deposited on top of the bondpads. Further, the poly-SiGe structural layer was patterned to create the fixed-fixed microbeams defining the GLVs.

(i) Finally the samples were released with a 5 step release recipe in a vapor of HF and ethanol. By breaking the release process in several steps, the water formed as by-product could be efficiently removed which decreases the chance of stiction of the structural layer.

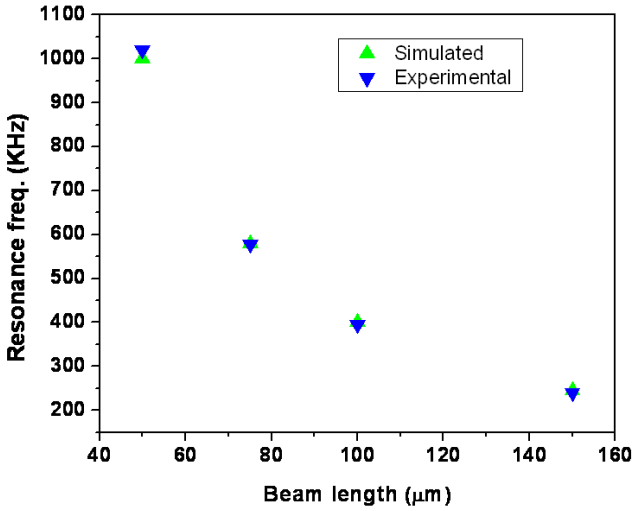

Figure 2.11: Experimental and simulated resonance frequency of the fixed-fixed beams with different lengths.

The structural layer is a B-doped poly-SiGe layer with a thickness of 330 nm (or 380 nm) which is deposited by chemical vapor deposition (CVD) at a wafer temperature of 450° C on top of a Ti (5 nm) / TiN (10 nm) adhesion layer. The precursor gasses are SiH_4, GeH_4 and B_2H_6. The SiH_4:GeH_4 ratio equals 0.9:1 and a B_2H_6 (1% in H2) flow of 90 sccm was used at a wafer temperature of 450° C resulting in an expected Ge concentration of 78% [15]. The total processing time at 450° C was 12.5 minutes for a 330 nm thick layer and 14.2 minutes for a 380 nm thick layer. Next, a CMP step was used on the SiGe structural layer for roughness reduction. This CMP step also reduces the thickness of the structural layer down to 300 nm (350 nm). Then a barrier layer of 5 nm thick SiC and a 30 nm thick Al layer were further added on top of the structural poly-SiGe layer to increase the reflectivity of the structures.

The strain gradient in cantilever beams was measured to be 7x10^{-4}/μm,

which makes this process also suitable for processing micro-mirrors. Due to difficulties in performing stress measurements on the thin SiGe samples, the resonance frequency of fixed-fixed beams with different lengths were measured and then fitted to find the Young's Modulus (E) and the tensile stress (σ) in the SiGe structural layer. As can be seen from the Fig. 2.11, E = 120 GPa and σ = 20 MPa result in a perfect fit. The maximum resonance frequency that was achieved in our structures is 1MHz which corresponds to the shortest microbeam of 50 μm.

2.7 Optical Interferometry

Optical interferometry has been widely used in accurate measurements of distances, displacements and vibrations, tests of optical systems, measurements of gas flows and plasmas, temperature, pressure, electrical and magnetic fields, rotation sensing, microscopy, and high resolution spectroscopy [16]. Because of its high precision and non-contact nature, it has long been acknowledged as a reliable profiling technique for measuring surfaces when stylus profiling cannot be used due to the risk of damage.

>From the basic principle of interferometry we all know that, if two coherent beams of intensities I_1 and I_2 overlap, then the resulting intensity can be expressed as:

$$I_{tot} = I_1 + I_2 + 2\sqrt{I_1 I_2}cos(\frac{2\pi}{\lambda}(p_1 - p_2)) \tag{2.43}$$

Where p_1 and p_2 are the path lengths traversed by the respective beams.

If the two waves are derived from a common source, we have: $\Delta\varphi = \frac{2\pi}{\lambda}(p_1 - p_2)$

That is, the phase difference is linearly related to the optical path difference (OPD). Thus the resultant sinusoidally varying intensity will form alternating bright and dark fringes if being observed from across the propagation direction.

In order to obtain sustained and distinguishable interference patterns, a few constraints should be fulfilled [17]:

i) The phase difference from the two vibrating sources must remain constant (they must remain coherent).

ii) The waves must have the same frequency and wavelength and nearly equal amplitudes.

iii) The wave sources must be of a single wavelength or nearly monochromatic.

iv) The wave fronts of the interfering waves must be traveling in the same direction or make only a very small angle with each other.

v) The two interfering waves must possess the same polarization state.

Optical interferometers can be used to measure distances in terms of the wavelength of light. Most of the interferometers used for this purpose are two-

beam interferometers, using amplitude division. In the Michelson interferometer, a beam-splitter is used to create interfering beams from a single light source and recombine them to form interfering fringes. The properties of the fringe pattern are determined by the known wavelength of the source and the OPD introduced by the modifiable relative positions of two reflecting mirrors for the two interfering beams. This scheme has been preserved and adapted to most of the modern interferometers. The fringes are observed by a light detector that can collect the intensity information, which will be sent to a photo-electronic fringe counting device to derive the OPD. Charge-Coupled Detector (CCD) arrays are usually used as the detector because of the capability of simultaneous measurements over a large array of points.

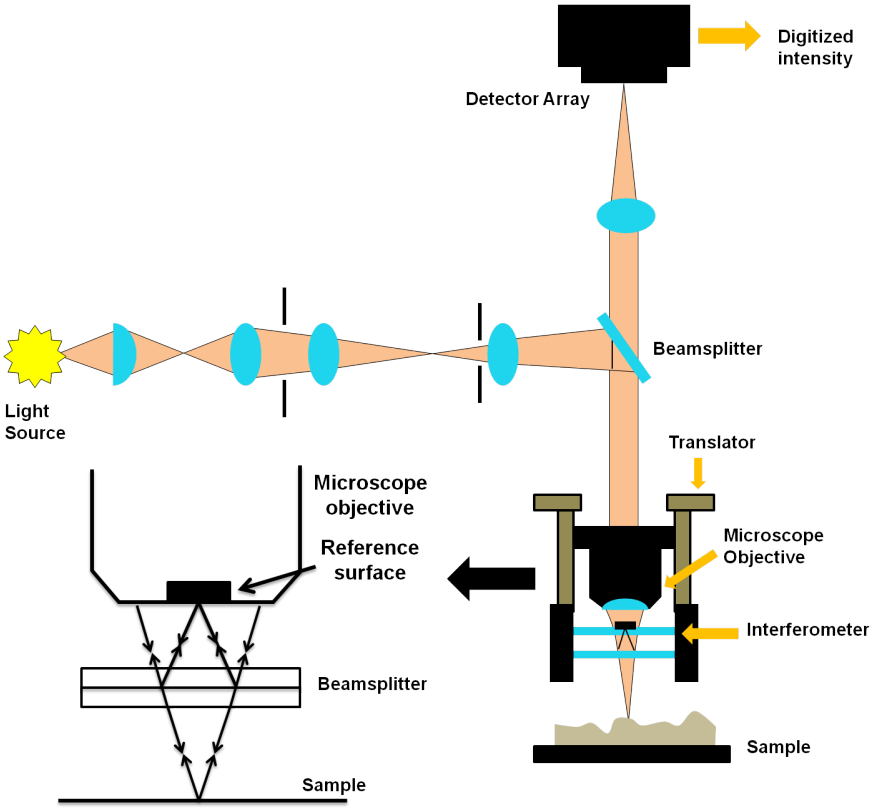

Figure 2.12: Distribution of the optical components inside a WYKO optical profilometer showing its operational principle.

2.7.1 WYKO Optical Profiler

Using a narrowband (near monochromatic) light source and trying to follow the continuous fringe shapes, Phase Shifting Interferometry (PSI) [1] is usually used to test smooth surfaces (roughness less than 30nm). Sub-nanometer resolution can be achieved in vertical measurements. However, PSI is incapable of obtaining a correct profile for objects with large step changes in height. It becomes ineffective as the height discontinuities of adjacent pixels approach $\lambda/4$, in which case maxima will occur at multiple positions in the resultant fringe pattern due to the near-monochromatic source, causing ambiguity.

A better solution is to use a broadband source (white light) with Vertical Scanning Interferometer (VSI). With a white-light source, a separate fringe system is produced for each wavelength, and the resultant intensity at any point in the observation plane is the sum of all the individual patterns. If an interferometer is adjusted so that the OPD is zero at the center of the field, when all the fringe systems from different wavelengths superimpose to each other, the maximum intensity with the best contrast is obtained only at this center point. Moving away from the center, because the coherence length of the source is short and the spacing of the fringes varies with the wavelength, the contrast decreases rapidly to zero at distances greater than the coherence length of the source, thus eliminating the height ambiguity in PSI. In other words, a sample point is in focus only when the maximum fringe contrast is obtained. In this kind of white light interferometery (VSI mode), th e height variations across the sample are determined by locating the focus points from the maximum fringe contrast. Each CCD pixel effectively acts as an individual interferometer and thus leads to a very accurate map of the surface.

The major disadvantage of VSI is that only a single height is measured at a time. This usually requires multiple scans for any surface larger than the FOV of the profiler, which would be time-consuming. White light interferometry gives a vertical resolution ~ 3nm, whereas it can measure rough surfaces with vertical range of ~ 135 nm to 10 mm.

The Michelson and other traditional amplitude division interferometers suffer from a vibration problem due to the long beam paths. To overcome this problem, the Mirau interferometer introduces a compact setup as shown in Fig. 2.12. In this scheme, source light is incident through the microscope objective on a beam splitter. The transmitted beam goes to the test surface, while the reflected beam goes to the reference mirror placed at the focal plane of the objective. Using the VSI mode, the sample is scanned along the vertical axis by a computer controlled piezoelectric pusher. The test beam is recombined with the reference beam at the same beam splitter and returned through the objec-

[1] taking successive interferograms at slightly shifted mirror positions

tive to the CCD detector. Both beams share a common path over most of their length, so the system is much less sensitive to vibrations. The demodulation is performed through post-processing involving Fourier analysis.

2.7.2 Laser Doppler Vibrometer

A laser Doppler vibrometer (LDV) [18, 19] is the scientific instrument that we employed to make the non-contact vibration measurement of our microstructures. The laser beam from the LDV is directed at the surface of interest and the vibration amplitude and frequency are extracted from the Doppler shift of the laser beam frequency due to motion of the microstructures. The output of an LDV is generally a continuous analog voltage that is directly proportional to the target velocity component along the direction of motion of the laser beam.

2.7.2.1 The Doppler effect

When a wave is reflected from a moving object and is detected by a measurement system, then the measured frequency shift of the wave can be described as [20]:

$$f_D = \frac{2 * v(t) * cos(\alpha)}{\lambda} \tag{2.44}$$

Where λ is the wavelength of the wave, v(t) is the object velocity as a function of time and α is the angle between the laser beam and the velocity vector. To be able to determine the velocity of the object, the (Doppler-) frequency shift has to be measured at a known wavelength. This is done in the LDV by using a laser interferometer as described in section 2.6.

2.7.2.2 Experimental set-up

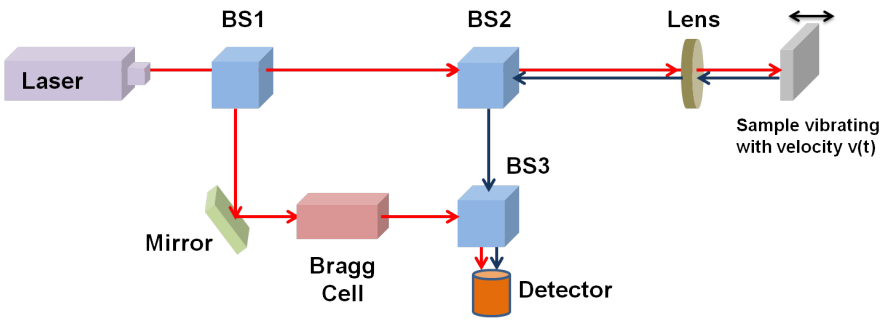

Figure 2.13: A simplified experimental set-up and working principle of a Laser Doppler Vibrometer.

A simplified experimental arrangement for an LDV system is shown in Fig. 2.13. A He-Ne laser beam is split by the beamsplitter BS1 into a reference beam and a measurement beam. After passing through a second beamsplitter BS2, the measurement beam is focused onto the surface under investigation which further reflects it back. The reflected beam is now deflected downwards by BS2 and merged with the reference beam by the third beamsplitter BS3 and is then directed towards the detector. Since, the path length of the reference beam remains constant over time (p2 = const.), a movement of the object surface under investigation (p1 = p1(t)) generates a dark and bright fringe pattern typical of interferometry on the detector.

Change in the optical path length per unit of time manifests itself as the frequency shift of the measurement beam. This means that the modulation frequency of the interferometer pattern determined is directly proportional to the velocity of the object. Since, the object movement away or towards the interferometer results in the same frequency shift, the optical set-up alone cannot determine the direction of motion of the object. Hence, an acousto-optic modulator (Bragg cell) [21] is placed in the reference beam, which shifts the light frequency by 40 MHz (by comparison the frequency of the laser light is 4.74 * 10^{14} Hz). This generates a modulation frequency of the fringe pattern of 40 MHz when the object is at rest. If the object then moves away from the interferometer then the modulation frequency is increased and if it moves towards the interferometer then the detector receives a frequency lower than 40 MHz. In this way, the vibrometer can not only de cipher the amplitude of the movement but also the direction of movement of the object.

2.8 Summary

In this chapter we introduced the theory behind the deformation of the microbeams which we will use in the following chapters to describe the electromechanical properties of the MEMS structures. We saw how the presence of residual stress in the fixed-fixed beams can influence its static and dynamic properties. We learned about the importance of the squeezed film damping phenomenon in the microstructures and in the following chapters we will see how it can be optimized to use the damping in our favor. We already got the details regarding the elastic properties of the poly-SiGe material which was used in imec to fabricate the MEMS devices. We also introduced the two standard measurement techniques to investigate the static and dynamic behavior of the MEMS devices.

References

[1] N. Lobontiu and E. Garcia, *Mechanics of microelectromechanical systems*. Springer, 2005.

[2] M. Do Carmo and M. Do Carmo, *Differential geometry of curves and surfaces*. Prentice-Hall Englewood Cliffs, NJ, 1976, vol. 2.

[3] H. Goldstein, *Classical mechanics*. Addison-Wesley, 1980.

[4] S. Senturia, *Microsystem design*. Springer Netherlands, 2001.

[5] W. Young and R. Budynas, *Roark's formulas for stress and strain*. McGraw-Hill, New York, 2002.

[6] A. Boresi, R. Schmidt, and O. Sidebottom, *Advanced mechanics of materials*. Wiley, 1993, vol. 5.

[7] G. Rebeiz, *RF MEMS: theory, design, and technology*. LibreDigital, 2003.

[8] J. Gere and S. Timoshenko, "Mechanics of materials, pws pub," *Co., Boston*, 1997.

[9] M. Zahn, *Electromagnetic Field Theory: a problem solving approach*. RF Krieger, 1987.

[10] H. Tilmans, M. Elwenspoek, and J. Fluitman, "Micro resonant force gauges," *Sensors and Actuators A: Physical*, vol. 30, no. 1, pp. 35–53, 1992.

[11] L. Landau and E. Lifshitz, *Fluid Mechanics*. Pergamon, 1987.

[12] K. Symon, *Mechanics*. Addison Wesley, 1971.

[13] M. Bao, *Analysis and design principles of MEMS devices*. Elsevier Science, 2005.

[14] M. Bao and H. Yang, "Squeeze film air damping in MEMS," *Sensors and Actuators A: Physical*, vol. 136, no. 1, pp. 3–27, 2007.

[15] G. Bryce, S. Severi, B. Du Bois, M. Willegems, G. Claes, R. Van Hoof, L. Haspeslagh, S. Decoutere, and A. Witvrouw, "Simultaneous optimization of the material properties, uniformity and deposition rate of polycrystalline cvd and pecvd silicon-germanium layers for mems applications." ECS, 2008.

[16] P. Hariharan, *Basics of interferometry*. Academic Press, 2007.

[17] J. Morgan and R. Hanau, "Introduction to geometrical and physical optics," *American Journal of Physics*, vol. 21, p. 696, 1953.

[18] P. Castellini, G. Revel, and E. Tomasini, "Laser doppler vibrometry," *An introduction to optoelectronic sensors*, vol. 7, p. 216, 2008.

[19] P. Castellini, M. Martarelli, and E. Tomasini, "Laser doppler vibrometry: Development of advanced solutions answering to technology's needs," *Mechanical Systems and Signal Processing*, vol. 20, no. 6, pp. 1265–1285, 2006.

[20] J. Rosen and L. Gothard, *Encyclopedia of Physical Science*, 2009, vol. 1.

[21] S. Chuang *et al.*, *Physics of optoelectronic devices*. Wiley New York, 1995.

3
Grating Light Valves

The Grating Light Valve (GLV) is a microelectromechanical reflection grating [1–4]. It consists of clamped-clamped beams suspended in air over a conducting substrate with the help of anchors on the two far ends allowing them to move vertically. The microbeams are held in tension so that when non-actuated they remain flat and behave like a mirror giving specular reflection in the 0th order and the pixel is in the OFF state, with no light diffracted to the ±1st order (dark state). After actuation, the alternate movable beams are deflected downwards, which turns the pixel ON and hence a quasi-continuous phase function can be imprinted onto the incoming light beam (bright state). The result is an entirely reconfigurable diffractive element in reflection mode providing precise and accurate pixel-by-pixel brightness control.

3.1 GLV concept and modeling

Fig. 3.1(a) shows the top view of the GLV device showing the series of 50 μm long microbeams which are anchored on the two end sides. If we consider the side view of the free-standing microbeams (the dotted region), then it looks like Fig. 3.1(b)(1) which acts like a specular reflector. Now if the alternative microbeams are vertically displaced due to electrical actuation then the device enters into a diffractive state. With increasing vertical displacement the amount of diffracted light starts dominating the reflected amount. At a deflection of $\lambda/4$, the amount

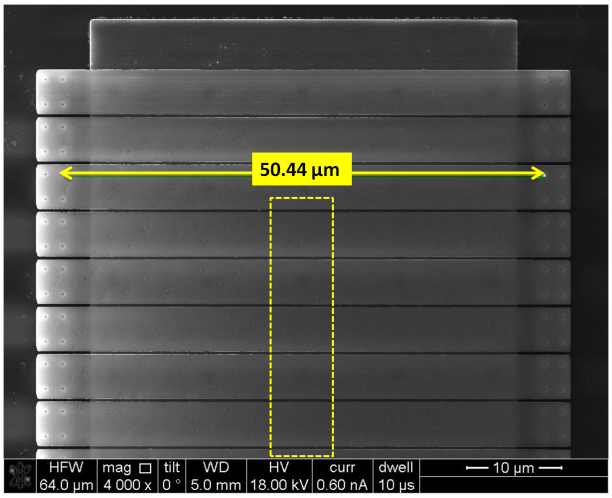

(a)

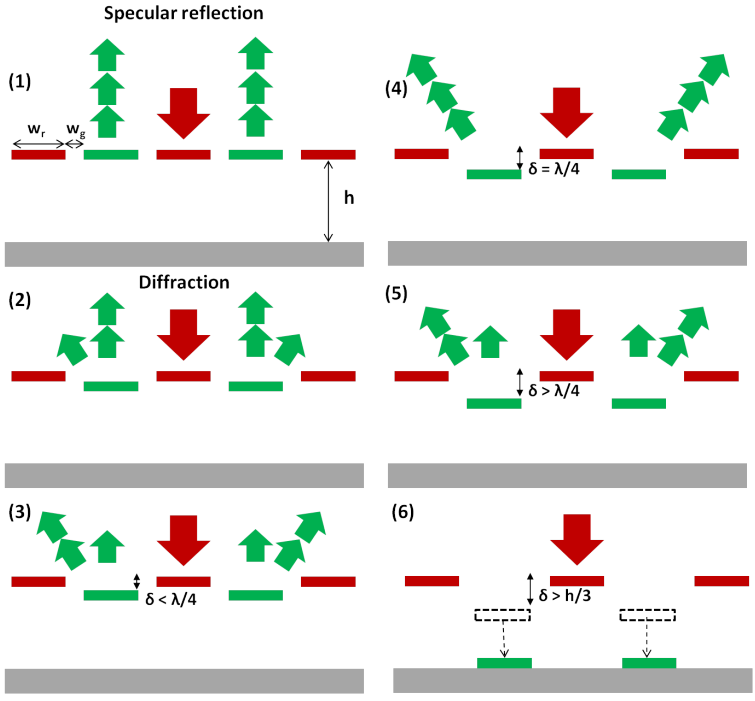

(b)

Figure 3.1: (a) The SEM picture of the top view of the GLV devices, (b) The different states of operation of a GLV device. The picture shows how the device transforms itself from a reflective OFF state (non actuated) to a diffractive ON state (actuated) and how the beam deformation influences the device characteristics further.

of light reflected from the stationary and deformed microbeam remains the same but they are exactly opposite in phase ($\frac{2\pi}{\lambda} \cdot 2 \cdot \frac{\lambda}{4} = \pi$). Hence, after a $\lambda/4$ vertical displacement, the specular reflection is minimal and the light diffracted to the $\pm$1st order reaches its maximum. For, any deflection between 0 and $\lambda/4$, the returning light from the grating is a mixture of reflected and diffracted light. By controlling the exact position of the microbeams and thereby the path length difference, we have an analog control over how much light is reflected and how much light is diffracted. Of course this requires that we have a structure and an actuation mechanism that allows continuous positioning of the microbeams.

3.1.1 Binary diffraction grating

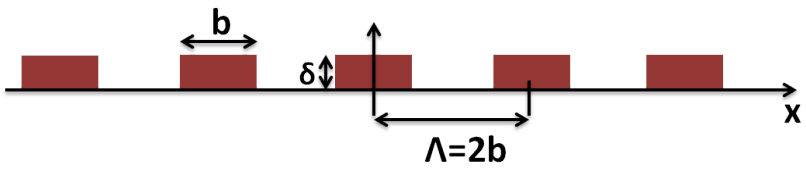

Figure 3.2: Binary grating with a period equal to twice the width of the rectangular steps.

If we consider a reflection type square wave phase grating [5, 6] consisting of rectangular sections as shown in Fig. 3.2, then the mathematical description of the unit cell is two offset rectangular functions with a phase constant applied to the second one.

$$f(x) \equiv \left[rect(\frac{x}{b}) \otimes \delta(x) \right] + \left[rect(\frac{x}{b}) \otimes \delta(x-b) \right] e^{i\phi} \tag{3.1}$$

the offset is accomplished with the delta function and the phase difference, $\phi = \frac{2\pi}{\lambda} * 2\delta$ is introduced by δ, the height of the rectangular section. Having defined the unit cell, the infinite grating can be represented with one additional convolution:

$$grating = f(x) \otimes comb(x/\Lambda) \tag{3.2}$$

Because the grating is a periodic structure, light propagation away from the surface will resolve itself into discrete diffraction orders whose angles of propagation θ_m are given by the grating equation:

$$\Lambda sin(\theta_m) = m\lambda \tag{3.3}$$

The discrete diffraction orders propagate at discrete angles of θ_m. Therefore, the Fourier transform of the grating is defined at discrete intervals corresponding to the transform of $comb(x/\Lambda)$, a function with unit value at $q = m/\Lambda = m/2b$, where m is an integer. The Fourier transform of the unit cell, forms an envelope function that defines the amplitude and relative phase of each diffracted order. The Fourier transform of the rect(x) function is sin(q)/q or sinc(q), so for the unit cell we get:

$$F\left(q\right) = \frac{1}{2}\frac{sin(\pi bq)}{\pi bq}exp(i2\pi qb/2) + \frac{1}{2}exp\left(i\phi\right)\frac{sin(\pi bq)}{\pi bq}exp(-i2\pi qb/2) \quad (3.4)$$

In the case of the ideal binary phase grating, where $\phi = \pi$, it simplifies to:

$$F(q) = \frac{1}{2} \times \frac{sin(\pi bq)}{\pi bq}[exp(i\pi qb) - exp(-i\pi qb)] \quad (3.5)$$

For the case of a square wave grating with b=$\Lambda/2$ and evaluating for the discrete diffraction orders where the comb function is non-zero, the output of the grating is defined as:

$$F(q)|_{q=\frac{m}{\Lambda}} = \frac{sin(m\pi/2)}{m\pi/2}[isin\,(m\pi/2)] \quad (3.6)$$

Which equals zero for all even values of m. For odd values of m, the diffraction efficiency from the grating is given by:

$$\eta_m = p_m^2 \equiv |F\left(\frac{m}{\Lambda}\right)|^2 = \left(\frac{2}{m\pi}\right)^2 \quad (3.7)$$

As evident, the diffraction efficiency is zero for all even values of m, whereas the maximum power is steered towards the 1st order with a maximum efficiency of 81%.

Given the high fill factor ($\mu = \frac{w_r}{w_r + w_g}$) of the GLVs, they can be approximated as a binary diffraction grating with changing phase due to controlled displacement of the alternate microbeams.

Considering 92% reflectivity of the top Al layer with 94% fill factor for our GLVs, the maximum attainable intensity together in both the 1st order turns out to be ~ 71%.

3.1.2 Simulation of the optical properties of the GLVs

The method of rigorous coupled wave analysis (RCWA) [7, 8] using the software CAMFR was used to simulate the optical properties of the Al coated GLVs. Fig. 3.3 shows the variation in diffraction efficiency of different orders with the fill factor of the GLVs. It clearly indicates the total diffraction efficiency in the 1st

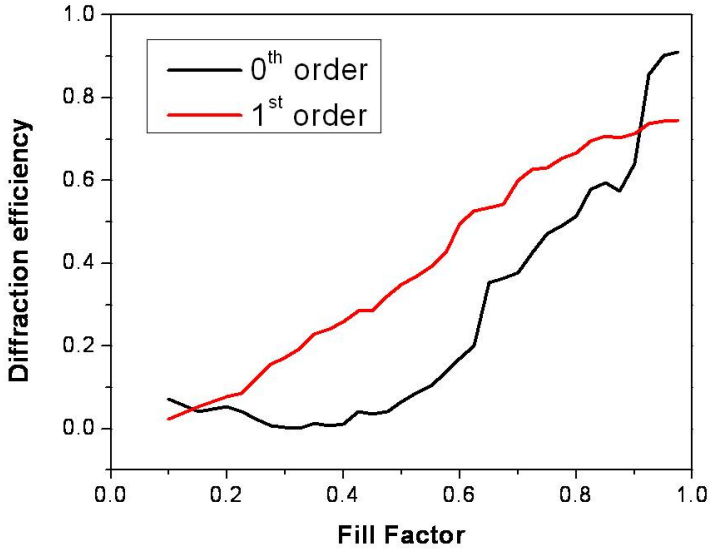

Figure 3.3: Variation of the 0th and 1st order diffraction efficiency of the GLVs with fill factor.

order (after a deflection of $\lambda/4$ of the alternate microbeams) is always higher than that of the 0th order (at non-deflected state of the microbeams) for $\mu < 0.91$. The situation reverses after $\mu > 0.91$. It also shows that the maximum diffraction efficiency achievable in the 1st order ranges between 70%-74%.

3.1.3 Modeling the electro-mechanical properties of the GLVs

In this section, we present the COMSOL simulations of the electromechanical properties of the GLV microbeams. In our simulation each microbeam is of 5 μm wide and 300 nm thick, made of poly-SiGe and coated with 30 nm of Al on top, both to increase the reflectivity and to act like a conductor. These are modeled as thin beams resting on anchors on both the ends with an airgap of 600 nm and we simulated their electrostatic displacement towards the substrate. The microbeams are under tensile stress which helps them to remain flat in their non-actuated state. Precise control of the vertical displacement can be achieved by balancing the electrostatic attraction against the restoring force of the microbeams.

Fig. 3.4 shows the trade-off between the resonance frequency and the pull-in voltage as a function of the length of the beams and tensile stress in it as found from the COMSOL Multiphysics simulations. The ultimate goal of GEMINI is to integrate the MOEMS with CMOS, hence the amplitude of actuation voltage is

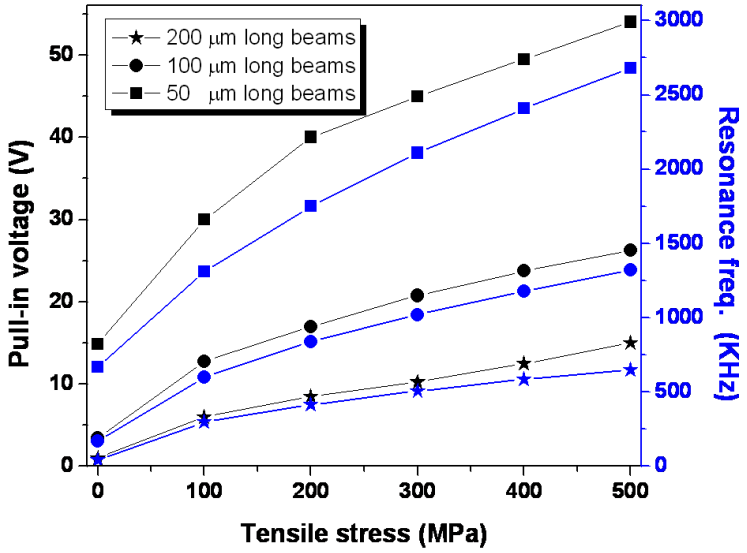

Figure 3.4: Trade off between the pull-in voltage and resonance frequency of the GLVs.

of utmost importance to us. As can be observed from the figure, an increase in resonance frequency comes at the expense of an increase in the operating voltage of the device. Hence, though a high tensile stress increases the speed of the device, it results in the operating voltage to go out of the range of the CMOS integrated circuit.

We used COMSOL Multiphysics (Finite Element Analysis), to model the static displacement of the GLV microbeams. Fig. 3.5 shows the deflection of a 50μm long microbeam under electrostatic attraction. It can be observed that the deflection of the alternate beams does not exactly resemble a square well grating structure. As seen from Fig. 3.6 the maximum deflection is only at the very center of the microbeams. For a 50μm long structure, the maximum deflection is concentrated only within 10μm at the center. In case the width of the focused spot finally incident on the GLV device is larger than 10μm, light reflected from different parts of the actuated beam is not exactly in the same phase and hence the efficiency of the device will deteriorate. This implies, shorter beams increase the speed of the device manifold but also needs tighter focussing to achieve the full optical functionality of the GLVs.

To maximize the efficiency of the diffracted light and to decrease the dark state noise within the system, we tried an alternative flexure structure instead of fixed-fixed continuous beams as shown in Fig. 3.7. Here a heavy central mass

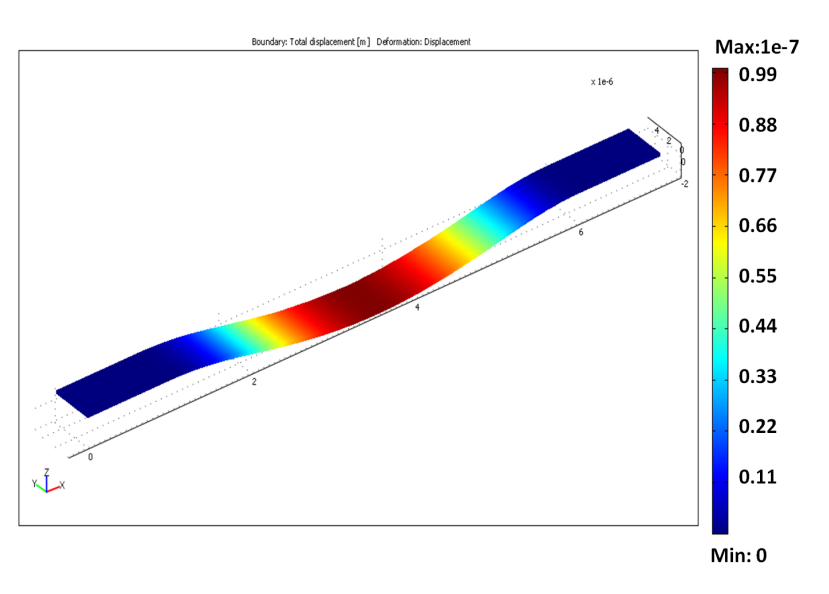

Figure 3.5: Electric field induced deformed shape of a fixed-fixed microbeam.

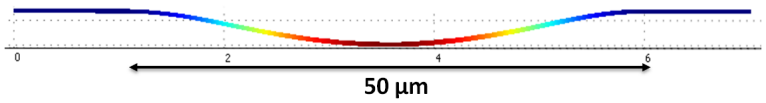

Figure 3.6: Side view of a deformed fixed-fixed beam showing a distinct difference from a square-well shape.

is suspended with the help of four strings fixed on anchors on both sides. During electrostatic actuation, the strings bend to create the deflection, though the central heavy mass nearly remains flat. In our device, the flexure consists of 20 μm long central portion suspended with the help of 15 μm long individual strings on both sides (the total length remains 50 μm). A clear difference in deflection of a fixed-fixed continuous beam and a flexure beam is shown in Fig. 3.8. As predicted earlier, the total length of the central flat portion of the flexure structure ($\sim 20\mu$m) is nearly double that of a fixed-fixed continuous beam. As a result, more light will be diffracted with the same phase which enhances the efficiency of the device.

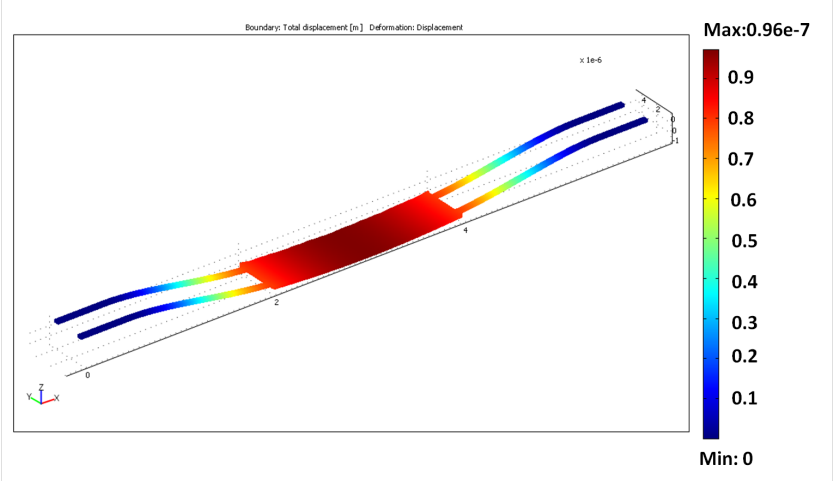

Figure 3.7: Deflection profile of a flexural microbeam with a central heavy mass supported at the two far ends by thin strings. As evident from the picture the central heavy mass remains significantly flatter after actuation of the structure compared to the simple microbeam of fig. 3.5.

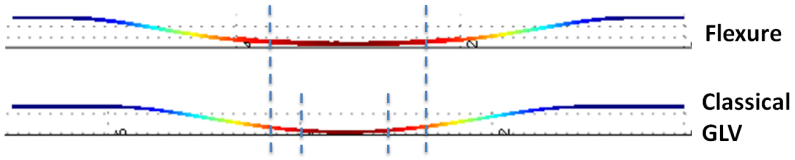

Figure 3.8: Comparison of the deflection profile of a fixed-fixed beam and a flexure beam of the same total length of 50 μm.

3.2 Static characterizations

3.2.1 Optical profilometry

One of the stringent requirements for a GLV to function well is to achieve minimal height difference among the consecutive microbeams which will scatter the incident light. This scattered light also adds up intensity in the direction of the 1st order diffraction without any actuation of the microbeams and as a result deteriorates the dark state. Hence, in Fig. 3.9(a), we show the profile of a 100 μm long non-actuated GLV device. Using an optical profilometer, we can measure a minimal height difference of 2.6 nm among the consecutive microbeams which indicates an excellent planarity of the fabricated devices. We further performed optical profiling of the devices in the actuated state to determine the

maximum displacement that can be obtained just before pull-in. Fig. 3.9(a) shows the result for a 100 μm long GLV device in two steps of voltages. As seen from Fig. 3.9(b) that after 129 nm of displacement of the microbeams at 5.3 V, the devices go straight to pull-in with the next step of 5.4 V indicating the max deflection obtainable is ~130 nm for these devices (for 400 nm airgap between the microbeams and the substrate).

3.2.2 Optical characterization set-up

As shown in Fig. 3.3, optical system can be constructed to collect either the 0th order or the 1st order diffracted light. The latter has definite advantages over the the 0th order. The non-diffracting portions of the device (surrounding region of the microbeams) remain equally reflecting for both the ON and OFF states. Hence, it becomes difficult to separate the modulated light (reflected of the center of the beam) from the stray light reflected from elsewhere. As a result, a good contrast value can't be reached.

The optical setup we used to characterize the DC performance of the device is shown in Fig. 3.10. The source we used was a 405 nm diode laser. The laser light is collimated and magnified using two bi-convex lenses and passes through a beamsplitter before facing the cylindrical lens which converges the light in a single direction to make a linear field along the center of the microbeams. The light diffracted from the gratings is separated from the incoming light with the help of the beamsplitter. A slit was used in between the collimating lens and the beamsplitter to change the length of the field incident on the device. It makes sure that the focused spot is contained only within the series of the microbeams and the amount of stray light generated from elsewhere of the device is minimal. Finally a detector is used to measure the intensity of the individual diffracted orders.

We thoroughly modeled our optical setup using the ray tracing software Advanced Systems Analysis Program (ASAP). To optimize the optical performance of the GLVs, one of the most challenging tasks is tighter focusing, i.e. to reduce the width of the line spot as far as possible. As the final focusing of the collimated light is done by the cylindrical lens, this only determines the final width of the focused spot on the microbeams.

We modeled all the optical components using ASAP (the shape, the dimensions and the coatings on it). We considered a collimated source generating 50×50 rays along the X and Y directions and the simulation was confined to a total of 2×10^6 generated rays within the optical system. The distance among the different objects was varied to minimize the stray light reaching the detector because of internal reflections among the different components. It ensures us that the achieved contrast is not limited by the used setup. First, the simula-

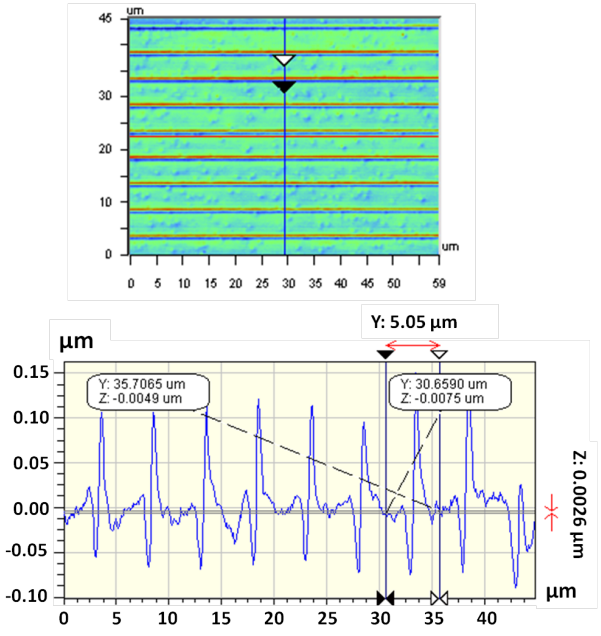

(a)

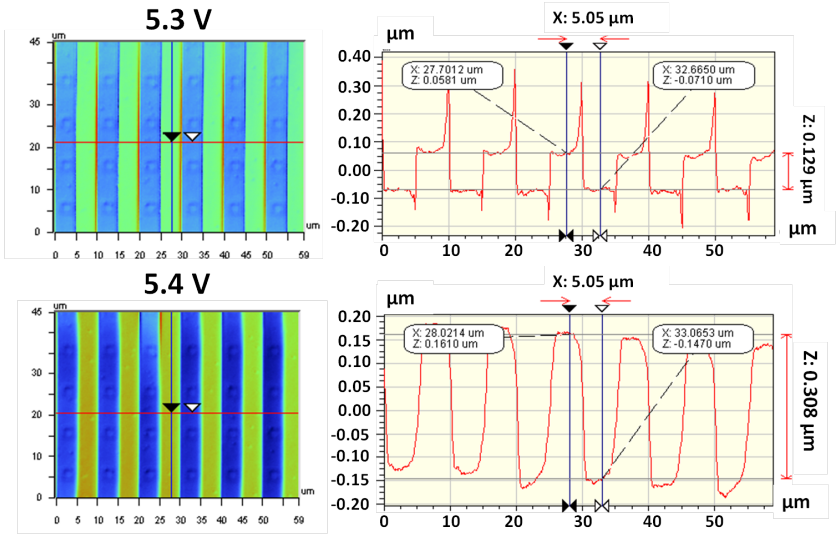

(b)

Figure 3.9: (a)Optical profile of a non-actuated GLV device as obtained from WYKO, (b) Optical profile of an actuated GLV device showing the pull-in phenomenon and hence the highest possible vertical displacement of the microbeams.

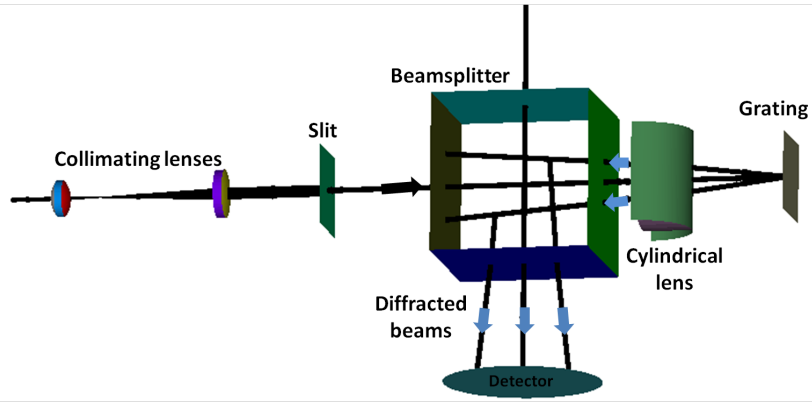

Figure 3.10: Schematic of the optical set-up as used in ASAP to study the stray light density influencing the contrast measurement.

	1st lens position (cm)	2nd lens position (cm)	Slit position (cm)	Beamsplitter Position (cm)	Cylindrical lens position (cm)	Detector distance from beamsplitter (cm)	Flux at detector without grating	Flux at detector with grating	Relative contrast
(1)	0	3	13	15.5	19.5	16.5	0.11e-8	0.84e-4	7.6*10^4
(2)	0	3	23	26.5	30.25	16.5	0.24e-9	0.84e-4	3.5*10^5
(3)	0	3	23	26.5	30.25	10	0.24e-9	0.84e-4	3.5*10^5

Figure 3.11: Influence of the different distances among the optical components on the amount of stray light reaching the detector and hence influencing the contrast measurement.

tion was performed considering a perfectly reflecting mirror at the focal plane of the lens to know the amount of stray light reaching the detector because of internal reflections and due to aberration of the lens. Then, maintaining the same distances an ideal grating (70% efficiency in the ±1st order) was placed in the focal plane to calculate the diffracted light along with the stray light finally reaching the detector. Hence we were able to calculate the maximum contrast that can be achieved with this experimental setup in case of an ideal grating. Table 3.11 shows the variation in the flux with the change in the distance among the different components and how it affects the contrast of the system. It gives us an estimation that if no stray light is generated by the GLV device, the maximum achievable contrast in the ±1st order is still limited to $\sim 10^5$ because of the optical components used within the characterization set-up.

Fig. 3.12(a) shows the experimental set-up used for characterization of the GLVs. A photodiode in series with a slit is used to measure the intensity of the individual diffracted orders as a function of amplitude of the applied actuation

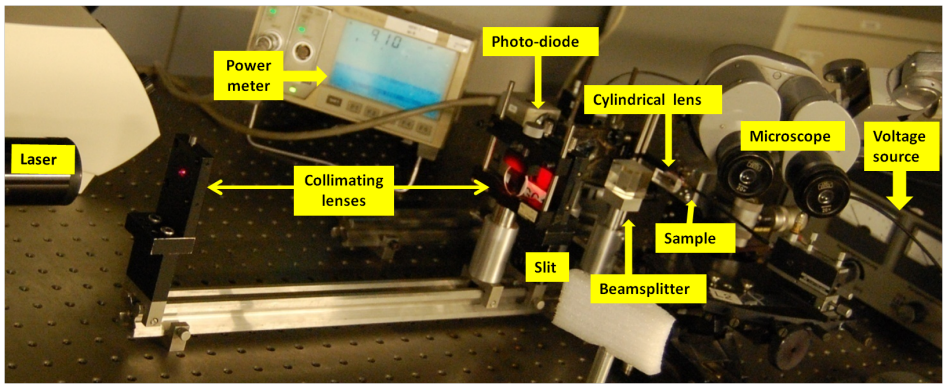

(a)

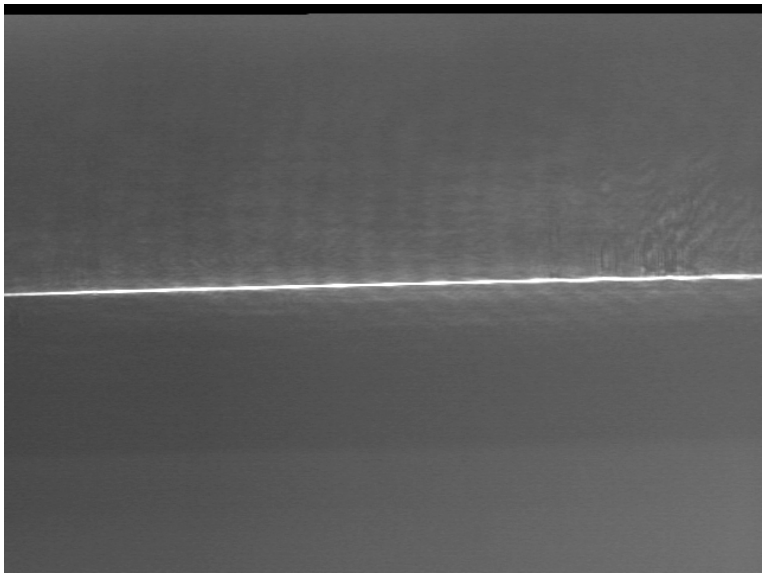

(b)

Figure 3.12: (a) Experimental set-up as used for characterization of the GLVs, (b) Line spot as generated by a cylindrical lens that was focused on top of the GLVs, measured using a CCD camera.

voltage. We could obtain a minimum line-width of 19.5 μm for the focused spot (Fig. 3.12(b)) using this set-up. The length of the line can be changed by changing the opening of the front slit.

3.2.3 Optical characterization

As discussed earlier, the beams are curved from the anchors onwards with maximum deflection occurring only at the center. The longer the microbeam, the flatter is the deformed shape. A comparison of the deformed shape (as obtained from a COMSOL Multiphysics simulation) of the fixed-fixed microbeams, the flexure structure and the experimentally obtained Gaussian intensity distribution of the focused spot is shown in Fig. 3.13(a). As can be observed, the variation in height of the central deformed region of a 75 μm long microbeam is much smaller than that of the 50 μm long microbeam. Moreover, a 50 μm long flexure beam with a heavy central mass has a comparable central deflection as that of a 75 μm long fixed-fixed beam.

We used the full 1D array of the successive 100 microbeams to measure the contrast and efficiency of the whole device using this set-up. Fig. 3.13(b) shows the analog optical behavior of the GLVs with 400 nm airgap. We used a 405 nm violet laser to characterize the optical response of the GLVs and to estimate the maximum contrast achievable for the devices. A clear increase in the +1st order diffracted intensity can be observed with increasing external DC bias. When the displacement of the microbeams exceed h= $\lambda/4$, the diffraction efficiency decreases again. At the same time, as described in Fig. 3.13, due to flatter deformation of the longer microbeams and the flexure structures compared to the shorter microbeams, higher diffraction efficiency and hence higher contrast is obtained for 75 μm long GLVs than that of the 50 μm long ones (section 3.1.3). For our GLVs, the maximum power diffracted in the first order was measured to be 67% (combining +1st and -1st orders) which follows the theoretical prediction very closely. A maximum contrast of ~ 1713:1 was obtained reproducibly showing the usefulness of our GLVs in making high quality displays.

3.3 Dynamic characterization

3.3.1 Effect of squeezed film damping in GLVs

As discussed before, squeezed film damping [9–11] plays an important role in the dynamic response of the devices. To take advantage of the relatively high resonance frequency, the damping in these devices should also be high enough to suppress oscillations [12]. We used laser doppler vibrometry to characterize the response of the GLVs to a square wave pulse train and varied different

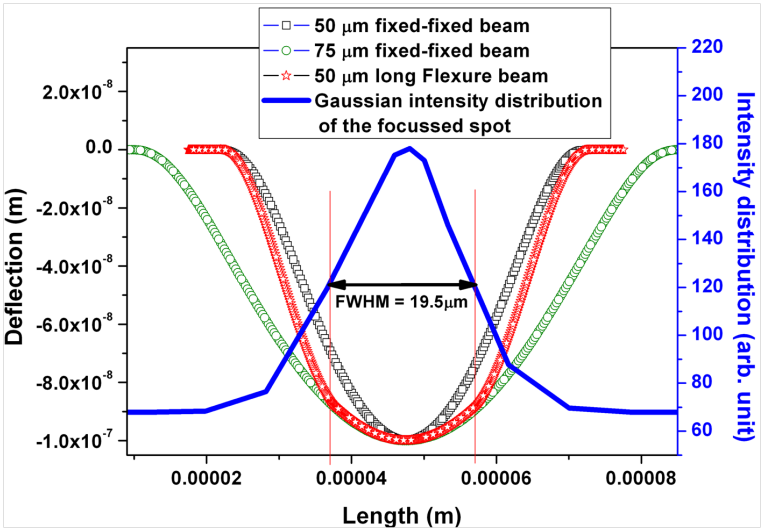

(a)

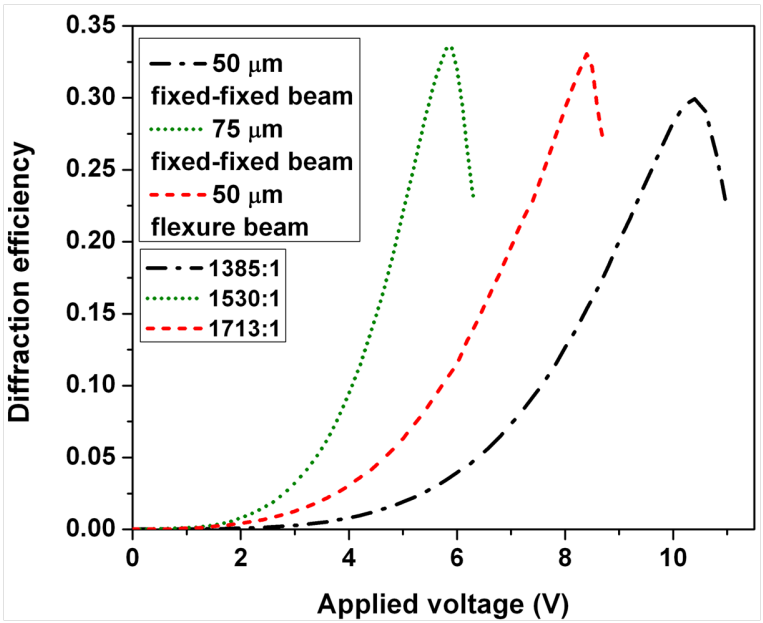

(b)

Figure 3.13: (a) Comparison of the deflection of the microbeams and the Gaussian intensity distribution of the focused spot at the center of the devices, (b) Analog response of GLV devices showing an excellent optical response.

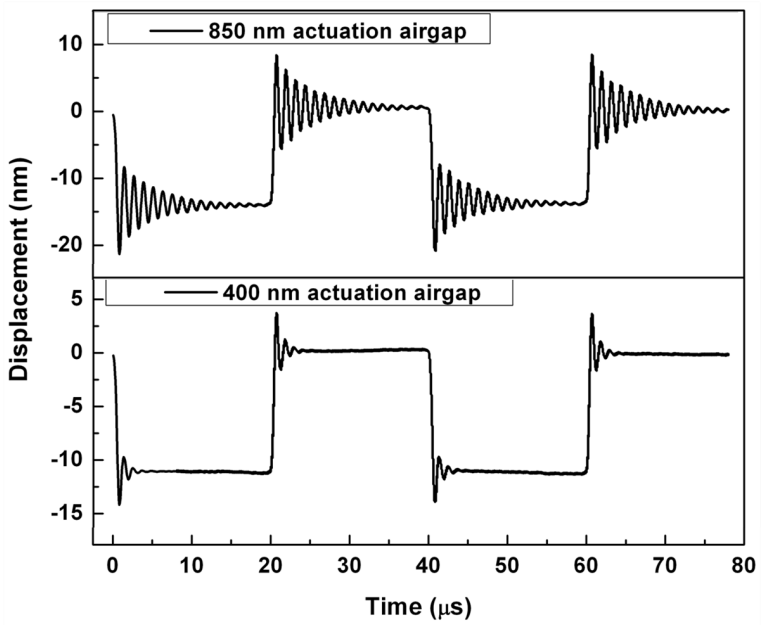

(a)

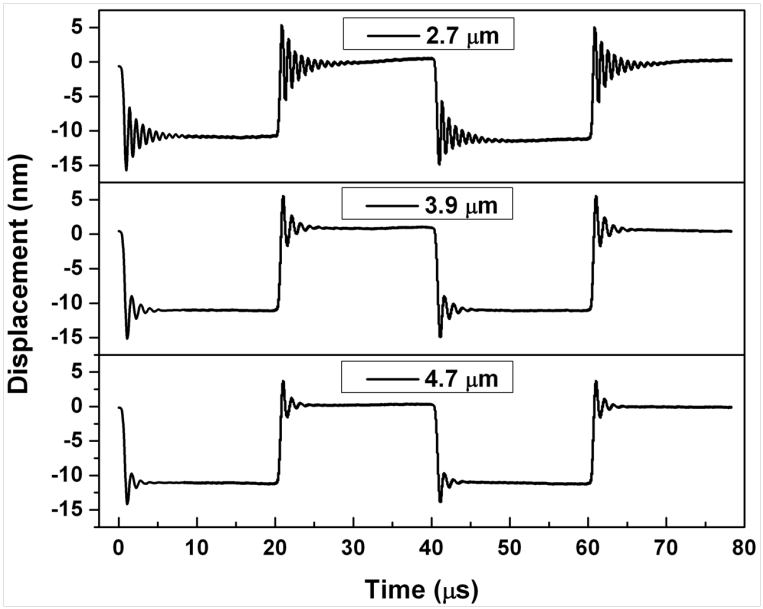

(b)

Figure 3.14: Variation in settling time of the devices with change in (a) underlying airgap and (b) width of the microbeams.

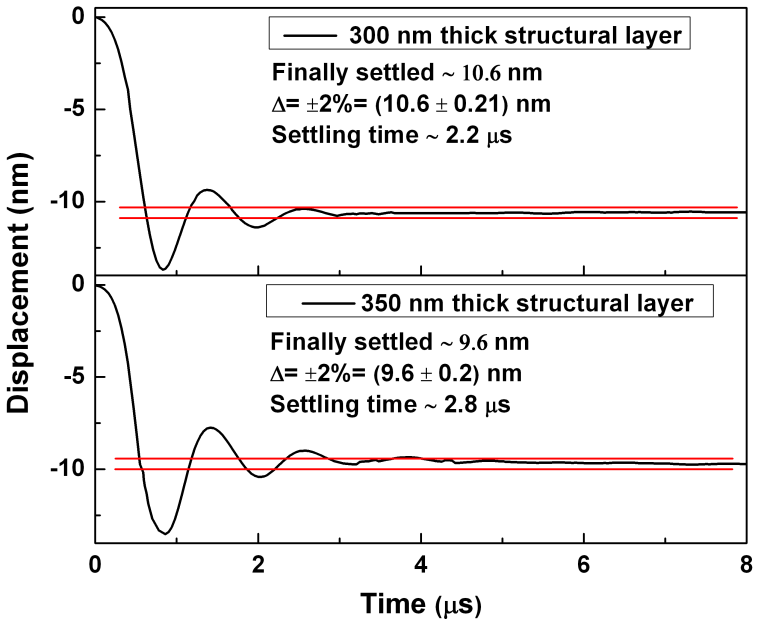

(a)

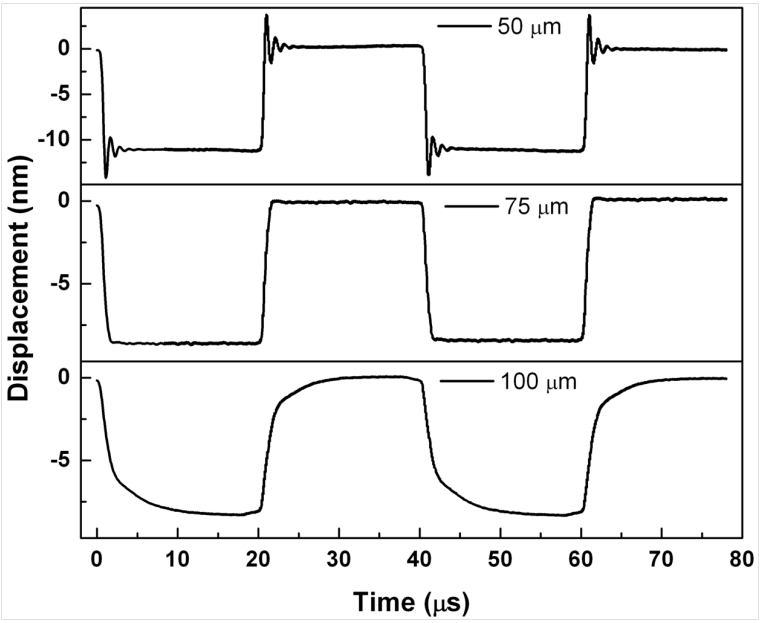

(b)

Figure 3.15: Variation in settling time of the devices with change in (a) layer thickness and (b) length of the microbeams.

dimensional parameters to determine their influence on the dynamics of the devices.

As seen from Eq. 2.41, the most important parameter influencing the damping of the devices is the airgap ($c_d \propto \frac{1}{h_0^3}$). Fig. 3.14(a) shows the dependence of the settling time (equilibrium ± 2%) of the microbeams on the underlying airgap thickness. Whereas the settling time was ~ 20 μs for a microbeam with 850 nm airgap, it reduced to 2.2 μs by changing the airgap to 400nm. With decreasing airgap, the underlying fluid is more efficiently trapped during displacement of the microbeams, damping the overshoots more effectively resulting in faster settling. Since the GLV beams are electrostatically actuated, their dynamic operation is inherently limited by the pull-in phenomenon (maximum deflection = $\frac{h_0}{3}$). Hence to obtain the maximum diffraction efficiency, the sacrificial layer thickness should be designed in such a manner that $\frac{h_0}{3} > \lambda/4$. As a result, the airgap is constrained by the wavelength of operation. Later in this chapter, we show an approach which we used to avoid destruction of the devices due to pull-in. In that case the airgap can be made closer to its minimum permissible value of $3\lambda/4$.

Fig. 3.14(b) shows the variation in settling time of the devices with change in width for a 50 μm long microbeam with an airgap of 400 nm. As can be seen clearly from the figure, with increasing width the mechanical oscillations and overshoots are more efficiently damped resulting in a faster settling of the devices. Whereas the settling time was ~ 6.5 μs for a 2.7 μm wide microbeam, it reduced to 2.2 μs by increasing the beam width to 4.7 μm. But the beam width is also related to the angular separation among different diffracted orders as shown in equation 3.3. Hence, for a larger width, the effective separation and collection of the 0th and the ± 1st orders of diffracted light become more difficult, resulting in either a reduced contrast or a more extended optical setup.

Variation in settling time of the devices with the thicknesses of the microbeams is shown in Fig. 3.15(a). The two microbeams differ only by their thickness and we actuated both of them in the same way. As can be seen from the figure, for the thicker microbeam, the amplitude of the overshoot and ringing is larger than that of the thinner one. Hence, faster settling is obtained for the thinner microbeam. But with lower thickness the resonance frequency also scales down. Hence a minimum thickness of the beam has to be chosen to achieve a resonance frequency suitable for the targeted application. Any additional thickness beyond the minimum value will degrade the settling time.

Fig. 3.15(b) shows the dependence of the settling time on the length of the microbeams. Whereas a 4.7 μm wide and 50 μm long beam with 400 nm airgap shows an under-damped nature with a settling time of ~2.2 μs, longer beams of 75 μm and 100 μm lengths with identical parameters become critically damped and over-damped with settling times of ~ 2 μs and ~ 11 μs respectively. It sug-

gests that with increasing length, the damping ratio increases and accordingly the nature of damping in the system is changed as predicted from Eq. 2.41. It is clear from fig. 3.4 that though longer beams help in faster settling, it decreases the resonance frequency and hence the modulation rate of the devices. On the other hand, shortening the length of the beams increases the actuation voltage and also requires critical optical settings to obtain a narrower focused spot at the center of the beams. Hence a judicial choice of the length of the beams has to be made depending on the target application of the devices.

Fig. 3.16 shows the relation among the above mentioned parameters with the final performance of the GLVs. As clear from the table that all the parameters are inter-related with other system level requirements. It shows that optimization of a single parameter cannot improve the total performance of the whole system and hence an overall optimization is necessary. Additionally, as evident from the above mentioned experimental results, with the relatively low resonance frequency of our microbeams, controlling the damping time becomes extremely important in obtaining high switching speed of our GLV devices.

DEVICE	LENGTH (l) ↑	WIDTH (w) ↑	THICKNESS (t) ↑	SACRIFICAL LAYER HEIGHT (h) ↑	TENSILE STRESS (σ) ↑
DATA RATE	Resonant frequency ↓ Damping time ↓	Damping time ↓	Resonant frequency ↑ Damping time ↑	Damping time ↑	Resonant frequency ↑
OPERATING VOLTAGE	Drive voltage ↓		Drive voltage ↑	Drive voltage ↑	Drive voltage ↑
WAVELENGTH		Angular resolution among diffracted orders ↓		Pull-in distance ↑	

Figure 3.16: Relation among different device parameters to optimize the system level performance of GLVs.

3.3.2 Effect of external impedance on settling time

Circuit impedance plays an important role in switching speed of the devices. Fig. 3.17(a) shows the equivalent circuit of a fixed-fixed beam, where R_S is the circuit impedance, C is the GLV capacitance. The GLV device has a capacitance value of only a few femtofarads. Usually the system RC time constant is deter-

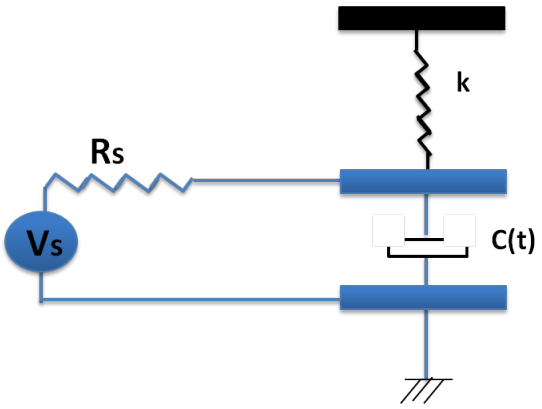

(a)

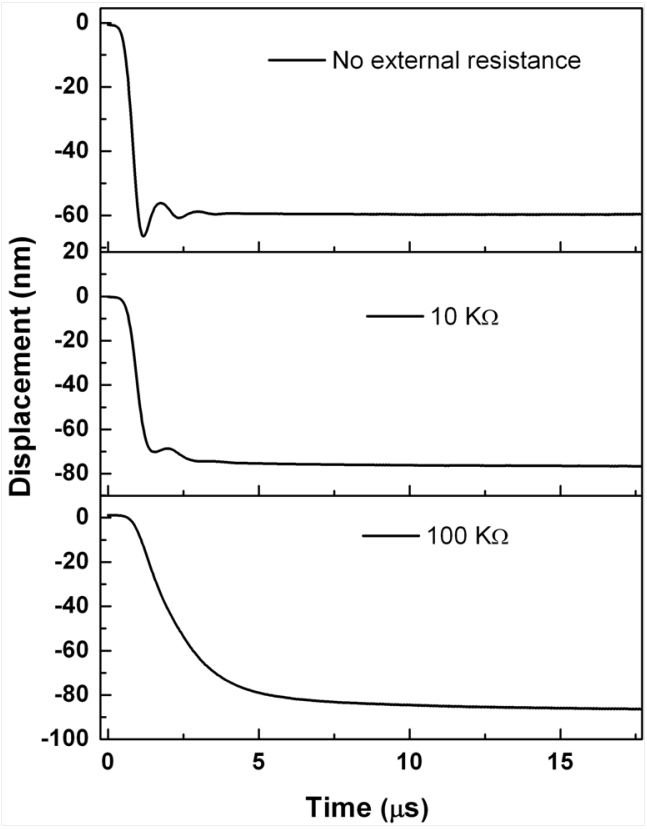

(b)

Figure 3.17: (a) A equivalent RC circuit of a GLV device, (b) Variation in settling time of a GLV devices with change in external impedance.

mined by the driver impedance, interconnect resistance and parasitic capacitance. The time constant of the circuit determines the amount of energy transferred to the microbeams. If the kinetic motion of the beams is not damped properly then it generates oscillations and overshoots. Fast rising edges have high frequency components that can excite ribbons at their resonant frequency; slow rising edges have less high-frequency energy and are less efficient at exciting those oscillations. Thus, adding an external resistance lowers the slew rate which reduces the ringing amplitude. However, if the electrical slew rate is too low, it starts dominating the dynamic response time of the system and the full capability of the GLV device is lost.

Fig. 3.17(b) shows the variation in settling time of the device with increasing impedance. Mechanical oscillations and overshoots are more efficiently damped with higher impedance though the transition time degrades.

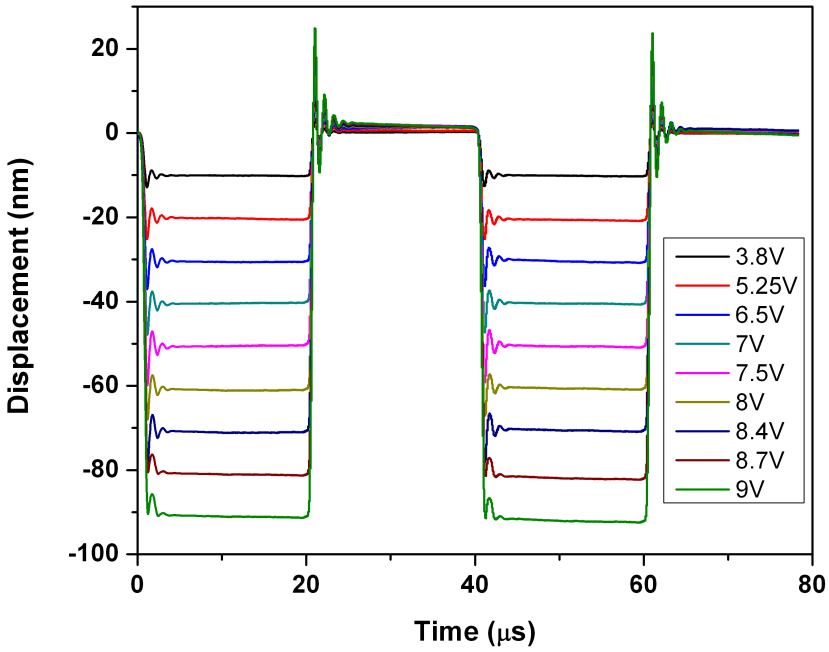

Figure 3.18: Response of a GLV to a square wave pulse train showing the inherent analog nature of the device.

3.3.3 Analog gray scale of GLVs

One of the most important advantages of GLVs over other optical MEMS is its intrinsic analog capability of producing gray scales as shown in Fig. 3.18.

Other digital modulators use pulse width modulation (PWM) [13] to achieve gray scales which directly erodes the data throughput of the devices. But GLVs, instead of using PWM to achieve gray scales, can be actuated to reach a defined displacement corresponding to a certain intensity level making these devices perfectly suitable for high speed applications. By increasing the resolution of the driving voltage, the GLVs can be easily programmed to different intensity levels extending the bit depth of the system. 8 bit or 10 bit grayscale GLVs [14] have already been reported and a bit depth as high as 16 bit has been proposed for use in a display application [15].

3.3.4 Mechanical stoppers as a pull-in protection mechanism

As discussed before, one of the stringent constraints behind the operation of GLVs, is avoiding the accidental pull-in of the microbeams when $\frac{h_0}{3} \sim \lambda/4$. Since the GLV microbeams are always at a higher potential compared to the bottom electrode (grounded), snapping down of the microbeams due to pull-in gives rise to a short circuit, potentially damaging the device. Hence, to avoid the short circuit, we did a thicker SiGe electrode deposition (within the airgap portion) which is electrically isolated from the rest of the bottom electrode and connected to the same metal line as of the microbeams through vias. Therefore, the electrostatic force acting on the fixed-fixed microbeam is still present because the larger area thin electrode does not interact with the equipotential bumps. The cross-section schematic and the relevant dimensions are shown in fig. 3.19(a). Once the pull-in occurs, the microbeams fall on the thicker equipotential bumps instead of the grounded electrode avoiding the short circuit. Given the small contact area between the GLV beams and the bumps, the problem of stiction after pull-in is avoided. Fig. 3.19(b) demonstrates the successful implementation of our pull-in protection mechanism. We used a 100 μm long GLV microbeam having a pull-in voltage (V_P) of 5.5 V. As observed from the figure, for a triangular pulse pattern of maximum ±6.5 V, the beam snaps down once V_P is exceeded. After snapping on the thicker bumps, no further displacement is measured and hence a flat response is obtained. Soon after the triangular pulse strength reduces again below V_P, the movement of the microbeam is resumed and the displacements can be traced back again. No failure for the device was observed over several periods of operation which proves the usefulness of the stopper mechanism.

3.4 Conclusion

We showed the successful implementation of poly-SiGe as a MEMS material in fabricating GLVs. The devices showed an excellent behavior both for the static

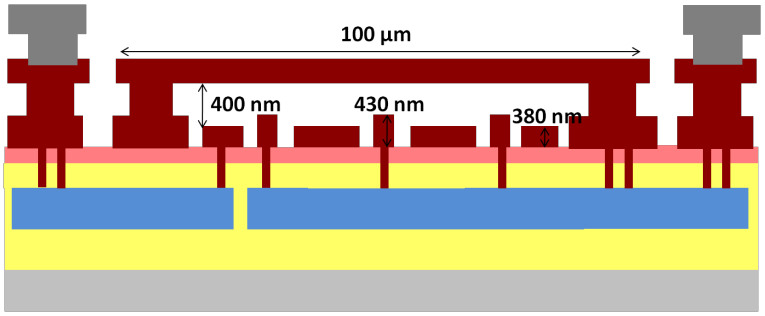

(a)

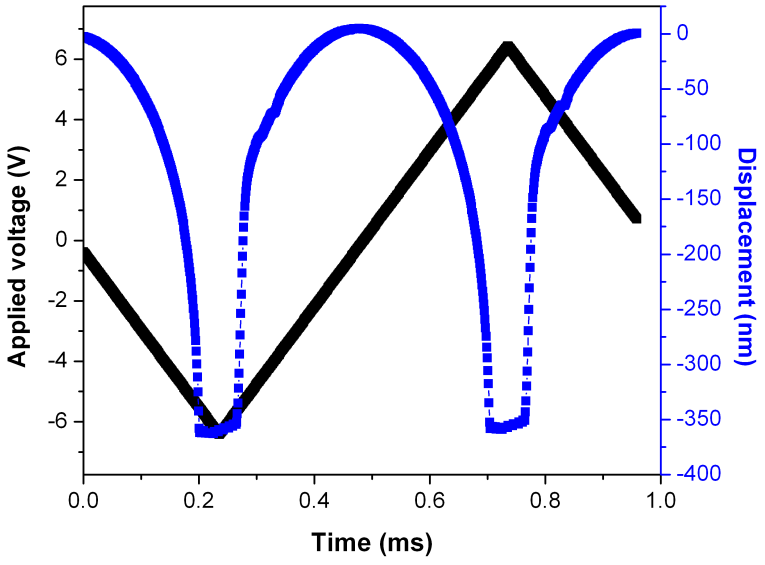

(b)

Figure 3.19: (a) Design details of the distribution of the equipotential thicker bumps and grounded thinner electrodes defining the pull-in protection mechanism, (b) Displacement of a pull-in protected GLV device in response to a triangular pulse pattern.

and dynamic responses. A contrast of more than 1500:1 was obtained with high diffraction efficiency. Since we operated with relatively short GLVs, the maximum diffracted light intensity was found to be strongly dependent on the length of the microbeams. The settling time of the devices was mainly dominated by the resonance frequency and the damping factor. Different dimensional parameters were varied to find their influence on the damping and hence the settling of the devices following a step function excitation. A minimum settling time of 2.2 μs and 2 μs were obtained for the 50 μm and 75 μm long devices showing under-damped and critically damped behavior respectively. We discussed how other system related trade-offs have to be managed once the dimensional parameters are varied to obtain faster switching. We proposed the use of mechanical stoppers [16] to save the devices from erroneous deterioration due to pull-in [17]. Overall these results prove the usefulness of the thin poly-SiGe MEMS technology for fabricating MOEMS devices directly on top of CMOS.

References

[1] D. Bloom *et al.*, "The grating light valve: revolutionizing display technology," in *Proc. SPIE*, vol. 3013, 1997, pp. 165–171.

[2] D. Amm and R. Corrigan, "Grating Light Valve Technology: Update and Novel Applications," in *SID Symposium Digest of Technical Papers*, vol. 29, no. 1, 1998, p. 29.

[3] J. Trisnadi, C. Carlisle, and R. Monteverde, "Overview and applications of Grating Light ValveTM based optical write engines for high-speed digital imaging," in *Proc. SPIE*, vol. 5348, 2004, pp. 1–13.

[4] D. Amm and R. Corrigan, "Optical performance of the grating light valve technology," 1999, pp. 1–8.

[5] D. C. O'Shea, *Diffractive optics: design, fabrication, and test.* Society of Photo Optical, 2004, vol. 62.

[6] J. Goodman, *Introduction to Fourier optics.* Roberts & Company Publishers, 2005.

[7] M. Moharam and T. Gaylord, "Rigorous coupled-wave analysis of planar-grating diffraction," *JOSA*, vol. 71, no. 7, pp. 811–818, 1981.

[8] S. Peng and G. M. Morris, "Efficient implementation of rigorous coupled-wave analysis for surface-relief gratings," *JOSA A*, vol. 12, no. 5, pp. 1087–1096, 1995.

[9] M. Bao, *Analysis and design principles of MEMS devices*. Elsevier Science, 2005.

[10] M. Bao and H. Yang, "Squeeze film air damping in MEMS," *Sensors and Actuators A: Physical*, vol. 136, no. 1, pp. 3–27, 2007.

[11] C. Gudeman, B. Staker, and M. Daneman, "Squeeze film damping of doubly supported ribbons in noble gas atmospheres," in *Technical Digest Solid-State Sensor and Actuator Workshop*, 1998, pp. 288–291.

[12] G. Rebeiz, *RF MEMS: theory, design, and technology*. LibreDigital, 2003.

[13] V. Markandey, T. Clatanoff, R. Gove, and K. Ohara, "Motion adaptive deinterlacer for dmd (digital micromirror device) based digital television," *Consumer Electronics, IEEE Transactions on*, vol. 40, no. 3, pp. 735–742, 1994.

[14] E. Tamaki, Y. Hashimoto, and O. Leung, "Computer-to-plate printing using the grating light valve device," in *Proc. SPIE*, vol. 5348, 2004, pp. 89–97.

[15] B. Winkler, D. Elkins, A. Tanner, D. Bloom, R. Yeh, V. Ramsey, and R. Cuff, "An optical microsystem for displays," in *Technical Digest of the 2006 Solid State Sensors, Actuators and Microsystems Workshop*, 2006, pp. 15–18.

[16] S. Beeby, G. Ensell, M. Kraft, and N. White, "Mems mechanical sensors. artech house," *Inc. Boston, London*, pp. 104–105, 2004.

[17] D. Peroulis, S. Pacheco, K. Sarabandi, and L. Katehi, "Electromechanical considerations in developing low-voltage RF MEMS switches," *Microwave Theory and Techniques, IEEE Transactions on*, vol. 51, no. 1, pp. 259–270, 2003.

4

Variable optical attenuator

In our earlier chapter we looked the GLVs as purely one-dimensional gratings in the sense that the optical interaction between the incident light and the grating was considered to be confined to a plane, in which the grating is periodic in one dimension and uniform in the other. In reality, of course the gratings are three-dimensional objects. Hence, a complete model of the optical interaction with the gratings has to include the grating depth which is ranging over the length of the beam, leading to shadowing and the fact that the gratings are of finite length which leads to diffraction effects from the termination of the microbeams. In practice for most applications, these effects are not significant enough to influence the proper operation of the movable gratings.

Polarization dependence, on the other hand, is an issue that is important for many practical implementations of the grating modulators. Because of the increasing miniaturization with MEMS technology, the polarization dependence worsens further with scaling down of the device dimensions. For the gratings, both vertical and lateral dimensions can be accurately controlled. Vertical precision is of course necessary for phase control, whereas the lateral accuracy allows us to create very narrow microbeams. As for any integrated circuit devices, the tendency is to shrink the device dimension to the minimum permissible value that can support the desired device functionality. This means, for the one dimensional grating modulators, the targeted period is not much larger than the wavelength. However, this is exactly the length scale at which periodic struc-

tures suffer from strong polarization dependence.

For many applications, polarization dependency is simple to deal with. For example, in a laser-based imaging system, the input polarization to the modulators can be held constant so that any polarization sensitivity is immaterial. Unfortunately, there are applications for which this approach will not work. Notably in fiber optics, the polarization state of the incident light is randomized by temperature dependence and time-varying birefringence of the fiber. For fiber optic applications of these gratings, it is therefore necessary to modify the grating modulator to remove or reduce its polarization sensitivity.

4.1 Introduction

Integrated variable optical attenuators (VOAs) have been widely used for actively controlling the optical power level in wavelength-division multiplexing (WDM) networks [1]. The widespread deployment of WDM networks demands VOAs with compact, robust designs with low power consumption and low wavelength dependent loss (WDL) [2]. Moreover, these VOAs should be able to dynamically regulate the WDM channel power irrespective of the incident light polarization. Additionally, in dense wavelength division multiplexing (DWDM) systems [3], it has become common to control the output of Distributed Feedback Laser Diodes (DFB-LD) with a VOA instead of the input current. Hence, with increasing number of wavelengths multiplexed in these networks, large arrays of VOAs preferably integrated on a single silicon chip will be needed for future DWDM applications. In addition, although the VOAs are now mostly used in telecommunication applications, there are other fields where VOAs are extremely useful. E.g. the membranes used in the absorbance based optodes which are susceptible to degradation due to excessive optical power can be protected using a VOA structure [4]. Also, with increasing popularity of Visible Light communications (VLC), use of VOAs in the visible wavelength is becoming more and more popular [5].

Basically two different families of VOAs have been presented so far, namely those based on micro-optoelectromechanical systems (MOEMS) and those based on photonic lightwave circuits (PLC). Typically, MOEMS based VOAs offer physical features such as tunability, scalability, low electrical power consumption and small form factor [6]. Additionally, as the MEMS technologies use a semiconductor-like lithographic batch fabrication process, the micro-optomechanical components can be monolithically integrated (if the technologies used are thermally and material-wise compatible) with the control electronics on the same chip [7]. This not only improves the performance, yield and reliability but also lowers the manufacturing, packaging and instrumentation costs [8].

Out of the several different MOEMS based VOA designs proposed over the years, interference type VOAs are one of the most primitive but also most popular ones. The interference type VOA uses multi-beam interference to adjust the attenuation level. The first such design was the MARS modulator [9], in which a SiN membrane of $\lambda/4$ optical thickness was suspended over a silicon substrate with a fixed $3\lambda/4$ spacing between the membrane and the substrate. When reflections from the top surfaces of the membrane and substrate are in phase, the incident light is totally reflected. But when the membrane is electrostatically lowered to an airgap of $\lambda/2$, it becomes an antireflection coating with strongly reduced reflectivity. Though the achieved attenuation level was 31 dB with < 3 μs of response time, the reported insertion loss was ~ 3 dB and the device had a relatively high actuation voltage of 35.2 V.

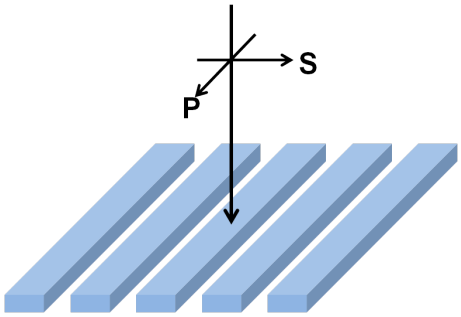

Figure 4.1: Schematic of the incidence of a polarized light on a 1D grating structure.

Alternatively, GLV devices have also been used as the heart of many useful products for optical communications, such as variable optical attenuators, channel power equalization devices, and arrays of 1xN switches. But, as discussed earlier, since these gratings are actually a 1D array of very closely spaced suspended microbeams with subwavelength airgap and metallic coating, the specular reflection is a strong function of the state of polarization of the incident light [10]. The cause of polarization sensitivity in these one dimensional gratings is their rectilinear geometry. The microbeams of the GLV interact differently with light depending on whether the incident electric field is parallel or perpendicular to the length of the microbeams (Fig. 4.1). This points the way to the solution of the polarization dependency problem. It is caused by geometry and hence the geometry has to be changed to make the gratings insensitive to the incident polarization.

In this chapter we report an alternative design which can be used effectively in solving the polarization dependence of the grating based VOAs. Our device consists of a poly-SiGe based 2D MEMS grating built from an anchored mem-

brane with symmetrically distributed square shaped perforations which are filled with fixed islands. Because of the planar symmetry of the design (Fig.4.2), any preferential reflectivity of the different polarization states is effectively eliminated. Also, because of the relatively large dimension of these membranes, the actuation voltage is sufficiently low, leading to minimal power consumption. The design was altered in such a manner that the moving membrane exhibits the optimal damping condition leading to a minimal switching time. Furthermore, poly-SiGe being the structural material, it enables the possibility of large arrays of VOAs to be individually connected to the interfacing circuits.

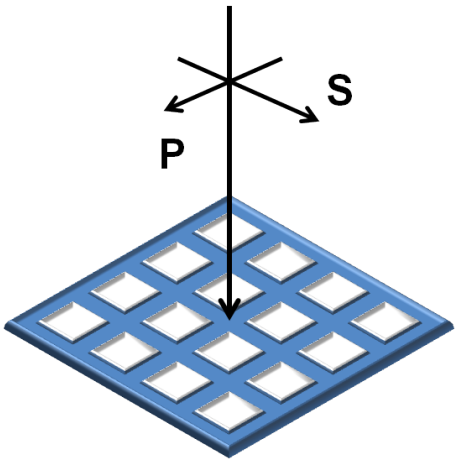

Figure 4.2: Schematic of the incidence of a polarized light on a 2D grating structure.

4.2 Device concept

The proposed structure is presented in Fig. 4.3(a). It consists of a suspended (anchored on four different sides) square shaped membrane which is perforated symmetrically in both in-plane orthogonal directions. Within these perforations, fixed blocks are created (Fig. 4.3(b)) which are supported by anchors of the same height as those supporting the membrane as shown in the cross sectional view in Fig. 4.4. The design was made in such a manner that the area of the movable part and fixed parts are nearly the same. The membrane is held in tension so that it remains flat and forms a reflective surface in the non-actuated state (OFF state) giving specular reflection in the 0th order. When actuated, the membrane is deflected vertically resulting into an entirely reconfigurable 2D diffractive element (ON state) producing increased diffraction in the higher or-

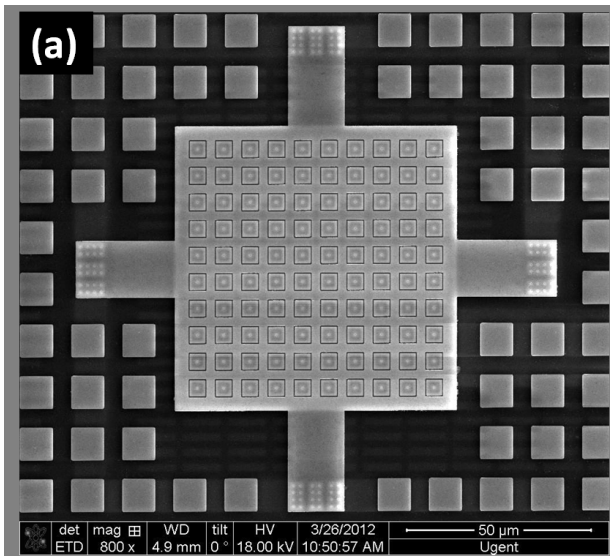

(a)

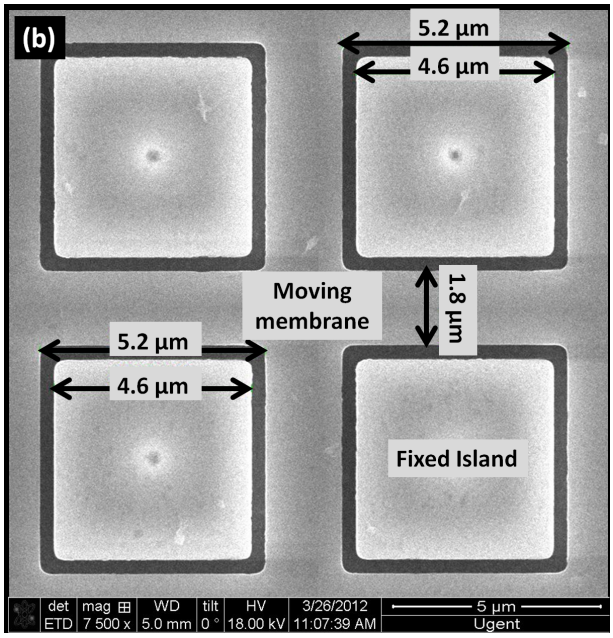

(b)

Figure 4.3: (a)SEM pictures of the top view of the full device with the attaching supports, (b) zoomed-in view of the perforated membrane filled with the fixed islands

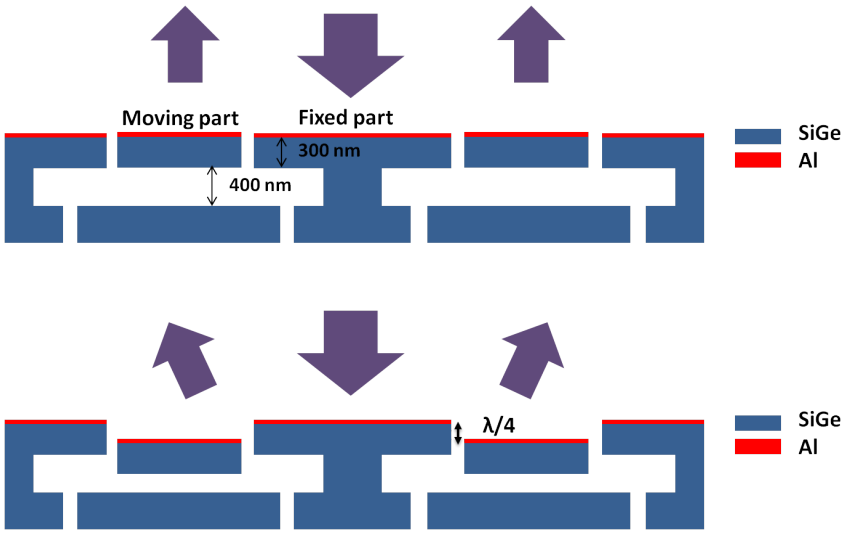

Figure 4.4: Cross-sectional view and working principle of the device.

ders (Fig. 4.4). At a deflection of $\lambda/4$, the light reflected from the membrane and the top of the islands are exactly opposite in phase which results in total annihilation of the 0th order intensity.

Though we used devices of different dimensions, here we discuss the best results as obtained with a perforated membrane with a total dimension of 75 μm x 75 μm, forming a grating with period of 7.0 μm with a fill factor of 0.88. The membrane was perforated with 5.2 μm x 5.2 μm holes within which fixed blocks of 4.6 μm x 4.6 μm were created. A fixed gap of 400 nm was maintained between the membrane and the substrate. The device was suspended on its four sides by supports of 18 μm x 15 μm each, which are then attached to anchors at the outer parts (Fig. 4.3(a)).

4.3 Static characterization

4.3.1 Setup for optical characterization

The optical characterization of the proposed design was carried out using a linearly polarized laser with 400 nm wavelength. This wavelength was selected in accordance to the airgap (400 nm) between the substrate and the membrane in the designed device. Fig. 4.5 shows the experimental set-up used to characterize the VOA. The setup has nearly the same optical configuration as we used to characterize the GLVs except the lens in front of the grating is a convex one which focuses the light as a circular spot (~ 40 μm diameter) with uniform in-

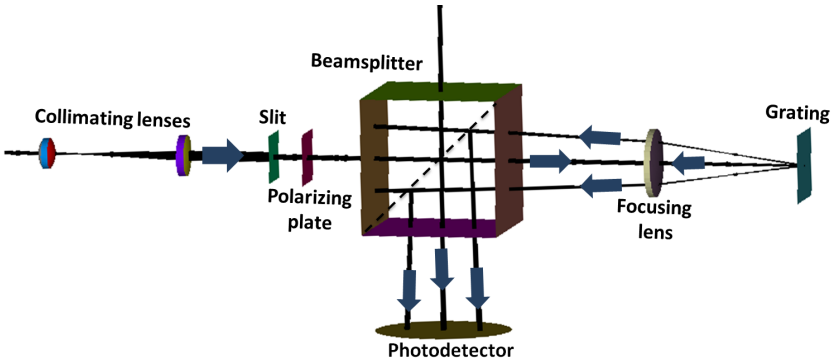

Figure 4.5: Schematic of the optical set-up used to characterize the attenuation of the device.

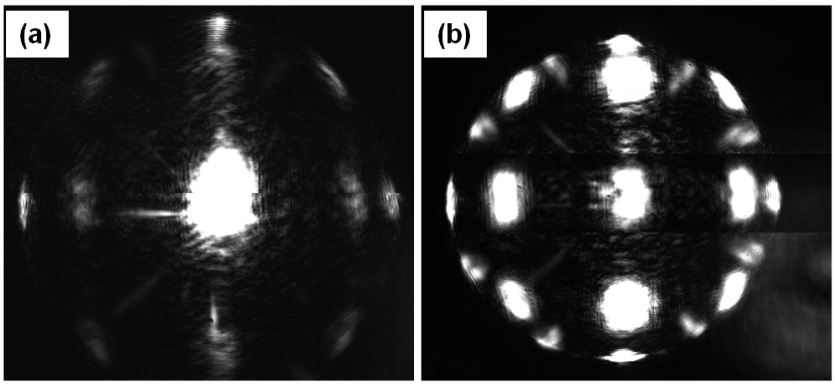

Figure 4.6: (a) Reflecting state of the grating in the non-actuated state, (b) Diffracting state of the 2D grating once actuated showing the fading of the 0th order intensity and increase of intenisty in the higher orders.

tensity on the center of the VOA membrane. The two convex lenses in the front act as a collimator. The beamsplitter helps in separating the incoming and outgoing light. A photodiode in series with a filtering slit was used to measure the intensity of the 0th diffracted order as a function of amplitude of the applied actuation voltage. Additionally, we used a quarter wave plate in front of the beamsplitter to generate the circularly or elliptically polarized light which was used in determining the polarization dependence of the VOA performance.

The device under investigation was mounted on a XYZ stage and was monitored with a microscope which helped us in finding the optimum position (center of the membrane) of the focused spot on the membrane giving rise to the maximum achievable attenuation. As we work with the 0th diffraction order,

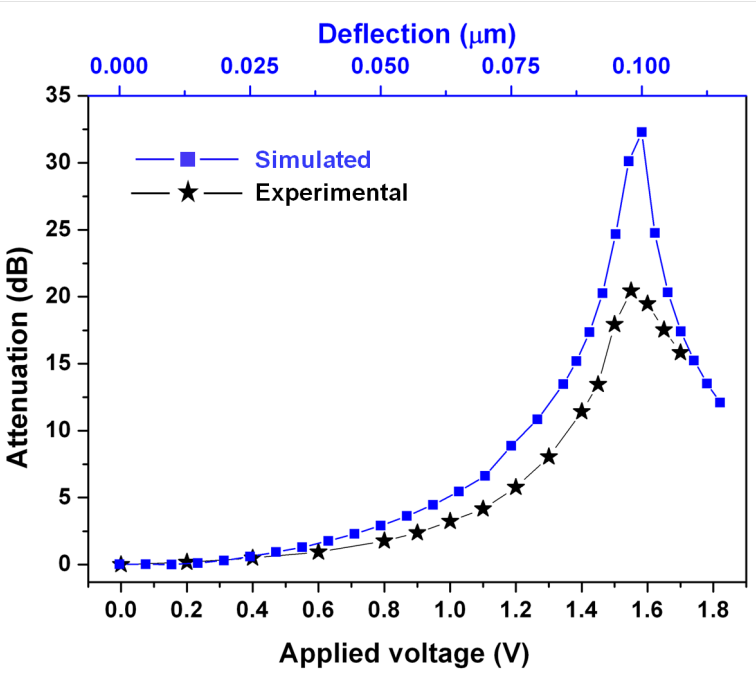

(a)

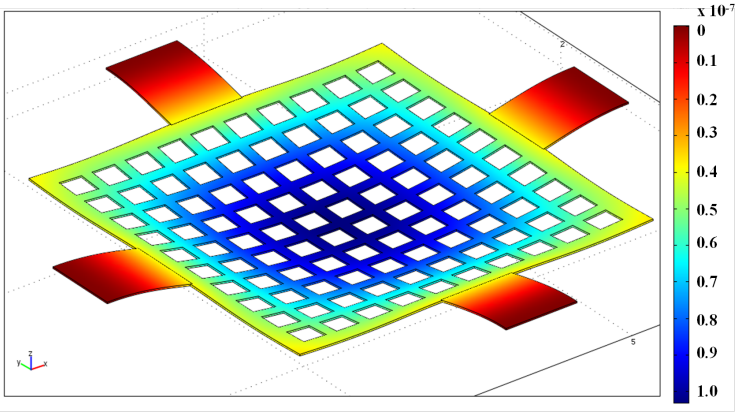

(b)

Figure 4.7: (a) Comparison of the experimental and theoretical attenuation of the proposed device, (b) COMSOL modeling of the electrostatic displacement of the membrane.

a small change in the incidence angle does not significantly influence the efficiency and the attenuation of the gratings under investigation.

4.3.2 Optical characterizations

The insertion loss of the devices was found to be ~ 1.1 dB which is mostly associated with the fill-factor of the grating and the reflectivity of the top layer. We believe that, with finer lithographic precision, the fill factor can be increased further. Moreover, due to the higher reflectivity of Al in the NIR regime, the insertion loss will be even lower in that part of the spectrum. Also, Fig. 4.6a shows some diffracted light in the higher orders in the non-actuated state which is also a contributing factor to the obtained insertion loss. It implies an initial height difference between the posts and the membrane which could be either due to a fabrication error or due to the bending of the membrane. Fig. 4.6b shows an intermediate actuated state of the device where further distribution of light from the 0th order to the higher orders can be observed. The attenuation as function of the applied voltage is shown in Fig. 4.7(a). A clear decrease in the 0th order intensity (increasing attenuation) can be observed with increasing external DC bias. We could obtain a maximum attenuation level of ~ 20 dB with an operating voltage of 1.6 V. The experimental result was also compared to a theoretical calculation carried out using Rigorous Coupled Wave Analysis (RCWA) [11]. While the qualitative behavior matches well, the maximum attenuation level differs by approximately 10 dB between the experimental results and the RCWA based simulations.

To understand this discrepancy, we also performed a COMSOL Multiphysics based simulation studying the deflection of the membrane when applying a voltage. Fig. 4.7(b) shows that the deflection is not uniform as assumed in the RCWA simulations, but that there is a maximum deflection right at the center of the membrane. Hence, light reflected from the off-center parts is less attenuated as compared to that reflected from the center of the membrane. More importantly, due to working with the 0th order mode, the removal of stray light is more challenging in the experimental set-up and hence we experience a decreased contrast.

The PDL was measured at different attenuation levels for four different polarization states of P, S, 45° (w.r.t. the P or S) and elliptical. The attenuation with applied voltage was measured for all the four different polarizations and the maximum deviation was observed between the 45° and the elliptical states. As shown in Fig. 4.8, a maximum loss of 0.11 dB at the highest attenuation of 20 dB was obtained which supports our claim that this device operates as a polarization independent VOA. We think, the increasing PDL with attenuation is because of the deviation of the symmetric shape of the grating due to increased

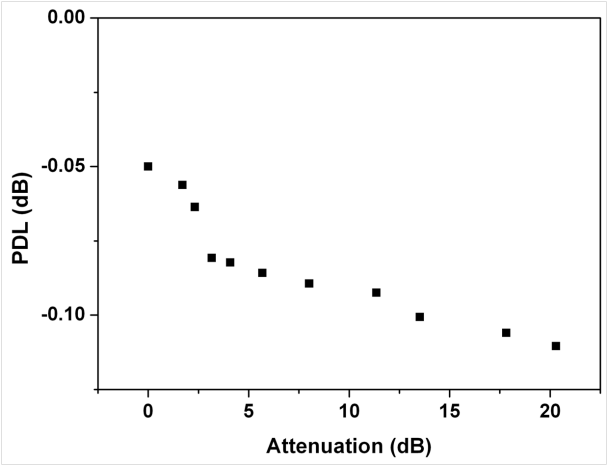

Figure 4.8: Change in PDL with attenuation of the device..

deformation at higher voltage.

4.4 Dynamic characterization

One of the substantial advantages of MEMS based VOAs compared to bulk mechanical systems is their high response speed enabling faster data transfer. Hence, it was important to study the device dynamics of these MEMS gratings. Due to the small underlying airgap and fast operating speed, squeeze film damping becomes the dominant damping mechanism affecting the dynamic response of the device. So, we used Laser Doppler Vibrometry (LDV) to characterize the mechanical behavior of the suspended membrane. A resonance frequency of 320 kHz was obtained for the device as shown in Fig. 4.9. We also studied the damping nature of the device through applying a square wave pulse train with 20 μs period. As evident from Fig. 4.10(a), a critically damped response was obtained for the device with a settling time $\sim$ 3.3 μs (equilibrium $\pm$ 2%). To cross-check the experimental result, the mechanical behavior of the membrane was studied further using COMSOL. These simulations match our experimental results well with a calculated resonance frequency of 343 kHz and a near critical damped response as shown in Fig. 4.10(b). The close match between the experimental and simulated results shows that by properly optimizing the design parameters, a fast settling time can be achieved even when the desired usable range is extended to the NIR regime.

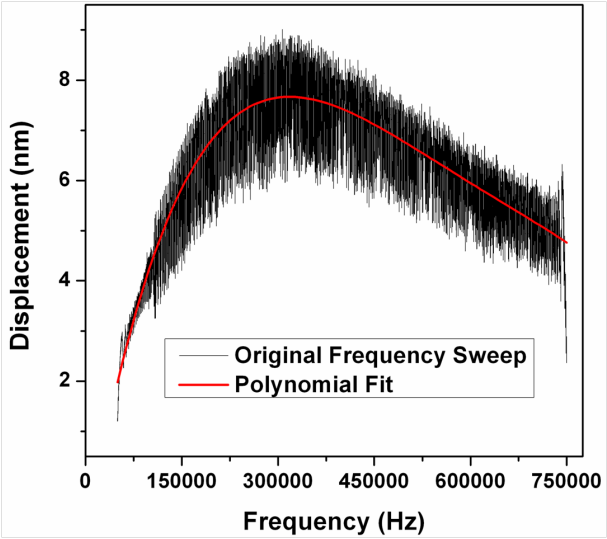

Figure 4.9: Small signal frequency response of the 2D grating showing a resonance peak at 320 kHz.

4.5 Wavelength dependent loss

We also calculated the expected wavelength dependent loss (WDL) for our devices in the C-band used for fiber based telecommunication using RCWA simulations. Fig. 4.11 shows the attenuation as function of the displacement of the membrane for different wavelength of the incident light. Over a 40 nm bandwidth and for an attenuation level of 15 dB there is a maximal variation of 0.9 dB.

4.6 Conclusion

Summarizing the chapter we showed the operation of a grating modulator which is geared towards polarization independent operation. We showed the necessary changes to be made in the device design to form a 2D symmetric grating structure which is insensitive to the direction of the polarization of the incident light. We obtained a maximum attenuation of 20 dB for the devices with a polarization dependent loss of 0.11 dB and a settling time of $\sim 3.3\ \mu$s. We also showed a very close overlap between the experimental and theoretical results regarding the mechanical behavior of the membrane indicating the possibility of optimizing the settling time in case of an altered design geared towards the NIR regime. Overall, these results prove the usefulness of the poly-

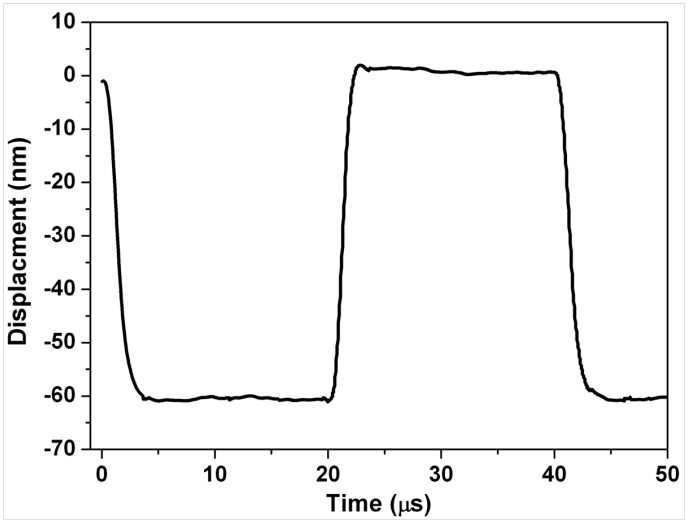

(a)

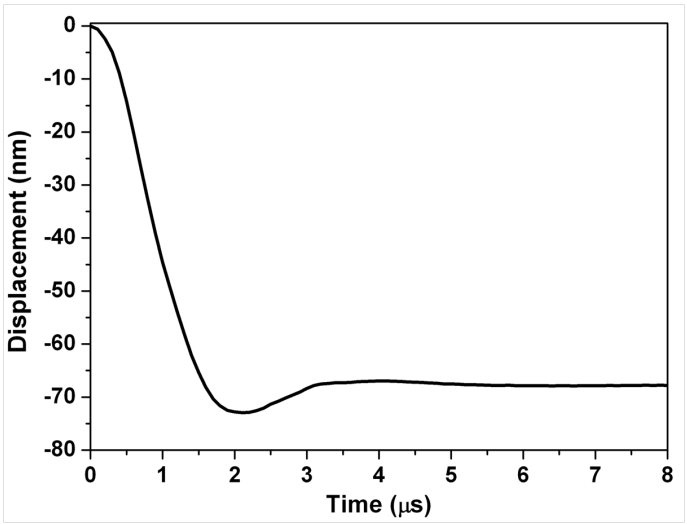

(b)

Figure 4.10: (a) Step-response to a square wave pulse train showing a critical damped nature of the device, (b) Simulated step response of the device showing a near critical damped behavior.

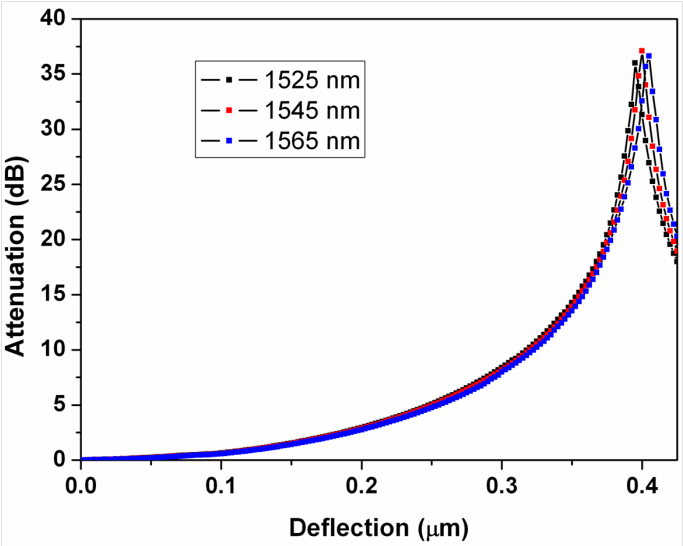

Figure 4.11: Wavelength dependent attenuation characteristics of the device as simulated using RCWA.

SiGe technology in fabricating high quality VOAs. Given the compatibility of this SiGe platform with post-CMOS processing, this can be a step forward in efficiently integrating large arrays of VOAs on a single silicon chip.

References

[1] H. Ishio, J. Minowa, and K. Nosu, "Review and status of wavelength-division-multiplexing technology and its application," *Lightwave Technology, Journal of*, vol. 2, no. 4, pp. 448–463, 1984.

[2] A. Liu, *Photonic MEMS devices: design, fabrication and control*. CRC, 2008, vol. 136.

[3] J. Laude, *DWDM fundamentals, components, and applications*. Artech House, 2002.

[4] M. Puyol, Í. Salinas, I. Garcés, F. Villuendas, A. Llobera, C. Domínguez, and J. Alonso, "Improved integrated waveguide absorbance optodes for ion-selective sensing," *Analytical chemistry*, vol. 74, no. 14, pp. 3354–3361, 2002.

[5] A. Khalid, G. Cossu, R. Corsini, M. Presi, and E. Ciaramella, "Hybrid radio over fiber and visible light (rof-vlc) communication system," in *European*

Conference and Exposition on Optical Communications. Optical Society of America, 2011.

[6] C. Lee and J. Yeh, "Development and evolution of moems technology in variable optical attenuators," *Journal of Micro/Nanolithography, MEMS, and MOEMS*, vol. 7, no. 2, pp. 021 003–021 003, 2008.

[7] R. Jablonski, M. Turkowski, and R. Szewczyk, *Recent advances in mechatronics*. Springer Publishing Company, Incorporated, 2007.

[8] A. Witvrouw, "CMOS-MEMS integration today and tomorrow," *scripta materialia*, vol. 59, no. 9, pp. 945–949, 2008.

[9] J. Ford and J. Walker, "Dynamic spectral power equalization using micro-opto-mechanics," *Photonics Technology Letters, IEEE*, vol. 10, no. 10, pp. 1440–1442, 1998.

[10] E. Tamaki, Y. Hashimoto, and O. Leung, "Computer-to-plate printing using the grating light valve device," in *Proc. SPIE*, vol. 5348, 2004, pp. 89–97.

[11] M. Moharam and T. Gaylord, "Rigorous coupled-wave analysis of planar-grating diffraction," *JOSA*, vol. 71, no. 7, pp. 811–818, 1981.

5

Integrated optic microelectromechanical structures

5.1 Introduction

In the last 30 years, optical fiber networks have been progressively deployed, in long haul (>10 km) telecommunications links first, down to enterprise LAN, metropolitan, and access networks. Nowadays, because of the intrinsic limitation of copper links in high-data rate servers, Internet switches, and supercomputers, optical links are spreading also rapidly in very short reach (VSR) systems [1]. In these systems, copper cables are typically replaced by active optical cables (AOC) using fibers, allowing a concatenated data rate of 100 Gb/s to be reached over tens of meters of multimode fiber ribbons. Compared with electrical interconnect solutions, optical links exhibit several advantages, such as lower signal attenuation, lower dispersion and lower crosstalk leading to superior bandwidth by distance products. However, optical links remain more expensive than electrical links. Hence, to be successful, the next generation of optical components needs to have a lower cost and has to be compatible with high-volume manufacturing.

An obvious way to achieve this requirement is to increase the degree of integration of optical devices. Silicon photonics, using highly confined optical modes in silicon waveguides, offers unique opportunities to cope with this in-

tegration challenge. In addition, it opens the door to simultaneous manufacturing of electronic and optical functions on the same chip using CMOS fabrication lines [2–4] and standard well-mastered microelectronics fabrication processes. The ultimate goal is to monolithically integrate optical transceivers or similar circuits into silicon IC chips. Recent developments have already shown the integration of several elementary optical functions into nanophotonic silicon circuits [4] such as laser emission, detection, modulation, multiplexing, and demultiplexing [5].

Silicon nanophotonic circuits can exhibit a very high level of functional integration due to the very small cross section of the silicon waveguides having a less than 0.5 μm mode-field diameter (MFD). However, to be implemented in data optical transmission networks, such circuits still must be interfaced with optical fibers having much larger dimensions with about 10 μm MFD. Due to this mismatch in size, a coupling structure is required in order to minimize the coupling loss that is obtained. This coupling structure must adapt the wide fiber mode with a narrow silicon wire mode and reduce the insertion loss as much as possible.

5.2 Actively alignable grating coupler

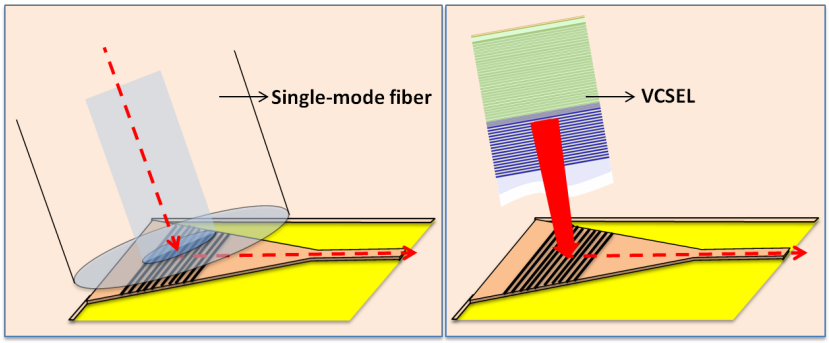

Figure 5.1: Illustration of the Focused Grating Coupler (FGC) showing the grating grooves and the adiabatic tapering leading to a single mode waveguide. The picture shows coupling of light from a single mode fiber or a VCSEL to the FGC.

Due to their compact size and planar structure, surface grating couplers are popular for vertical or quasi-vertical optical coupling between a fiber or a VCSEL and a nanophotonic circuit [6, 7]. They can be located anywhere over the chip and not only at the edge. Therefore, compared to edge-coupling structures [8, 9], such surface couplers allow light coupling without the need for dicing and

polishing the chip edge, which also makes wafer-scale testing of nanophotonic circuits possible. This is the reason why grating couplers are widely used in silicon photonics devices today.

Standard grating couplers in a 220nm silicon-on-insulator (SOI) layer exhibit a coupling efficiency to a single-mode fiber of around 33% as demonstrated by [7]. At the same time, as shown by Taillaert *et al* [10], a 10° angle of the optical fiber w.r.t. the grating normal has to be maintained to reduce the second-order reflection at the waveguide grating interface and to maximize the coupling efficiency. But, given the typical placement accuracy of ~ ±2 μm between an SMF and FGC using passive approaches, it already leads to an additional insertion loss of 0.75 dB at 1.55 μm wavelength. Alternatively, with the use of passive approaches, there lies also the possibility of angular misalignment between the SMF and the FGC which also deteriorates the coupling efficiency. It is shown that the central wavelength of maximum coupling shifts by 9 nm for each degree of change from the optimized angle of 10°.

The insertion loss between the light source (through an optical fiber or from a VCSEL) and a nanophotonic circuit is definitively a big issue as it directly determines the link performance parameters such as the link reach, the signaling rate, the receiver sensitivity, etc. The selection of the coupling structure also has a big influence on the final cost of the device, when taking into account the wafer-level testing capabilities and the packaging requirements, which need integration with fiber assemblies. Hence, considering the extreme sensitivity of the coupling efficiency to a slight misalignment between a single mode fiber and a grating coupler, new solutions are required to reduce packaging costs. Two options can be considered:

1. One option is to use passive alignment approaches like pick-and-place assembly equipment components or using mechanical fixtures for passive core alignment or gluing the fibers directly on top of the desired location of the photonic circuit. Hence, given the tight tolerance on the accuracy of alignment of the fiber position and angle w.r.t. the grating, it is extremely difficult to obtain and maintain the optimum alignment condition.

2. Another option is to use an active alignment procedure where either the light source (Fiber/ VCSEL) or the coupling structure can be actively controlled with sub μm precision using MEMS platforms. Several solutions for in-package fiber alignment can be found in literature [11, 12]. Recently, V-beam actuator based microsystems were reported which have the capability to perform 2-D fiber alignment to a laser diode with a precision of ± 0.1 μm. Another robust technique reported recently, uses a MEMS XY scanner mounted with a micro-lens to actively perform optical alignment of fiber optic modules by steering a beam [13, 14].

Hence, in this work, we looked forward to an alternative solution where a surface coupling structure has the capability to move in-plane or rotate out-of-plane. Given the alignment tolerances stated before, we looked into two different options:

- Possibility of moving the surface coupling structure in-plane which can mitigate a misalignment of ~ ±2 μm between an SMF and FGC with an accuracy of ~100 nm, or
- Possibility of tilting the surface coupling structure out-of-plane which can steer the light ~ 4-5° with an accuracy of 0.1°.

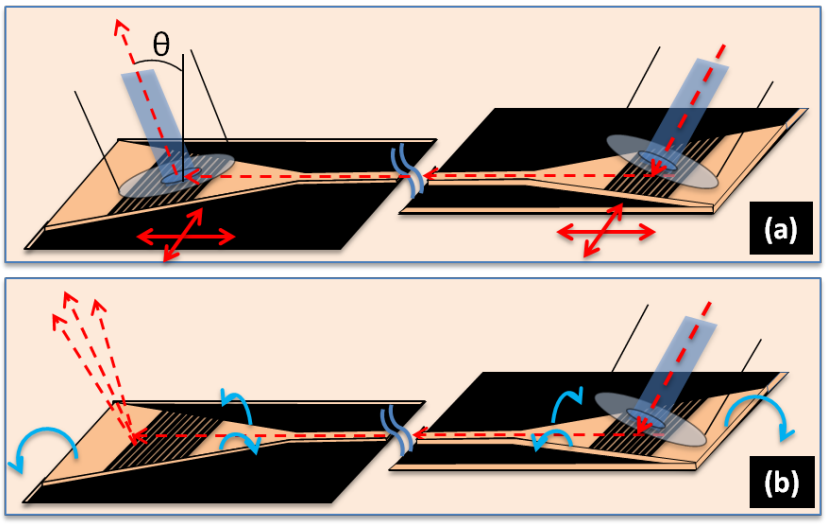

Figure 5.2: Conceptual illustration of the motivation behind the integrated optic microelectromechanical structures showing the possibility of moving the FGC in the orthogonal planar direction to minimize the misalignment between the FGC and the SMF at the in-coupling side(a), and tilting the FGC at the out-coupling side generating the possibility of beam steering with the purpose of directing the signal in the desired direction (b).

Looking at the alignment tolerances and accuracies, a MEMS based system is undoubtedly a very promising option to achieve sub-micron displacement or sub-degree tilt of the coupling structure. In this chapter, we propose a novel idea in which the grating coupler can be moved in plane with the help of comb-drive actuators in all possible directions and therefore can be accurately positioned with sub-micron precision (5.2a). Alternatively the grating coupler can be tilted

in the out-of-plane direction using capacitive MEMS structures [15] and hence the out-coupled light can be steered two-dimensionally (5.2b). This structure e.g. has the potential to simplify the alignment for free space interconnects between different silicon photonics chips.

5.3 Device layout

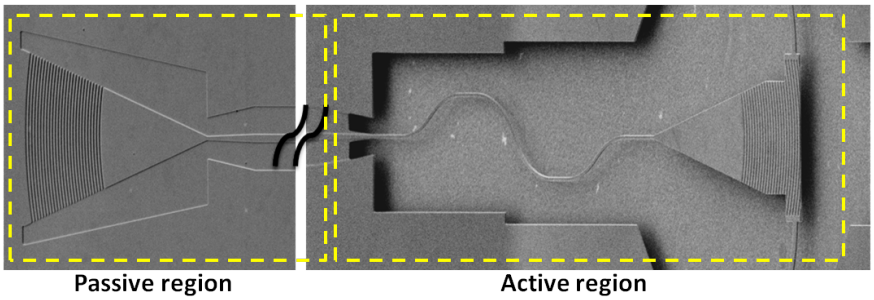

Figure 5.3: General schematic of segmentation of the functional devices into passive and active regions.

The general layout of the devices we designed (Fig. 5.3) can be split in two different sections: (i) passive region, (ii) active region.

(i) The passive region consists of a shallowly etched FGC (70 nm etch) which is tapered to a ~3 mm long shallow etched rib waveguide (70nm etch depth and 0.9 μm width). At the end of the shallow waveguide, there is another tapered transition, from the shallow rib waveguide to a spring shaped deeply etched waveguide.

(ii) The active region starts from the spring shaped freely hanging single mode waveguide (0.45 μm width). Each turn of the spring shaped waveguide was of 10 μm bend radius which is further connected to a deeply etched FGC (220 nm etch boundary). This FGC is further connected with other MEMS structures which enable it either to move in plane or rotate out-of-plane.

5.4 Basic components

A brief description of the basic components that were used to form the devices are described below:

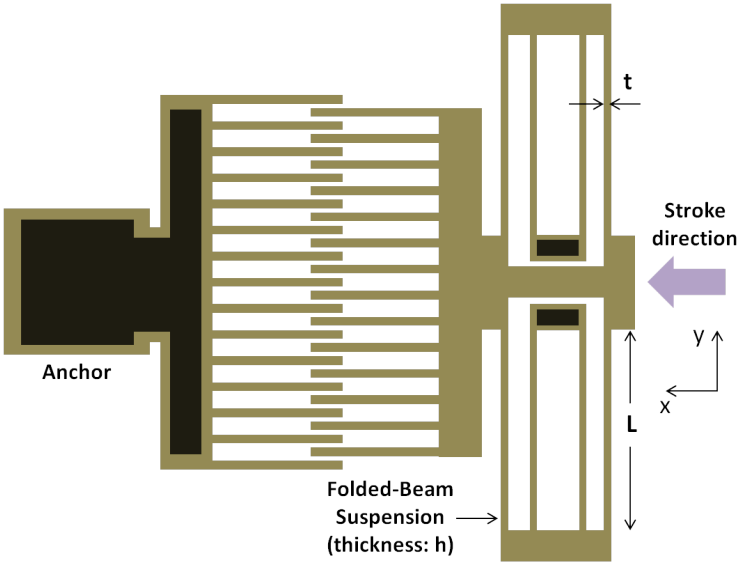

Figure 5.4: Schematic of a comb-drive actuator showing the oppositely acting electrical and mechanical forces within the system.

5.4.1 Comb-drive actuators

Comb drives are often used in devices with structures held by mechanical springs. They can be used either for in-plane rotational or lateral actuation or for out-of-plane motion.

Figure 5.4 shows a schematic view of a comb-drive actuator. If h is the height of the device, N_F is the number of fingers and g is the gap between the combs, the resulting force for an applied voltage U can be approximated as follows [16, 17]:

$$F_E \approx -\varepsilon_o \varepsilon_r \frac{hN_F}{g} U^2 \tag{5.1}$$

The elastic restoring force of a beam is given by eq. 5.2 where E is the Young's modulus, L is the length of the spring and t is its width:

$$F_M = \frac{Eht^3}{L^3} x \tag{5.2}$$

where, x is the displacement of the comb fingers due to the electrical force.

The sum of the forces in the situation of Fig. 5.4 gives the following displacement versus the voltage [18]:

$$x = \frac{1}{2}\frac{\varepsilon_o \varepsilon_r N_F L^3}{gEt^3} U^2 \tag{5.3}$$

In this case, the displacement depends on the square of the voltage.

Eq. 5.1 is valid only if the movable fingers are perfectly centered between the fixed ones. If this is not the case, the lateral forces create an instability in the system. Comb-drive actuation can be described as an instable equilibrium. To avoid any lateral motion of the movable part of the actuator, the mechanical springs have to be correctly designed and optimized.

5.4.2 Compliant S beams

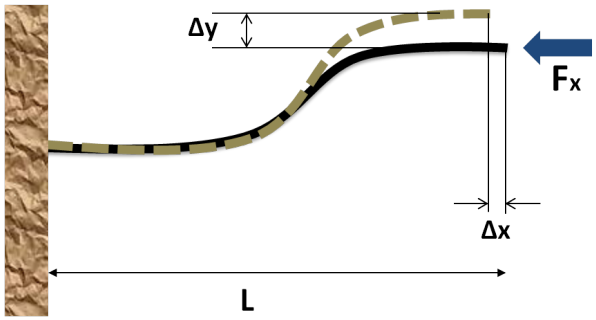

Figure 5.5: Bending of a flexible 'S' beam when force is applied on one end of it in the x-direction while the other end is fixed.

In the laterally moving structures we used 'S' shaped flexible beams [14], which are designed to convert two unidirectional (X) actuations into two dimensional (XY) displacements and to amplify the movement of an attached proof mass in the direction orthogonal to the moving direction of the actuators by a factor of two. The curvature of the S-beams is given by the following formula [14]:

$$y(x) = \frac{\sqrt{2}}{4}x - \frac{\sqrt{2}L}{8\pi} sin\left(\frac{2\pi}{L}x\right) \tag{5.4}$$

where, L is the length of the beam in the x-direction. The bending characteristic of the S-beam is illustrated in Fig. 5.5. If one end of the S-beam is fixed and a unidirectional force in the x direction is applied to the beam from its other end, the tip of the beam moves in both x and y directions.

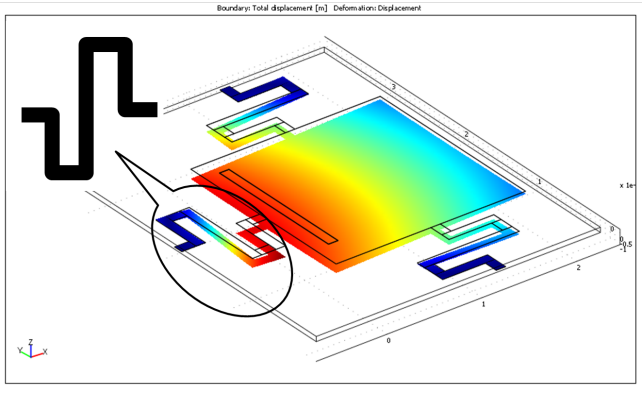

Figure 5.6: Use of serpentine beams for out-of-plane movement of attached mass.

5.4.3 Serpentine beams

The serpentine beams we designed for holding the out-of-plane rotating grating couplers are composed of two short beam segments folded around in the shape of a 'S' and connected to the sides of a mass. The serpentine beams or meander type beams are designed to achieve a lower spring constant for out-of-plane motion of MEMS switches to achieve a low actuation voltage [19]. Adding more meanders can significantly lower the spring constant without excessively increasing the required space as miniaturization is necessary for a device to be embedded in applications. As shown in Fig. 5.6, when properly designed, it also helps in keeping the shape of the attached mass intact during the out-of-plane deformation.

5.4.4 Integrated waveguides

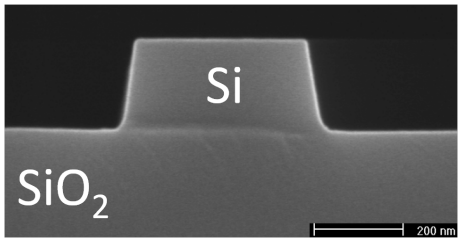

Figure 5.7: SEM cross section of an integrated strip waveguide on SOI.

The key functionality of a photonic waveguide is its ability to guide light. Op-

tical fibers for example are a well-established propagation medium due to their low propagation losses of 0.2 dB/km [20]. On an integrated platform, losses are typically higher. The propagation losses for a 450 nm wide, 220 nm high strip waveguide on SOI (Fig. 5.7), is between 2-3 dB/cm with bend losses of less than 0.01 dB/90° bend for a 5 μm radius [21]. The main loss factor is scattering at the edges of the strip waveguide. By using rib waveguides, the loss can be reduced by an order of magnitude to less then 0.3 dB/cm. When using these waveguides in our devices, we used a short taper (10-15 μm) to make the transition from a 0.9 μm wide rib waveguide to a 0.45 μm wide strip waveguide or vice versa.

5.4.5 Focusing grating coupler (FGC)

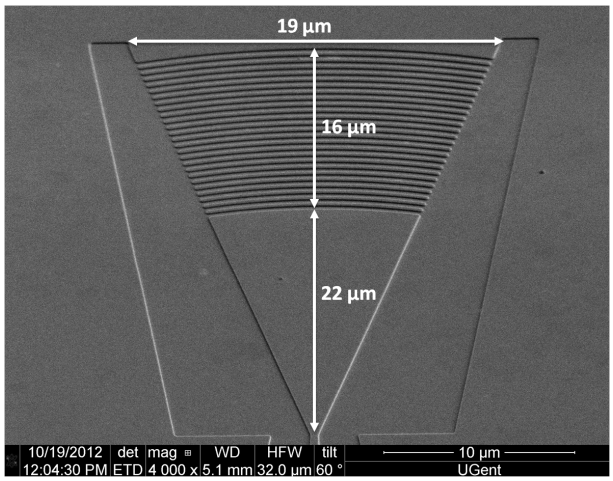

Figure 5.8: SEM top view (tilt = 60°) of a shallow etched focusing grating coupler on SOI.

When using a straight 1-D grating, the light from the fiber is first diffracted into a 10-12 μm wide, multimode waveguide, which is then adiabatically tapered down to the photonic wire (450 nm wide). As a result, we have a very compact grating in combination with a relatively long taper (typically ~150 μm long). However, by curving the grating lines, the light can be focused onto the single-mode wire waveguide, and the taper can be omitted [22], as shown in Fig. 5.8. In our FGCs, the elliptical grating grooves are 70 nm deep with a period of 630 nm. As described earlier, we have used two different FGCs in our devices; in the passive region, the FGCs are shallowly etched (70 nm etch) at the sides whereas in the active region, the FGCs are deeply etched (220 nm etch).

5.5 Creating structures

The photonic components used in this work were fabricated in IMEC using the standard passives process, using the ePIXfab multi-project foundry service. The formation of the metal pads and the following release of the microstructures was done by myself, in the UGent cleanroom.

5.5.1 Standard passives process of IMEC

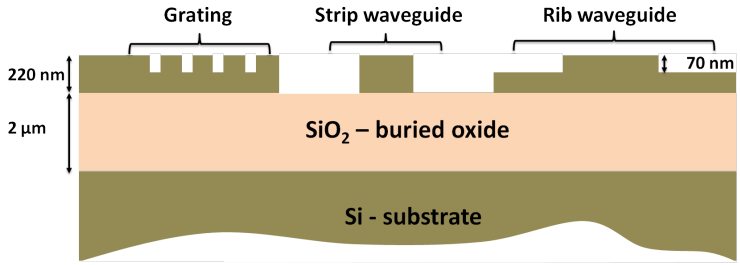

Figure 5.9: The different photonic components fabricated in IMEC on the SOI wafer. The 220nm deep etch is used in fabricating the strip waveguides whereas the shallow etch of 70 nm is used in making the rib waveguides and the gratings [23].

The photonic components in the standard passives run are processed on a 200 mm SOI wafer from SOITEC [24] with a 2 μm buried oxide layer and a 220 nm top Si layer. Two etch steps are used in the standard passives process using deep-UV 193 nm lithography. The fabrication details can be found in [21]. There is one full etch of 220 nm that allows fabricating strip waveguides and another etch of 70 nm to fabricate rib waveguides, taper sections and gratings as can be seen schematically in Fig. 5.9.

5.5.2 Surface micromachining

As described before, surface micromachining is a fabrication method that uses thin film deposition, patterning via photolithography and chemical etching to build mechanical structures on top of a substrate, typically a silicon wafer. It is a layered fabrication process in which some layers form structural elements and others are etched away. The layers are referred to as the structural layers and the sacrificial layers respectively, and form the building blocks of the process. These set of steps can be repeated several times in order to create complicated structures, often with moving parts. The key steps that were used to form our devices are described below:

5.5.2.1 Lift-off

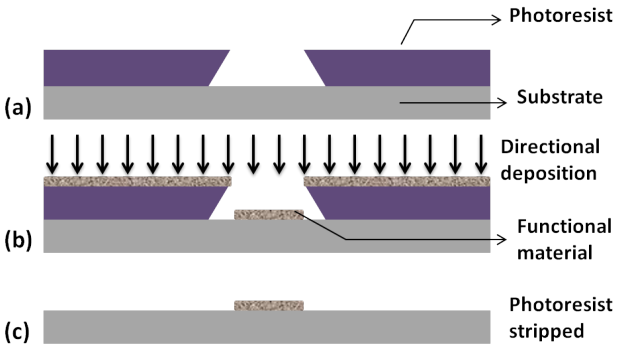

Figure 5.10: Steps in a lift-off process: (a) deposition and patterning of the photoresist on a substrate; (b) deposition of the desired material via a line-of sight method; (c) stripping of the photoresist and lifting-off the unwanted material.

Lift-off is a surface micromachining technique in which a material is selectively deposited on a wafer by making use of a temporary layer which is ultimately removed. First photoresist is spun on a wafer and using lithography, it is selectively exposed, creating the desired pattern (Fig. 5.10a). Care is taken to ensure that the resist has either straight side walls or more desirably, a reentrant shape. Next a material is deposited through the photoresist mask via a line-of-sight method, such as evaporation (Fig. 5.10b). Since a line-of-sight method is used, some shadowing takes place, leaving at least part of the photoresist sidewalls without any deposited material on them. When the photoresist is stripped, it therefore leaves behind only the material deposited through the opening, lifting off the material on top of it (Fig. 5.10c). Naturally the thickness of the deposited material needs to be thinner compared to the resist thickness for the techn ique to work. Lift-off is most often used to deposit metals, especially those that are hard to etch using plasmas.

Formation of metal pads: For our devices we used the technique of image reversal using the AZ 5214 photoresist [25]. Standard contact mask lithography was used to selectively open the resist layer where the metal connection needed to be formed. It was followed by a metal deposition process consisting of 200 nm evaporated Au layer on top of a 15 nm thick sputter deposited Ti which was used to enhance the adhesion. Later the metal deposited samples along with the photoresist was cleaned thoroughly in acetone to finish the final step of the lift-off to form the metal connection on top of the SOI samples.

5.5.2.2 Release of the microstructures

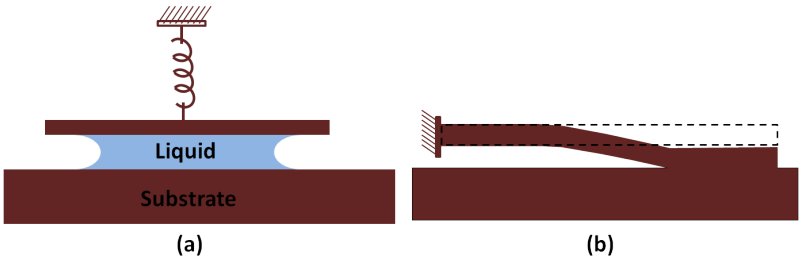

Figure 5.11: Schematic illustration of: (a) the formation of a liquid meniscus during the the sacrifical etch, and (b) sticking of the released parts due to surface tension at the final phase of evaporation.

The final step in the process of fabricating surface micromachined MEMS is a wet chemical etch, which removes the silicon dioxide matrix that encapsulates the movable mechanical structures. Removal of the water from the liquid etchant results in a meniscus (liquid-air interface) that often pulls movable structures into contact via capillary forces. Once in contact, even after drying, the surfaces often remain in contact due to various types of adhesion forces (e.g. capillary, van Der Waals, electrostatic due to trapped charge) resulting in a stuck, or stiction-like failure as shown in Fig. 5.11.

As an object's size decreases, its volume decreases by a power of three - and so does inertia. Because surface tension decreases in direct proportion to the object's length, any reduction in surface tension is relatively small. So as size goes down, surface tension decreases only by a power of one, while inertia drops by a power of three. In the subminiature world of MEMS, objects are a million times smaller than the ones we are used to in daily life. So the differences are sufficiently skewed to make intuitive thinking on this scale extremely difficult.

There are several solutions that have been used by researchers and MEMS manufacturers to reduce the chances for stiction. One approach calls for coating the substrate surface with a thin hydrophobic layer [26], thereby repelling liquid from the surface. Another popular technique is to dry surfaces using super-critical CO_2 [27]. This removes fluid without surface tension coming into play. Still other techniques utilize "stand-off bumps" on the underside of moving parts [28, 29]. These bumps act as pillars, propping up movable parts wherever surface tension may form. However, the most effective method for avoiding stiction is simply to use dry or quasi-dry etching techniques for release wherever possible.

A possible approach is to use a hydro-fluoric acid (HF) vapor phase etching (VPE) system [30]. This enables the removal of silicon dioxide in a vaporous

environment rather than in an aqueous solution [31]. The silicon oxide is etched in a quasi-dry method and is never in contact with a liquid. No cleaning or rinsing of the chips is needed.

To describe the process, Offenberg et al. [32] proposed a two step reaction where first the oxide surface is opened by formation of silanol groups by adsorbed water. Subsequently the silanol groups are attacked by the HF:

$$SiO_2 + 2H_2O -> Si(OH)_4 \tag{5.5}$$

$$Si(OH)_4 + 4HF -> SiF_4 + 4H_2O \tag{5.6}$$

The above formula shows that water acts as initiator of the etching process as well as reactant. This fact suggests that the etching process can be temperature controlled to maintain the amount of water needed to initiate the process and the amount of reactant water in equilibrium.

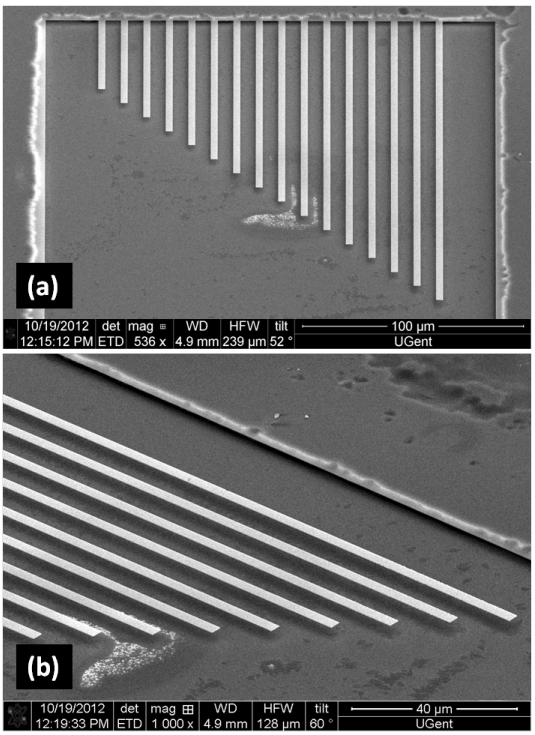

Figure 5.12: SEM pictures of the successful release of 220 nm thick and 2 μm wide Si cantilevers on top of 2 μm thick SiO_2 without sticking; where the length of the cantilevers varies from 50 μm to 200 μm.

We used the HF VPE apparatus from IDONUS to release all our MEMS devices. A detailed description of the working principle of the apparatus and its

mechanical realisation can be found in [33]. In this system, the HF evaporates at room temperature and the etching process starts spontaneously. The etch rate is controlled by the wafer temperature that can be adjusted from 35°C to 60°C. The water film on the wafer is evaporated at moderate temperatures. We experimentally found that the etch rate decreases with increasing temperature and stops completely at temperatures above 52°C when using 50% concentrated HF.

Process optimization: Starting with a clean and dry surface of the samples was the most important pre-condition to obtain a uniform etching rate for successful release of the structural layers. Hence, the separate dies were first cleaned with acetone, IPA and de-ionized water and later dried with N_2. Next, the samples were thoroughly dried at an elevated temperature of 150 °C for 15 minutes to ensure that no moisture is left on the samples before they were put inside the VPE. Particularly, the metal deposited samples suffered from frequent stictions even after thorough cleaning and drying of the samples before starting the etching process. The situation worsened with any residual resist left on the samples after the lift-off. Additionally, after a long etching time (~ 2-2.5 hrs), we observed peeling of the metal layers deposited on top of the Si structure. Hence, we had to add an intermediate step of rapid thermal annealing of the metal deposited samples at 430°C to enhance t he adhesion of the Au films deposited on Si. Even after taking all the precautions, we observed non uniform etching and sticking of the released samples when etched at temperatures lower than 40 °C. However, we could achieve a stiction free release of our devices when the buried oxide was etched at a temperature of (≥)42°C which resulted in an etch rate of ~ 5-6 μm/ hr. In this way, we could obtain a reproducible etching process though a few inconsistencies remained.

Fig. 5.12 shows an example where 220 nm thick and 2 μm wide Si cantilevers with length upto 200 μm are released successfully without stiction after removing the 2 μm thick SiO_2 layer. For these devices, we had to go to higher temperature of 43.5°C to release the longer cantilevers, which gave us an etching rate of ~1 μm/ hr.

5.6 In plane moving devices

SEM pictures of the in plane moving device are given in Fig. 5.13(a). The actuator consists of 3 major elements (5.13(b)):

1. The first is the focusing grating coupler (FGC) which is the principal micro-optical component of the device and the central component of the active region. To decrease the weight of the proof mass (here the FGC) attached to the comb drives, the FGC is cut down from the sides and the

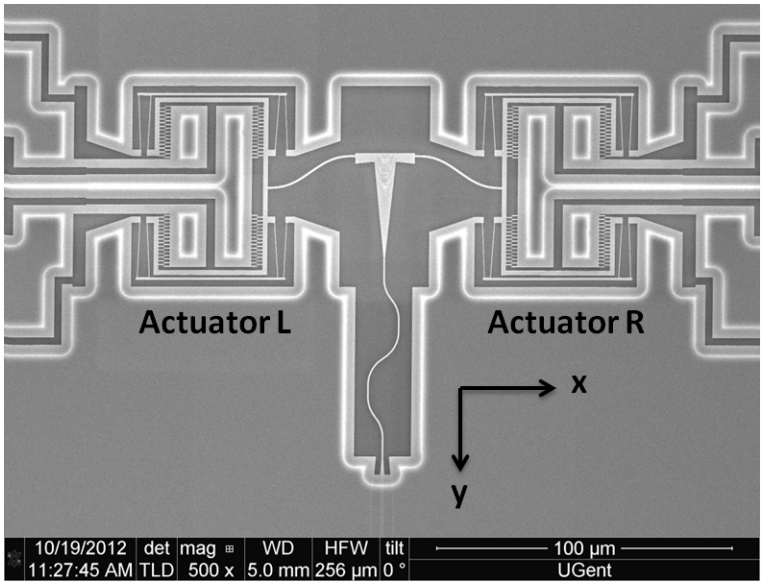

(a)

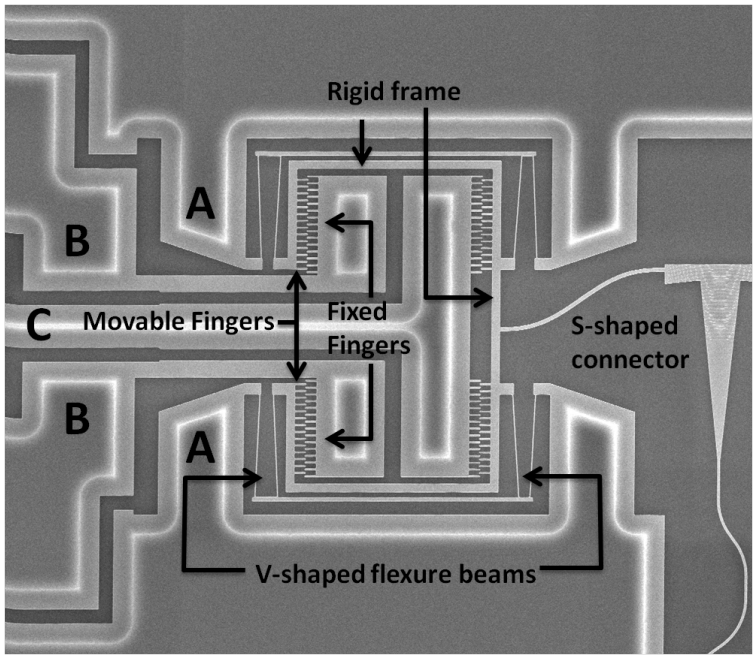

(b)

Figure 5.13: (a) SEM picture of the top view of the planar moving devices showing the two actuators on both the sides of the FGC (a), and close-up view of the specific actuators and the different components of it (b).

top, making it smaller and lighter (Fig. 5.13b).

2. The second is a system of curved compliant suspension beams. The curved 'S' shape [14] is designed to convert a unidirectional actuation into a bidirectional displacement (see section 5.4.2).

3. The third element comprises of comb-drive actuators where the moving fingers are attached to a rigid frame which is further attached to the fixed parts of the chip by 'V' shaped springs [18].

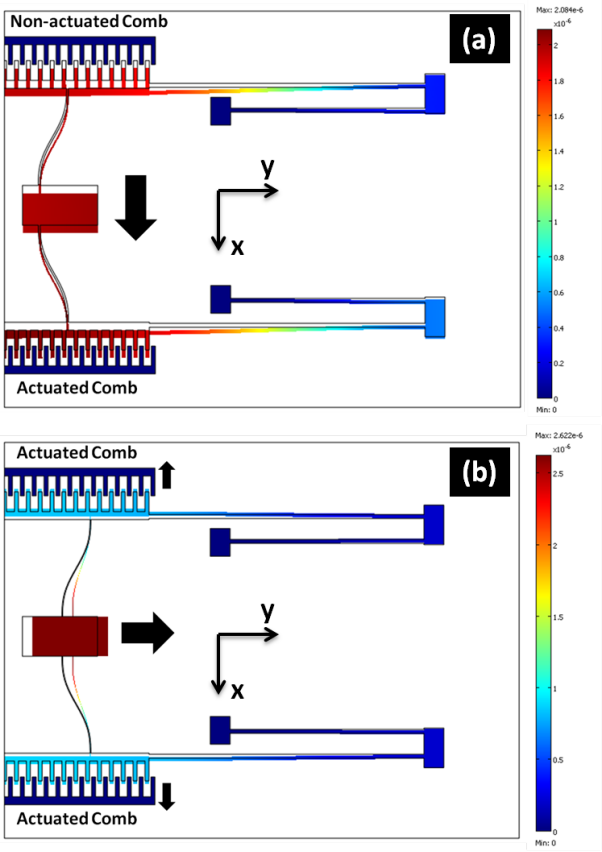

Figure 5.14: COMSOL Multiphysics simulation of the functioning of the planar device when both the actuators are moving in the same direction (a), and opposite direction (b).

The active FGC along with the movable comb fingers (region A) are always kept at ground potential whereas the two separate fixed comb structures (region B and C) are always maintained either at ground or higher potential respectively

depending on the direction of the desired movement. The boundaries between these three regions A, B and C are etched completely through the silicon, allowing for separate electrical actuation.

In our design (Fig. 5.13b), each of the combdrive actuators consists of 28 pairs of fingers of 300 nm width, 2 μm length and 300 nm gap between each pair. The rigid support is 1.5 μm wide and 56 μm long. The 'V' shaped springs are 120 nm wide and 18 μm long and are connected by another 0.75 μm wide rigid structure. The 'S' shaped connectors are 29 μm long and 0.75 μm wide.

COMSOL modeling: The principle of operation of a slightly simplified version of our MOEMS structure is shown in Fig. 5.14. When the two actuators (L and R in Fig. 5.13a) are moving in the same direction and by the same amount (5.14a), the platform translates in the same orientation and by the same distance (displacement in X direction). On the contrary, when the two actuators are moving in the opposite directions by the same amount (5.14b), the platform translates in the orthogonal direction (displacement in Y) by either compressing or extending the compliant 'S' beams. By combining these basic displacements and applying different signal amplitudes to the comb drive actuators, any off-axis points of the reachable area (~ $\pm$ 1.3 μm in both orthogonal directions) can be addressed.

5.7 Out-of-plane moving devices

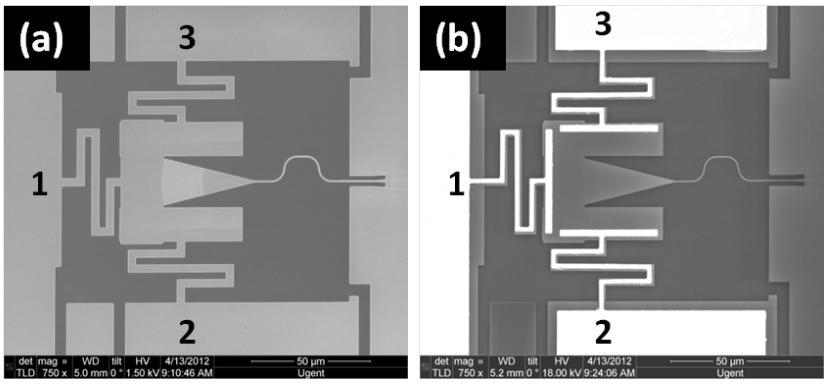

Figure 5.15: SEM pictures of the top-view of: (a) the basic SOI structure with the grating coupler and the MEMS platform, (b) released device after Au deposition on the serpentine beams and the rectangular blocks for electrical actuation.

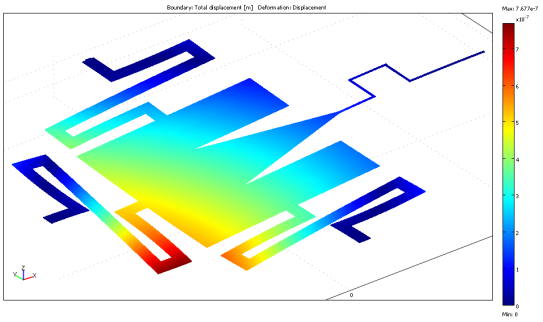

(a)

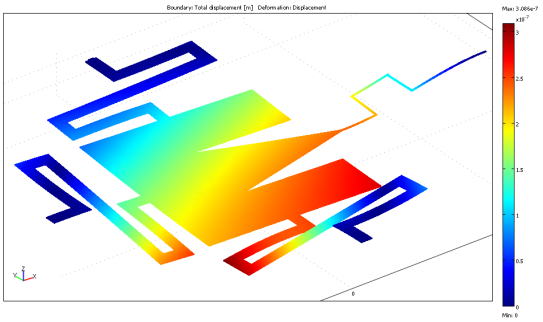

(b)

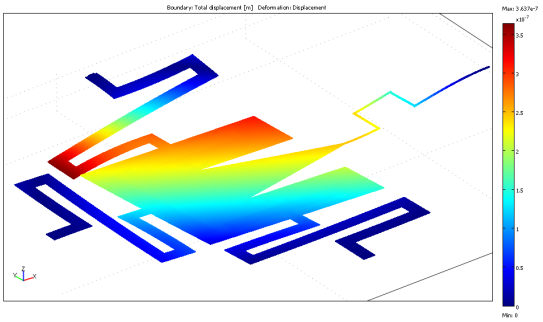

(c)

Figure 5.16: (a) COMSOL Multiphysics simulation of tilting of the out-of-plane moving devices showing the effect of actuation (Fig. 5.15) of: the back pad 1 (a) and the side pads 2 (b) and 3 (c). During actuation of the individual pads, the other two pads were always kept at ground potential along with the substrate.

SEM pictures of the out-of-plane moving device are given in Fig. 5.15. The actuator consists of three major elements:

1. The first is the deeply etched focused grating coupler (FGC) which is also the principal micro-optical component of the device and the central component of the active region. The FGC is held in a 'U' shaped silicon platform.

2. The whole silicon platform is held up by three identical serpentine structures as shown in Fig. 5.15a. Three rectangular metal pads were formed on the outside of the U-shaped silicon slab, as shown in Fig. 5.15b. These actuator pads are connected to the probe pads through metal lines running over the serpentine structures. The three regions (numbered 1, 2 and 3) where the serpentine beams are attached, are individually isolated by etching completely through the silicon, allowing for separate electrical actuation.

3. The third crucial part of the structure is the substrate. To achieve out-of-plane rotation, a voltage is applied between 1/2/3 w.r.t. the substrate. The fabricated device is glued to a copper plate using conductive glue to form the ground connection of the substrate.

The ultimate goal of the proposed structure is to steer the light coupling out from the active grating coupler independently in two orthogonal directions through actuating the three separate metal pads on the three different sides of the rectangular blocks. When a single side is actuated, (keeping the remaining two pads grounded with respect to the substrate), a large force acts on it, tilting the device vertically downward along that side resulting in steering of the outcoming light.

COMSOL modeling: Fig. 5.16 shows the COMSOL Multiphysics simulation of the deformation of a similar working device where the force is applied on the three different pads of the MEMS structures. As shown earlier, the advantage of using the serpentine structure [15] compared to a straight connection is that it decreases the stiffness of the vertical motion and at the same time it should help to keep the shape of the rectangular intact during the deformation. Given the pull-in constrained maximum displacement of ~0.65 μm at the individual sides of the 50 μm wide platform, the maximum angle by which the outcoming light from the FGC can be tilted is ~0.8°. Reducing the platform size should allow larger angles in future devices.

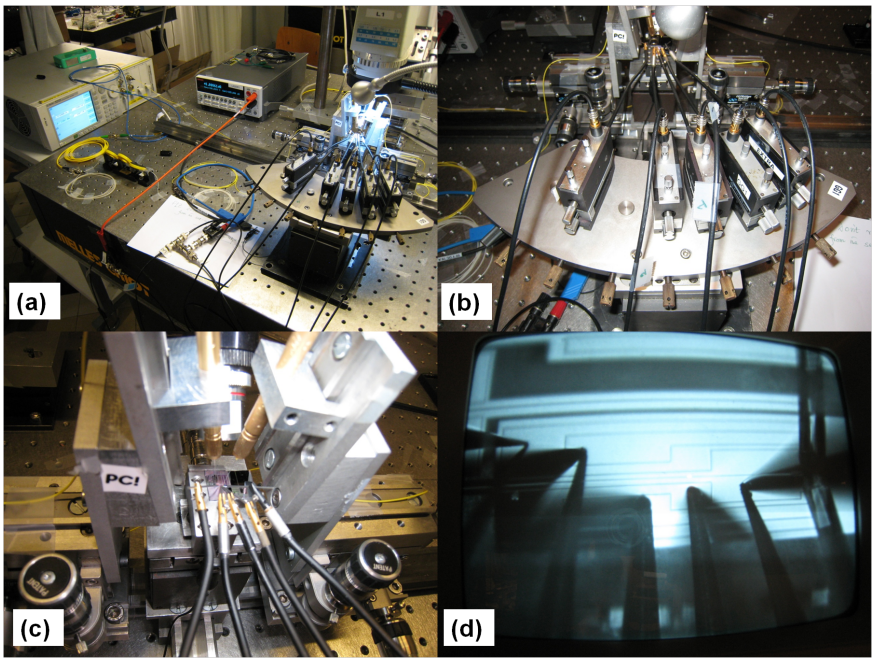

Figure 5.17: Schematic of the experimental set-up that was used to measure the integrated optic MEMS devices, where the full experimental set-up is shown in (a), the electric probes are shown in (b), the fiber holding blocks and the fixed wafer are shown in (c), whereas (d) shows the positioned electric needles on top of the different pads of the planar moving device.

5.8 Experimental Set-up and Calibration

We used a pair of single mode fibers (SMF) to measure the transmission spectra through the devices. One fiber was used to couple light at the passive region, in the fixed grating coupler, while the other fiber is used to sense the motion of the movable grating coupler at the active region. The fibers are tilted 10 degrees with respect to the normal (Fig. 5.17c) of the FGC to avoid unwanted back reflection from the grating. A detailed description of the optical set-up can be found elsewhere [10].

A grounded steel block with vacuum holes was used to fix the devices which helped in keeping the substrate always at ground potential. Electrical probes were used to actuate the separate pads of the MEMS structures as shown in Fig. (5.17b and 5.17d). For the in plane moving devices, the released structures were always kept at ground potential ensuring that these parts never experience any vertical force due to a potential difference with the substrate.

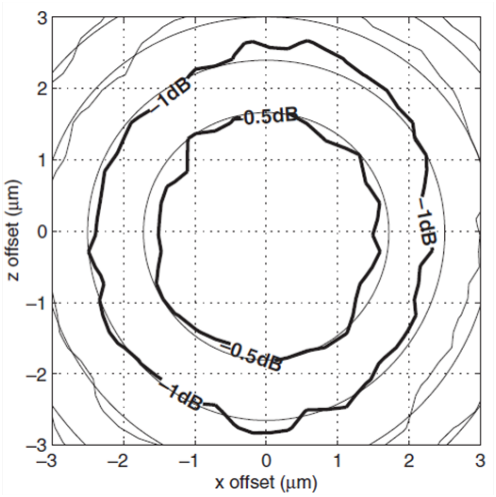

Figure 5.18: Measured (black) and simulated (grey) fiber to waveguide insertion loss (in dB) tolerance through a grating coupler as reported in [7].

For the planar MEMS devices, we used the concept described by Taillaert *et al* in [7]. As shown in Fig. 5.18, as the SMF or the FGC is displaced from its optimum position, the coupling efficiency goes down and for ~1.4 μm displacement of the fiber, an additional loss of 0.5 dB is measured. Hence, we calibrated our planar MEMS structures based on Fig. 5.18 to understand the displacement of the FGC due to the actuation of the comb drives.

For the out-of-plane moving device, we used the grating coupler equation as the basic guideline to follow the tilt of the FGC w.r.t. the fiber. For the grating couplers, the central wavelength of the trasmission spectra is determined by the following equation:

$$\lambda_0 = \Lambda(n_{eff} - sin\theta) \tag{5.7}$$

where Λ is the period of the grooves, θ is the angle made by the fiber w.r.t the normal of the FGC and n_{eff} is the effective refractive index of the guiding layer in the grating.

It shows that when the grating coupler is titled in the backward direction (Fig. 5.2), the fiber to FGC angle θ decreases and as a result the central wavelength gets red shifted. Whereas, if the grating coupler is tilted sidewise (left or right), then the angle θ remains intact but the optimum position between the FGC and the fiber is changed which results in extra coupling loss at a constant central wavelength.

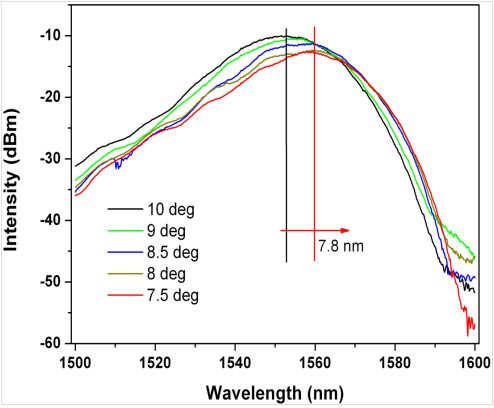

Figure 5.19: A calibration measurement showing the change in transmission spectra with change in angle of the fiber to the grating coupler.

Hence, we first characterized the effect of tilting the fiber while keeping the devices stationary and unactuated. Fig. 5.19 shows how the transmission spectra changes when decreasing the angle (θ) of the fiber w.r.t. the normal of the active grating coupler. As can be observed, the maximum intensity reduces and there is a red-shift of the wavelength for maximum transmission, as can be expected from eq. 5.7.

5.9 Experimental results

5.9.1 In-plane moving devices

As mentioned above, we based our characterization of the in-plane moving gratings on the changes of the coupling efficiency (and hence the transmission through the device) when actuating the comb drives. First, in the non-actuated condition of the device, the fiber is aligned such that the transmission between the FGC and the fiber is maximized. Then, the two different actuators 'R' and 'L' were actuated together or separately to achieve displacement of the FGC in the desired direction.

Fig. 5.20 shows one such example where the FGC is actuated in the -ve x direction. For this, when the pads 'A' and 'B' (Fig. 5.14b) were kept at the ground potential, pad 'C' was at a higher potential for actuator L which actuates the connected comb drives. Similarly, for the actuator R, the disconnected combs were actuated which helps together with actuator L in pushing the FGC towards the -ve X direction. The transmission spectra are shown in Fig. 5.20a for the different positions of the FGC and the SMF. For clarity, we perfomed a 3rd order

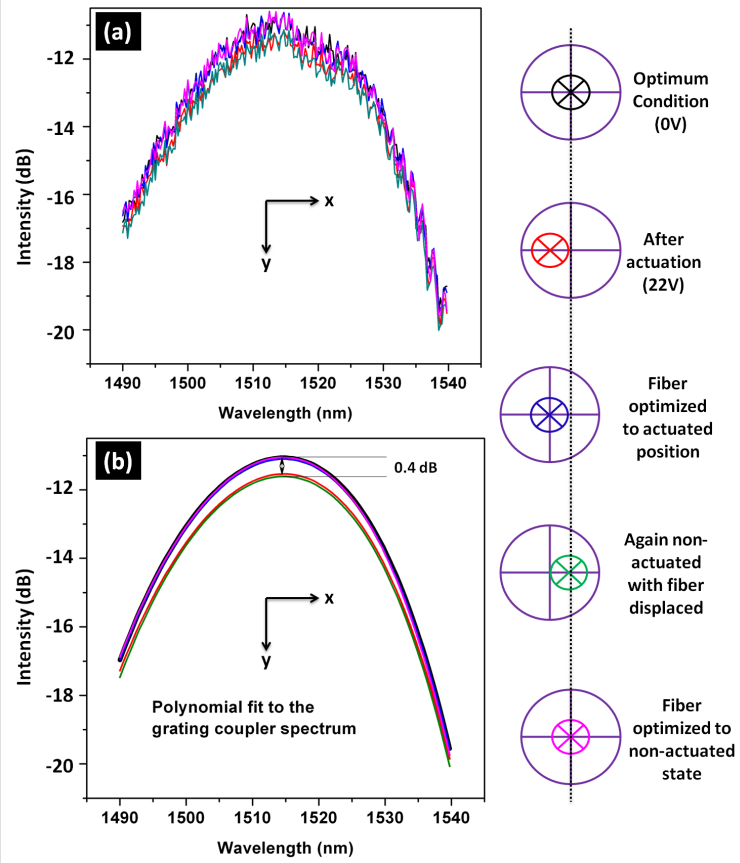

Figure 5.20: Change in transmission spectra of the grating coupler (a) when the FGC is displaced along the -ve x-direction due to actuation of the comb drives, (b) 3rd order polynomial fit of the transmission spectra clearly indicating the change in intensity level with the displacement of the FGC (The big circle represented the SMF whereas the smaller crossed circle represents the FGC).

polynomial fit of each spectrum as shown in Fig. 5.20b. As can be observed, at an applied voltage of ~ 22 V, an additional loss of 0.4 dB was measured. To confirm the direction of movement of the FGC, we then shifted the fiber in the -ve X direction and we could successfully reach back to the initial intensity at the same central wavelength of the FGC. Further, as we again went back to the non-actuated state as before keeping the SMF position fixed, the intensity again drops down because of the mismatch between the SMF and the FGC. Once, we move the SMF in the opposite direction from the previous one, the optimum

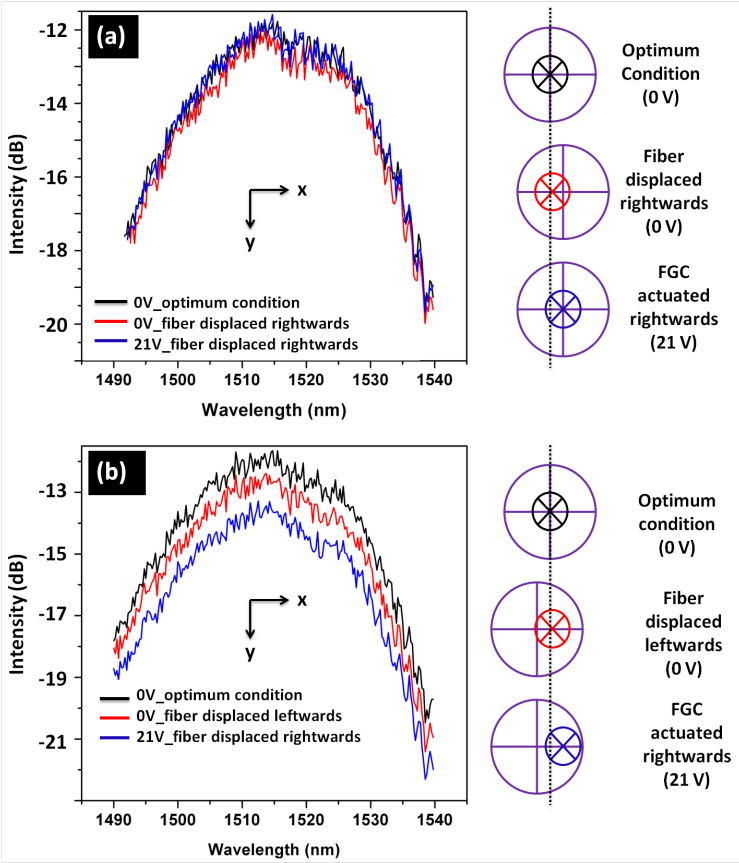

Figure 5.21: Change in transmission spectra of the grating coupler when the FGC is displaced along the +ve x-direction with the fiber displaced in the same direction (a) and in the opposite direction (b) (The big circle represented the SMF whereas the smaller crossed circle represents the FGC).

alignment is achieved again.

Fig. 5.21 shows another approach to prove the movement of the FGC, in this case in the +ve X direction. Here, we first moved the SMF in the +ve X direction to intentionally introduce an alignment loss of 0.3 dB. Thereafter, the actuators R and L are moved together to push the FGC to the right and as can be observed, we could again reach the same intensity distribution as in the non-actuated condition (Fig. 5.21a). Later, we moved the SMF in the -ve X direction from the optimum alignment condition and as we further push the FGC rightwards, due to an increased misalignment, the intensity at the central wavelength drops

down further as can be observed from Fig. 5.21b.

Hence, Figs. 5.20 and 5.21 together shows the successful implementation of the lateral movement of the FGC through the synchronized movement of the actuator 'L' and 'R' in the same direction.

Unlike the previous cases, Fig. 5.22 shows the case when the actuators R and L are moved in the opposite direction. As mentioned earlier, when the two actuators move in the opposite directions, the 'S' shaped flexures either get stretched or compressed hopefully making the FGC to move in the +ve or -ve Y direction respectively. Figs. 5.22a and 5.22b show the corresponding experimental results when the two actuators are moving towards each other and away from each other respectively.

Fig. 5.22a shows the two cases when the SMF is moved towards and opposite to the direction of the expected movement of the FGC (+ve Y direction). As can be observed, when the SMF is moved in the -ve Y direction and then the combs are actuated, the intensity drops further which is in accordance to our expectation. In the next figure, we show the case when the fiber is initially moved in the +ve Y direction and then the combs are actuated. In this case we cannot get back the same intensity level as we started with the optimum alignment condition. This result contradicts the expected movement of the FGC for the case when the actuators are moving towards each other. Similar experimental results can be observed (Fig. 5.22b) when the two actuators are moving away from each other which was supposed to push the FGC in the -ve Y direction. Next to that, a lot of devices were destroyed due to stiction of the comb fingers during stretching or compressing of the 'S' shaped flexures as shown in Fig. 5.23.

Though we are not fully sure of what could be the exact reason behind the non-performance of the stretching and compressing of the 'S' beams in the desired manner, one reason could be the deeply etched single mode waveguide which connects the FGC and the passive region. We designed the spring shape of the waveguide so that it gets compressed and extended following the movement of the FGC in the ± Y direction. But, unlike deforming a long spring sidewise, more force is needed to shorten or elongate them. Hence, it might be that the force imposed on the waveguide by the FGC is not large enough to deform it along its length.

Another possible reason of the failure of the mechanism could be the width of the designed 'S' beams which we kept to be 0.75 μm. With larger width, stretching or compressing the 'S' beams becomes more and more difficult which in-turn deteriorates the whole mechanism. Hence, to our understanding, though the lateral displacement (X direction) of the FGC works perfectly, these two reasons individually or together might have influenced the non-performance of the mechanism in the transversal (Y) direction.

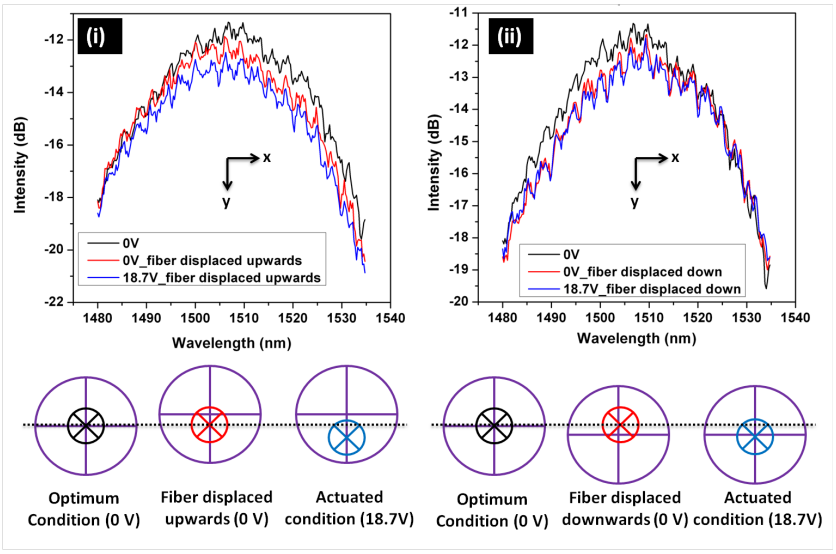

(a)

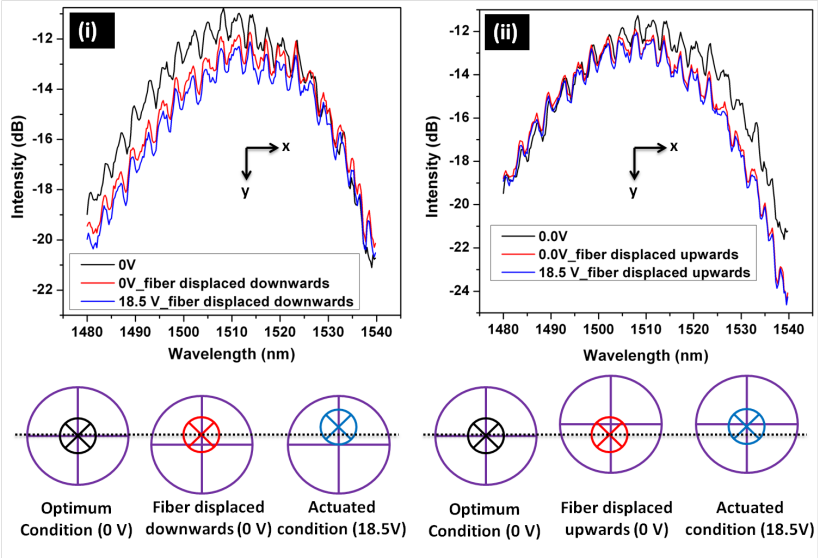

(b)

Figure 5.22: Change in transmission spectra of the grating coupler when the FGC is actuated along the +ve y-direction (a) and -ve y-direction (b) with the fiber displaced in the opposite direction direction (i) and in the same direction (ii) respectively.

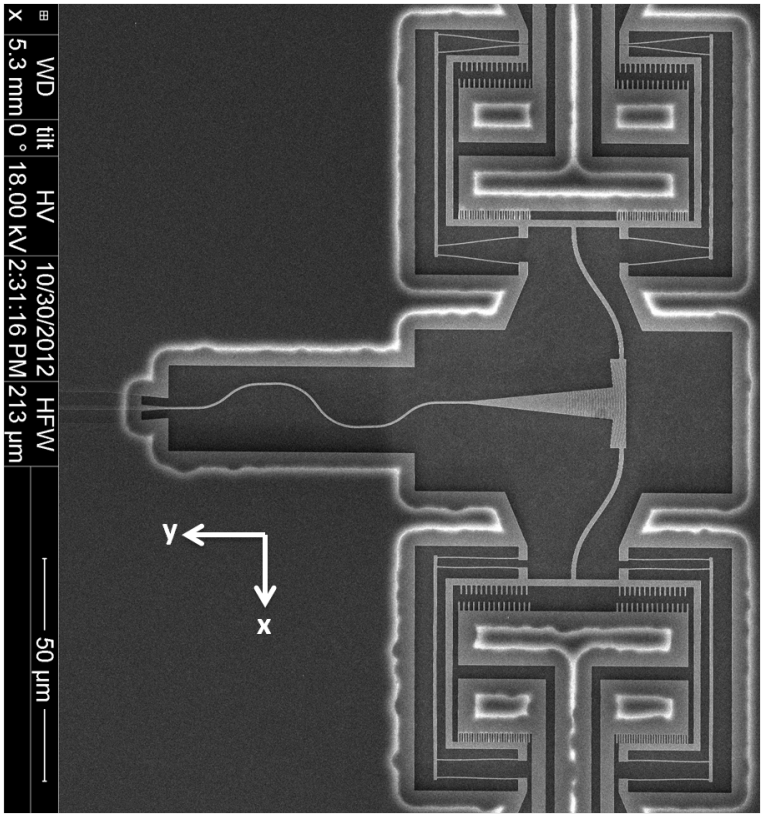

Figure 5.23: Sticking of the comb fingers during movement of the actuators L and R in the opposite direction.

5.9.2 Out-of-plane moving devices

As mentioned earlier, for the out-of-plane moving devices, we based our measurements on the changing angle between the SMF and the FGC which leads to a deviation from the optimum alignment condition. So, first we aligned the two fibers for maximum transmission and then the MEMS structure was actuated to measure the change in intensity caused by tilting of the grating coupler.

Fig. 5.24(a), shows the change in intensity when pad 1 (i.e. the back pad in Fig. 5.15b) is actuated. Similar results are obtained as when tilting the fiber as shown in Fig. 5.19 (note we are now working in the opposite reference frame). A clear decrease in transmitted intensity is observed with increasing the voltage. At the same time, a distinct red-shift in the transmission spectra for the actuated grating coupler can be found. This indicates that the grating is tilted downwards in the direction of pad 1 which decreases the angle θ between the fiber and the

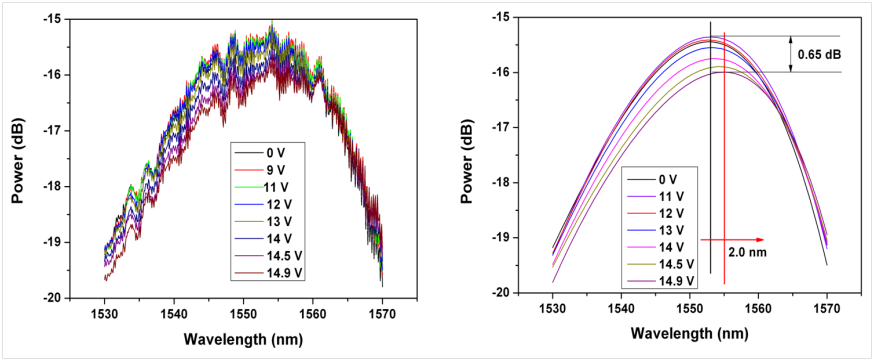

(a)

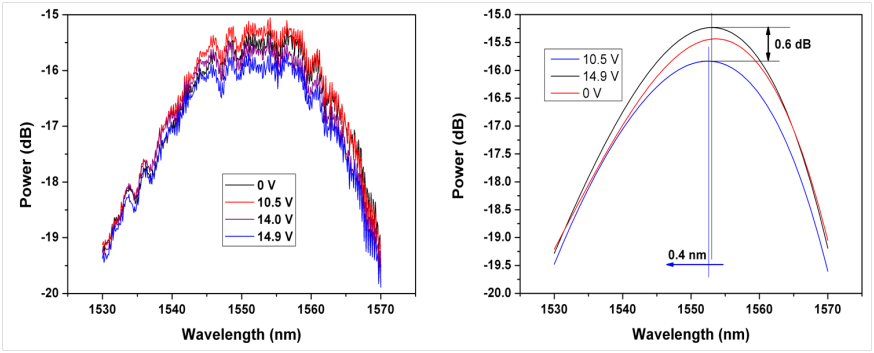

(b)

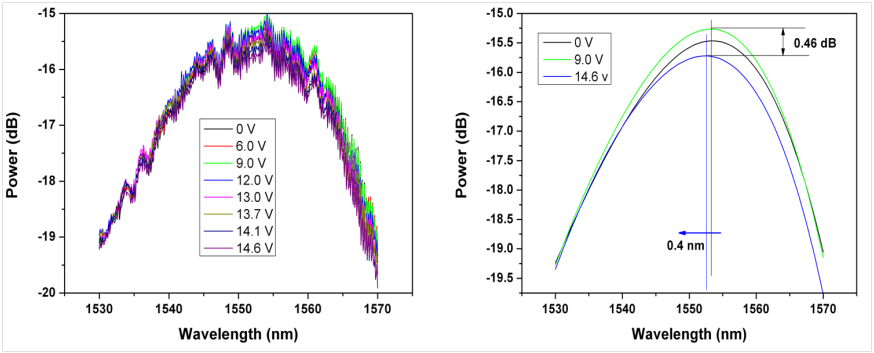

(c)

Figure 5.24: Variation in fiber-to-fiber measured transmission spectra from the grating coupler due to the actuation of the pad no. 1 (a), 2 (b) and 3 (c) (Fig. 5.15), when the other two pads are grounded. The three experimental results shown here, simultaneously correspond to the three COMSOL simulated results shown in Fig. 5.16

grating coupler. When compared to the calibration measurement, the tilt angle is found to be around 0.55°.

Fig. 5.24(c) and 5.24(b) shows the effect of actuation of the side pads (2 and 3 in Fig. 5.15). A similar phenomenon of decreasing intensity with increasing voltage is observed, but unlike the previous measurement, a 0.4 nm of blue-shift is observed here. At first sight, this seems to be due to the reduced stiffness of the structure at the front side (connecting the waveguide to the passive section) which also tilts slightly during the deformation of the serpentine beams connected to pads 2 or 3. This can be observed from the simulations in Figs. 5.16(b) and 5.16(c). It results in a minor increase of the angle of the fiber with respect to the grating and hence the wavelength of maximum transmission gets blue-shifted.

Unlike the particularly good device for which we described the above mentioned results, for several of our other devices we observed a current flow between the pads held at different potentials. Since our silicon waveguide structure is lightly p-doped, when two different pads on the same silicon structure are set at two different potentials, after a certain voltage difference a current flow starts between the two pads and hence there is a potential distribution throughout the silicon platform. This withheld us from performing further measurements by increasing the voltage above ~ 9-10V at any of the pads with respect to the other ones.

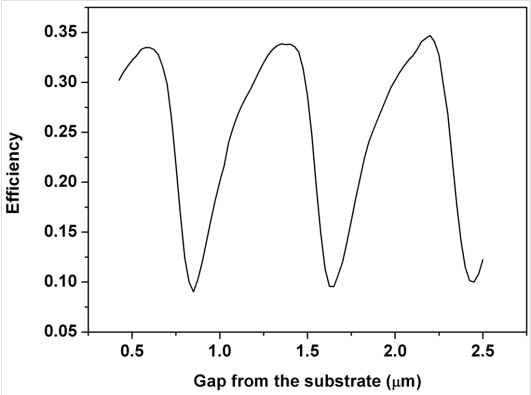

Figure 5.25: Grating coupler efficiency variation as function of the underlying airgap thickness.

At the same time, if we observe Figs. 5.16(c) and 5.16(b) closely then it can be seen that during tilting of the FGC in the sidewise direction, its height with respect to the substrate also decreases significantly. Hence, we also simulated the change in efficiency of the grating coupler with the change in its height from the substrate as shown in Fig. 5.25. As can be observed from the figure, when

the height decreases from 2.0 μm onwards, the efficiency of the grating coupler decreases steeply. So, it is evident that the decrease in height also alters the transmitted intensity from the FGC. Hence, the change of intensity that we observed from the experimental results can be a contribution from two interlocked factors of mismatch between the SMF and the FGC due to the MEMS actuation and also the change in FGC height from the underlying substrate due to lowering of the whole silicon platform when ac tuated. This makes it to be more complicated for us to understand the exact reason of change in intensity during the actuation of the FGC.

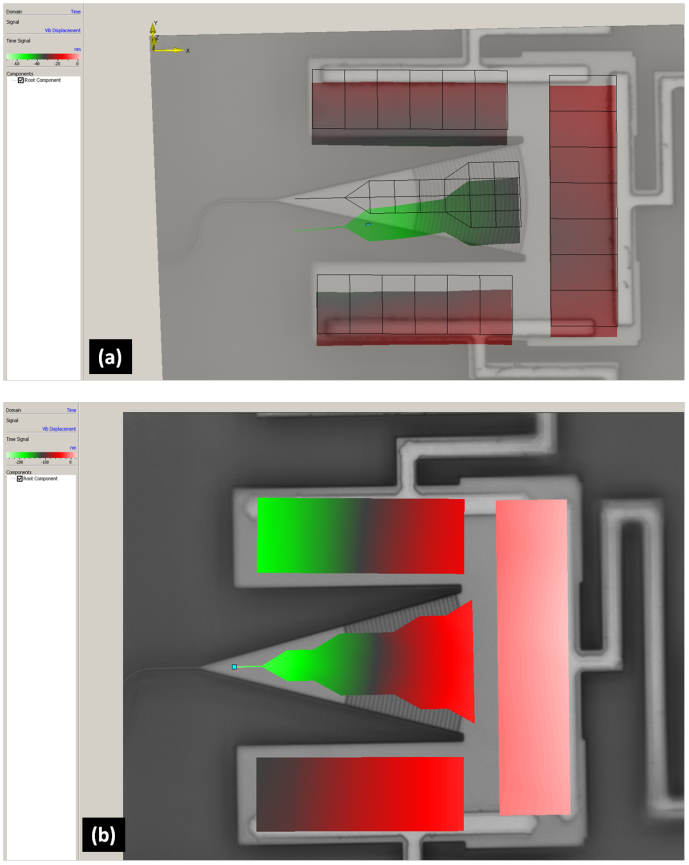

Figure 5.26: LDV measurement on the out-of-plane moving devices showing the results when the bakcpad (1) (a) and when the sidepad (2) (b) are actuated independently. In both the cases, a vertical displacement of the FGC is observed.

To better understand the operation of our device, we performed LDV (see

section 2.7.2) measurements on the vertical moving devices. Fig. 5.26a shows the case when the back pad, i.e. pad no. 3 was actuated. Surprisingly, instead of tilting in the backwards direction towards pad 3, we found that the device is tilted in the forward direction towards the connected waveguide. This is in direct contradiction to the obtained result from the transmission measurement because if the tilt is in the other direction then the angle to the fiber increases. With increase in angle θ (Eq. 5.7), the central wavelength λ_0 gets blue shifted whereas from the obtained optical measurements we saw it to be exactly opposite. Similarly, from Fig. 5.26b we again see that the FGC tilts in the forward direction when the sidepad (leftpad) of the device was actuated. Possibly, this is because of the current flow that we observed before during performing the optical measurements. Compared to the sides of the silicon platform supported by the serpentine structures, the tip of the grating coupler is instead supported by a long narrow waveguide. Hence, the stiffness against any vertical force on the silicon platform is minimum at the tip of the FGC. As a result, when the FGC structure is at a high potential compared to the grounded substrate, the whole FGC part goes downwards like a cantilever due to the vertical force acting on it.

To verify this, we again simulated the potential distribution over the whole silicon block using COMSOL Multiphysics (Fig. 5.27), considering the SOI structure to have 8 Ω cm resistivity and the metal pads to be in direct contact to the silicon platform. However, this simulation did not show any substantial voltage over the FGC structure, even when the pad opposite to the FGC was increased in potential up to 18V (sidepads were grounded). The current flow between the different pads observed by us during the optical measurements, occurred already at a much lower applied voltage of ~ 9-10 V for a device with the same dimensions as the simulated one. Overall, we got contradictory results from the optical and dynamic measurements of the LDV.

A possible solution to the problem of the current running through the silicon platform is to deposit the metal pads on top of an insulating material which avoids direct contact between the metal and the silicon platform. In that case there would not be any current flow between pads which are kept at a different potential. But the prerequisite is that the insulating material should be sufficiently resistant to vapor HF so that the deposited metal pads are never in conctact to the SOI structure. Though in literature, evaporated Al_2O_3 was mentioned to be resistant to vapor HF ([34]), in our lab we found it to be severely affected by the presence of vapor HF which creates big bubbles and penetrates through the Al_2O_3 films easily. Hence, this idea could not be tested any further.

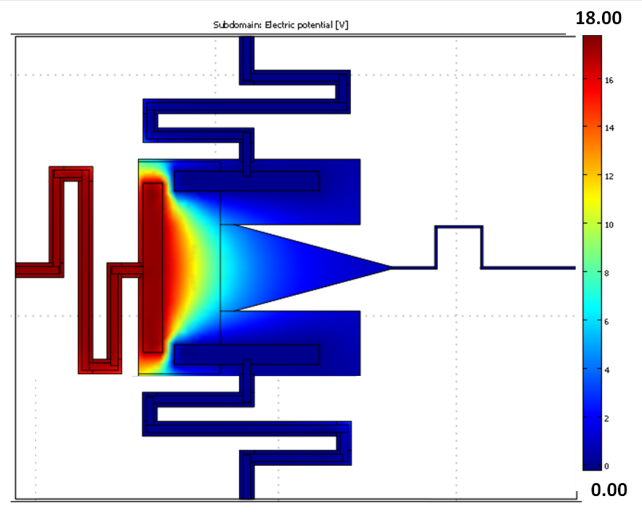

Figure 5.27: COMSOL Multiphysics simulation of the potential distribution over the rectangular block and the FGC when the backpad (pad no. 3 in Fig. 5.15) is actuated w.r.t. the two other side pads.

5.10 Conclusion

In this chapter, we introduced two novel approaches geared towards solving alignment problems in optical interconnects by combining silicon photonics and MEMS structures. We used the focusing grating coupler as the principal optical component which either helps in coupling incoming light to the photonic circuit (directly from an optical fiber or from integrated light sources like VCSELs or laser diodes) or out-coupling the processed signal to a desired location.

Using COMSOL Multiphysics, we showed the possibility to move the FGC in both orthogonal in-plane directions by using nanoscale comb-drives. Experimentally, we successfully proved the mechanism of synchronized movement of the FGC along the direction of movement of the two comb-drive actuators. The orthogonal (perpendicular to the direction of displacement of the combs) movement of the FGC is yet to be confirmed and more work is required to reinvestigate the mechanism by altering the dimensions of the actuator components and the spring shape of the freely hanging SMF.

We also showed COMSOL Multiphysics based FEM simulations for the serpentine structure based out-of-plane moving FGCs. We showed how the separate actuation of the three metallic pads on the silicon platform influence the tilting of the FGC in three independent directions. We believe, this operation

could not be experimentally demonstrated yet due to shortening of the metal pads through the lightly p-doped Si structure. Hence, we propose to add an insulating layer between the metallic pad and the SOI structure to prevent a short circuit between the individual pads. Additionally, we also believe that the determination of the tilt angle by measuring the change in coupling efficiency and shift of the central wavelength of the grating coupler spectrum is not the best approach. The change in coupling efficiency can be caused either because of the misalignment due to tilting of the FGC or because of the decrease in height from the substrate. These two reasons are difficult to be de-coupled using a fiber to FGC transmission measurement. Hence, a beam steering set-up with camera is needed to trace the steered beam movement to fully understand the effectiveness of the mechanism stated in the chapter. At the same time, to achieve ~ 4-5° steering of the light, the FGC holding structure has to be rotated further without suffering from any pull-in and hence the box layer thickness has to be increased to 5 μm or more.

References

[1] R. Dangel, C. Berger, R. Beyeler, L. Dellmann, M. Gmur, R. Hamelin, F. Horst, T. Lamprecht, T. Morf, S. Oggioni *et al.*, "Polymer-waveguide-based board-level optical interconnect technology for datacom applications," *Advanced Packaging, IEEE Transactions on*, vol. 31, no. 4, pp. 759–767, 2008.

[2] S. Assefa, S. Shank, W. Green, M. Khater, E. Kiewra, C. Reinholm, S. Kamlapurkar, A. Rylyakov, C. Schow, F. Horst *et al.*, "A 90nm cmos integrated nano-photonics technology for 25gbps wdm optical communications applications," in *Electron Devices Meeting (IEDM), 2012 IEEE International*. IEEE, 2012, pp. 33–8.

[3] J. Fedeli, R. Orobtchouk, C. Seassal, and L. Vivien, "Integration issues of a photonic layer on top of a cmos circuit," *Proc. SPIE6125 H*, vol. 61250, pp. 61 250H–15, 2006.

[4] R. Baets, P. Dumon, W. Bogaerts, G. Roelkens, D. Taillaert, B. Luyssaert, G. Priem, G. Morthier, P. Bienstman, and D. Van Thourhout, "Silicon-on-insulator based nano-photonics: Why, how, what for?" in *Group IV Photonics, 2005. 2nd IEEE International Conference on*. IEEE, 2005, pp. 168–170.

[5] J. Fedeli, M. Migette, L. Cioccio, L. El Melhaoui, R. Orobtchouk, C. Seassal, P. Rojo-Romeo, F. Mandorlo, D. Marris-Morini, and L. Vivien, "Incorporation of a photonic layer at the metallizations levels of a cmos circuit," in

Group IV Photonics, 2006. 3rd IEEE International Conference on. IEEE, 2006, pp. 200–202.

[6] J. Witzens, A. Scherer, G. Pickrell, D. Louderback, and P. Guilfoyle, "Monolithic integration of vertical-cavity surface-emitting lasers with in-plane waveguides," *Applied Physics Letters*, vol. 86, no. 10, pp. 101 105–101 105, 2005.

[7] D. Taillaert, R. Baets, P. Dumon, W. Wim Bogaerts, D. Van Thourhout, B. Luyssaert, V. Wiaux, S. Beckx, and J. Wouters, "Silicon-on-insulator platform for integrated wavelength-selective components," in *Fibres and Optical Passive Components, 2005. Proceedings of 2005 IEEE/LEOS Workshop on.* IEEE, 2005, pp. 115–120.

[8] T. Brenner and H. Melchior, "Integrated optical modeshape adapters in ingaasp/inp for efficient fiber-to-waveguide coupling," *Photonics Technology Letters, IEEE*, vol. 5, no. 9, pp. 1053–1056, 1993.

[9] T. Shoji, T. Tsuchizawa, T. Watanabe, K. Yamada, and H. Morita, "Spot-size converter for low-loss coupling between 0.3-μm-square si wire waveguides and single-mode fibers," in *Lasers and Electro-Optics Society, 2002. LEOS 2002. The 15th Annual Meeting of the IEEE*, vol. 1. IEEE, 2002, pp. 289–290.

[10] D. Taillaert, F. Van Laere, M. Ayre, W. Bogaerts, D. Van Thourhout, P. Bienstman, and R. Baets, "Grating couplers for coupling between optical fibers and nanophotonic waveguides," *Jpn. J. Appl. Phys*, vol. 45, no. 8A, pp. 6071–6077, 2006.

[11] V. Henneken, W. Sassen, W. van der Vlist, W. Wien, M. Tichem, and P. Sarro, "Two-dimensional fiber positioning and clamping device for product-internal microassembly," *Microelectromechanical Systems, Journal of*, vol. 17, no. 3, pp. 724–734, 2008.

[12] A. Unamuno, J. Yao, and D. Uttamchandani, "Alignment and fixing of fiber optics based on electrothermal mems actuators," *Photonics Technology Letters, IEEE*, vol. 17, no. 4, pp. 816–818, 2005.

[13] Y. Petremand, P.-A. Clerc, M. Epitaux, R. Hauffe, W. Noell, and N. de Rooij, "Optical beam steering using a 2d mems scanner," in *International Symposium on Optomechatronic Technologies*. International Society for Optics and Photonics, 2007, pp. 671 502–671 502.

[14] C. Ataman, Y. Petremand, W. Noell, H. Urey, and N. de Rooij, "A 2d mems stage for optical applications," in *Proceedings of SPIE, the International Society for Optical Engineering*. Society of Photo-Optical Instrumentation Engineers, 2006, pp. 618 603–1.

[15] G. Su, S. Hung, D. Jia, and F. Jiang, "Serpentine spring corner designs for micro-electro-mechanical systems optical switches with large mirror mass," *Optical review*, vol. 12, no. 4, pp. 339–344, 2005.

[16] T. Hirano, T. Furuhata, K. Gabriel, and H. Fujita, "Design, fabrication, and operation of submicron gap comb-drive microactuators," *Microelectromechanical Systems, Journal of*, vol. 1, no. 1, pp. 52–59, 1992.

[17] V. Jaecklin, C. Linder, N. De Rooij, and J. Moret, "Micromechanical comb actuators with low driving voltage," *Journal of micromechanics and microengineering*, vol. 2, no. 4, p. 250, 1999.

[18] G. Zhou and P. Dowd, "Tilted folded-beam suspension for extending the stable travel range of comb-drive actuators," *Journal of Micromechanics and Microengineering*, vol. 13, no. 2, p. 178, 2002.

[19] H. Jaafar, O. Sidek, A. Miskam, and S. Korakkottil, "Design and simulation of microelectromechanical system capacitive shunt switches," *Am. J. Engg. & Applied Sci*, vol. 2, no. 4, pp. 655–660, 2009.

[20] G. P. Agrawal, *Fiber-optic communication systems*. Wiley, 2010.

[21] S. K. Selvaraja, P. Jaenen, W. Bogaerts, D. Van Thourhout, P. Dumon, and R. Baets, "Fabrication of photonic wire and crystal circuits in silicon-on-insulator using 193-nm optical lithography," *Lightwave Technology, Journal of*, vol. 27, no. 18, pp. 4076–4083, 2009.

[22] F. Van Laere, T. Claes, J. Schrauwen, S. Scheerlinck, W. Bogaerts, D. Taillaert, L. O'Faolain, D. Van Thourhout, and R. Baets, "Compact focusing grating couplers for silicon-on-insulator integrated circuits," *Photonics Technology Letters, IEEE*, vol. 19, no. 23, pp. 1919–1921, 2007.

[23] [Online]. Available: http://www.epixfab.eu/technologies/imec-siphotonics

[24] SOITEC, "Soitec's unibond(r) process," *Microelectronics Journal*, vol. 27 (4/5), p. R36, 1996.

[25] M. Spak, D. Mammato, S. Jain, and D. Durham, "Mechanism and lithographic evaluation of image reversal in az 5214 photoresist," in *Seventh International Technical Conference on Photopolymers, Ellenville, New York*, 1985.

[26] R. Maboudian, W. Ashurst, and C. Carraro, "Self-assembled monolayers as anti-stiction coatings for mems: characteristics and recent developments," *Sensors and Actuators A: Physical*, vol. 82, no. 1, pp. 219–223, 2000.

[27] C. Mastrangelo, "Suppression of stiction in mems," in *MRS Proceedings*, vol. 605, no. 1. Cambridge Univ Press, 1999.

[28] M. Miles *et al.*, "Mems devices with stiction bumps," Jun. 30 2009, uS Patent 7,554,711.

[29] D. DeReus, "Mems device having contact and standoff bumps and related methods," Apr. 5 2005, uS Patent 6,876,482.

[30] A. Witvrouw, B. Du Bois, P. De Moor, A. Verbist, C. A. Van Hoof, H. Bender, and C. Baert, "Comparison between wet hf etching and vapor hf etching for sacrificial oxide removal," in *Micromachining and Microfabrication*. International Society for Optics and Photonics, 2000, pp. 130–141.

[31] J. Anguita and F. Briones, "Hf/h2o vapor etching of sio2 sacrificial layer for large-area surface-micromachined membranes," *Sensors and Actuators A: Physical*, vol. 64, no. 3, pp. 247–251, 1998.

[32] M. Offenberg, B. Elsner, and F. Lärmer, "Vapor hf etching for sacrificial oxide removal in surface micromachining," in *Proc. Electrochemical Soc. Fall Meeting*, vol. 94, no. 2, 1994, pp. 1056–1057.

[33] M. Zickar, W. Noell, T. Overstolz, C. Spörl, and N. De Rooij, "Quasi-dry release for micro electro-mechanical systems," in *Proceedings of the COMS Conference, Baden-Baden, Germany*, 2005, pp. 611–616.

[34] T. Bakke, J. Schmidt, M. Friedrichs, and B. Völker, "Etch stop materials for release by vapor hf etching," *Micromechanics Europe*, 2005.

6 Conclusions and outlook

6.1 Conclusions

The work presented in this thesis primarily focused on different kind of optical MEMS devices targeting various applications such as modern day display technology and optical communication systems. A significant part of the work in this thesis was directed towards the investigation of the CMOS compatible poly-SiGe technology in fabricating high quality optical MEMS devices. The validation was intended through the successful fabrication and subsequent performance evaluation of long and thin fixed-fixed microbeams and large perforated membranes using the poly-SiGe technology.

All of the previous work performed on GLV devices used silicon nitride as a structural layer with large tensile stress which resulted in high resonance frequency (~10 MHz) and consequently high switching speed. Instead, all our investigated poly-SiGe devices were accompanied with relatively lower resonance frequencies (~1 MHz) resulting in a challenge to obtain a fast switching rate. Hence, in our work, a significant effort was spent on optimization of the squeezed film damping which helped us in minimizing the settling time of the devices. We showed how dimensional changes influence the dynamic behavior of the microbeams and how a critical damped response can be obtained resulting in a fast switching rate (~2 μs) for the fabricated GLV devices. The changes in length and shape of the microbeams is clearly reflected also in the optical

characterization of the GLVs where we saw an increased contrast (>1500:1) with longer microbeams and flexure shape. Lastly, we showed how we used the different thicknesses of the bottom electrode to our advantage in making a pull-in protection scheme which saved the devices from accidental deterioration.

Later, we went one step further in extending the poly-SiGe technology in making a novel 2D MEMS grating based VOA. Instead of using short microbeams, we used a large (75 μm x 75 μm) perforated and suspended membrane. The perforations were filled with fixed islands forming the 2D grating shape once the membrane is deformed due to applied electrical actuation. This was also a test for the poly-SiGe technology to verify the stability of the large suspended membrane and to make sure that it does not buckle downwards. A minimal polarization dependent loss of 0.11 dB was obtained for the investigated VOA at a maximum attenuation of 20 dB. We were also able to obtain a critical damped response for the VOA with a settling time of $\sim$ 3.3 μs. It showed that by proper design of the membrane dimensions and the underlying airgap, the damping within the device can be optimized to maximize the switching speed.

Hence, the high contrast (or attenuation) and fast switching speed of the fabricated devices at relatively low actuation voltages prove the excellent characteristics of the poly-SiGe technology in forming large array of high quality MOEMS which can be monolithically integrated directly on top of CMOS.

On the other hand, the last part of the work was directed towards solving alignment problems in silicon photonic devices using MEMS technologies built in SOI. We used the focusing grating coupler (FGC) as the principal micro-optic component to couple light in/ out from a single mode fiber (SMF). We introduced the novel idea of moving the FGC in the two orthogonal in-plane directions with the help of comb-drive actuators to solve any misalignment between the SMF and the FGC. While the displacement ($\sim$ 1 μm) of the FGC along the direction of movement of the comb-drives could be unambiguously proven through optical measurements, the orthogonal displacement was not achieved with full effect. Additionally, we also introduced the novel idea of beam steering with the help of capacitive MEMS action by tilting the FGC to redirect the out-coupled light in the desired direction.

6.2 Outlook

Though the obtained specs for the poly-SiGe diffractive MEMS gratings that were shown in this work is definitely significant, a lot can still be done to improve the performance of the devices.

An obvious improvement is to tailor the fabrication process to incorporate higher tensile stress within the microbeams. It will help in achieving better dy-

namic behavior (higher resonance frequency and even shorter settling time) of the devices with longer microbeams. At the same time the longer microbeams will also help in achieving higher contrast due to flatter deflection at the center. Within the GEMINI project we have seen that with higher tensile stress the anchors were not able to hold the structural layer which resulted in deterioration of the devices. Hence, an improvement of this adhesion is needed from the point of view of inclusion of the larger tensile stress.

Also, the fabricated VOAs can be altered e.g. through using circular shaped islands distributed in a symmetric 2D array which will help in making the devices even more polarization insensitive. Also, new ideas are required to make the devices more wavelength insensitive to reduce the wavelength dependent loss.

On the contrary, the silicon photonic MEMS devices need a lot of improvements from the perspective of design and measurements. The 'S' beams connecting the FGC with the comb-drives should be thinned down to the minimum possible width (allowed within the design rules) to facilitate the movement of the FGC in the orthogonal direction to the comb-drive displacement. Obviously, with thinning down of the width of the 'S' beams, the stability of the freely-hanging FGC after the HF release etch also needs to be cross-checked. Related to the out-of-plane beam-steering device, a thorough process improvement is required to separate the SOI structure from the deposited metal electrodes by using an insulating layer. At the same time, we need to make sure that the insulating layer remains unaffected from the vapor HF process. It will help in stopping the short circuit between the actuation electrodes through the lightly doped silicon structural layer. Also, instead of using the fiber based readout mechanism, a camera set-up must be used to image the displacement of the steered beam in real time.

Overall, using the poly-SiGe MEMS devices we could already show high quality results. Hence, in near future, the poly-SiGe technology investigated in imec, is definitely poised to attract the attention of the industry which needs high quality MEMS devices fabricated in large arrays.

On the other hand, though silicon photonics have already attracted a great deal of scientific attention, combination of these devices with MEMS will bring more scientific wonders which are poised to solve several other challenges within the field of MOEMS.